The University of Sydney

Translation-Rotation Coupling in Collisions of Frictional Spheres and Structural Diversity and Stability in Amorphous Materials

Yue Ran Wang

Faculty of Science, School of Chemistry

A thesis submitted to fulfil requirements for the degree of Doctor/Master of Philosophy

"This research reported in this thesis was supported by the award of a Research Training Program scholarship to the PhD Candidate."

2024

Contents

Acknowledgments and Statements

Molecular Dynamics simulations were performed using the LAMMPS Molecular Dynamics Simulator originally developed at Sandia National Laboratories. The basic concepts of the Favoured Local Structure model were designed by P. Ronceray and P. Harrowell.

Chapter 2 of this thesis is published as:

> Y. Wang, and P. Harrowell, Translational-Rotational Coupling during the Scattering of a Frictional Sphere from a Flat Surface, *J. Chem. Phys.* **155**, 054303 (2021).

I co-designed the study with Prof. P. Harrowell, and fully contributed in the performance of data analysis and drafting of publication.

Chapter 3 of this thesis is published as:

> Y. Wang, and P. Harrowell, Translation–Rotation Coupling and the Kinematics of Non-Slip Boundary Conditions: A Rough Sphere between Two Sliding Walls, *J. Chem. Phys.* **159**, 054707 (2023).

I co-designed the study with Prof. P. Harrowell, and fully contributed in the performance of data analysis and drafting of publication.

This is to certify that to the best of my knowledge, the content of this thesis is my own work. This thesis has not been submitted for any degree or other purposes. I certify that the intellectual content of this thesis is the product of my own work and that all the assistance received in preparing this thesis and sources have been acknowledged.

Yue Ran Wang

27th February 2024

As supervisor for the candidature upon which this thesis is based, I can confirm that the authorship attribution statements above are correct.

Professor Peter Harrowell

27th February 2024

Acknowledgments

I would first like to express my sincere gratitude to Prof. Peter Harrowell for his supervision, patience, and kind help throughout my studies in the degree of Doctor of Philosophy. I would also like to thank Assoc. Prof. Toby Hudson for his valuable advice. Special thanks to the support from the University of Sydney in the form of University of Sydney Postgraduate Awards (UPA).

Abstract

There are a number of advantages of using computational simulation methods in chemistry research – the exploration of a conditions and parameters that are not feasible in the laboratory, time saving and cost saving compared to certain experimental methods, and the ability to reveal information that is difficult or impossible to obtain experimentally. The first study (Chapter 2) in this thesis uses molecular dynamics simulation methods developed for granular material, to introduce a model which studies the coupling of translational and rotational velocities of a spherical particle in collision with a surface. Analytical treatments are presented and kinematic expressions are derived for the important limiting classes of two types of collision: energy conserving and rapid transverse dissipation. The second study (Chapter 3) theoretically studies, from the results of Chapter 2, the consequences of the collision between a particle and two parallel walls under a non-slip boundary condition applied at the microscopic level. Results show the deposit of energy from wall to particle preferentially choses the rotational degree of freedom, and the particle can be trapped within a confined space with a bounded oscillation of energy. The third study (Chapter 4) presents a new diversity measure for the structural diversity of crystals and glasses, adapted from biodiversity literature, which shows great effectiveness in the filtering of noise. The Favoured Local Structure (FLS) lattice model is used to produce analytical data. Diversity measures show that the stability of structures involve the inclusion and exclusion of local structures, and the spectrum between crystal and glass is associated with a stabilization of either point-like defects or grain boundaries. A common ground in these distinctive studies is the use of simple models, which proves to be functional and effective for investigating generic problems.

Chapter 1. Introduction

This project spanned the period of the COVID pandemic and, like so many undertakings over that strange time, the initial plans for the project were disrupted. The result is a project reported in two very different areas of study. The first is an exploration of the coupling between translational and rotational motion of a rigid body, in particular how it occurs and what are the consequences of this coupling. The second project looks at developing a general measure of the structural diversity in condensed matter, a measure that can be applied equally to crystals and glasses, and all types of structures in between. These two topics are sufficiently distinct as to be best served by separate introductions, provided in Chapters 2.1 and 4.1.

There is, however, a common theme for both projects, namely the value of insights we can extract from simple models. Each project employs a greatly simplified model of phenomena that, in reality, is often highly complex. In the first project, the microscopic nature of translational-rotational coupling through collisions is addressed. The molecules that exhibit this coupling come in a wide variety of shapes, rigidities and interaction energies. Separating the general features of collisional coupling from this thicket of specific details has proven difficult. In this project, an extremely simple example of translational -rotational coupling based on a well-studied model of a frictional sphere has been considered. This model retains the coupling while avoiding the complications of molecular shape and internal vibrations. In the second project, a simple model of a condensed material for use as a testbed of the measure of structural diversity has been employed. Unlike more realistic models, the Favoured Local Structure model which will be later introduced allows easy adjustment to the complexity of the structure of the ground state of the system within a single consistent model. While it might be argued that modern computers and the richness of efficient algorithms possess higher values than that of simple models, providing quantitative accurate representations of real materials, an argument that shall be made here is that simple models remain important because simplification is now still a key attribute of physical understanding. A principle often attributed to in philosophy is the Occam's razor, stated by friar William of Ockham in the 14th century, stating that in the competition of a complex and a simple idea, the simple one is preferred. It is by eliminating the unnecessary that we establish what matters. No better example of this principle can be found than the Ising model.

A more accurate title would be the 'Lenz-Ising model' which was first proposed by Ernst Ising [1] in 1925, inspired by Wilhelm Lenz [2] in 1920. This simple model suggests that physio-chemical systems can be represented by a regular lattice arrangement of molecules in space [3], where each

node on the lattice is expressed with a value of either +1 or –1, and the interaction energy only depends on the configurations of neighbouring nodes. Ising [1] published his work based on ferromagnetic bodies in a one-dimensional lattice, but the expectations were not met for the two and three dimensional cases, thus the model was rejected by Ising himself. However in mid-1930, the Ising model showed success in two and three dimensions in the extensive work of Peierls [4] on ferromagnetism, and produced exact quantitative results in the study of transition temperature by Kramers and Wannier [5] in 1941. Since then, the Ising model has been noted in a substantial number of literature [6-8], and is still of interest in recent years [9-11].

Another field that must be accounted for in this thesis is computational science. This method of performing simulations on computers is widely used to solve problems in various fields of science. Two simulation methods are particularly introduced here, the Monte Carlo method (MC) and Molecular dynamics (MD). The Monte Carlo method was first developed by Metropolis and Ulam [12] in 1949 to deal with a class of problems in mathematical physics, considering the fact that an experiment may be required to repeat numerous times in order to achieve some general results. The basic concept of the model is the production of random numbers with a probability distribution within a domain of possible inputs, then performing a deterministic calculation on the chosen input. Right after the development, the MC method was adapted for use in physics and chemistry simulations, and was proven to be a powerful tool for studying molecular systems [13] and simulating physical processes [14]. The high popularity of the MC method in the field of computational chemistry was after the 1970s, and became an essential tool for the simulation of chemical systems and the prediction of their behaviours, such as studies on phase transition [15, 16] and lattice models [17]. Molecular dynamics on the other hand, is a simulation method designed to simulate the physical movement and interactions of microscopic bulk systems, generally atoms and molecules, first introduced as a computational method by Alder and Wainwright [18] in 1957, following the earlier success in the MC method. A significant difference between these two simulating models is that MD is parallelizable in a way that a single step calculates the interaction between all particles in the system, while originally the MC method can only move a single particle at a time. An associated problem that arises in MD simulations is due to the large sizes of molecular systems, and possibly long time evolution, the computation becomes extremely time consuming and requires high computational resources. Since the 1970s, along with the development of the performance of computers, algorithms [19] were also designed to improve the efficiency of MD simulations. With the help of High-Performance Computing (HPC) nowadays, the MD simulations have become increasingly sophisticated with a range of useful software [20], and numerous literature in various fields [21-23].

Both simulation methods introduced above will be employed in this thesis. Molecular dynamics simulations will be the basis of the study in Chapter 2, where a simple model is developed from expressions for studies in granular materials [24]. The spherical particle in the model exhibits translational-rotational coupling, which acts as a substitution for the anisotropic properties of molecular particles in collision with a surface. Chapter 4 focuses on the diversity and stability of local structures of both crystals, glasses and the intermediate range. The Monte Carlo method will be included in the modified piece of computational code, used for the production of analytical data. Chapter 3 on the other hand, is a pure theoretical study that follows the results from Chapter 2, considering non-slip boundary conditions in the microscopic level.

Chapter 2. Translational-Rotational Coupling during the Scattering of a Frictional Sphere from a Flat Surface

2.1 Introduction

In molecular collisions, rotations of the scattered particles are often observed, due to the anisotropic property of the particles. In these situations, a torque arises from the coupling between the anisotropic component of the particle interaction potential and the force acting on the centre of mass. The aim of this Chapter is to develop a physical picture of the occurrence of this coupling. To solve for this problem, the explicit relationship between the translational and rotational velocities of the particle after collision in accordance with the initial conditions, is the principle in this case. Such relations are regarded as 'kinematic', which only describes the motion of particles, with no details on the dynamic trajectory of the collisional event. However considering the anisotropies, it has been proved difficult, by a number of studies [25-29] on surface scattering of diatomic molecules, to obtain kinematic descriptions of collisions that are essential to the translational-rotational (TR) coupling. Due to the distribution of initial orientations of a particle, the outcome of a collision will not produce a single set of velocities, but a large distribution of final values. It was also noted [30] that an increase in particle anisotropy will also increase the width of distribution of the final states. Another difficulty with particle anisotropy arises from the unlimited possibilities of particle shape, which may result in an equally diverse range of possible kinematic outcomes.

The choice has been made to study the TR coupling of a spherical particle with a frictional interaction with the scattering surface, in order to address the difficulties of particle anisotropy. By introducing friction, it allows a torque to be produced on the particle, similar to the results of anisotropies, and at the same time avoids the complications raised by the distribution of particle orientations. A model developed Cundall and Strack [24] for the study of granular materials including a frictional contact similar to the observations made in macroscopic cases, is chosen here. The model may not be able to describe any collision in the molecular level, but will hopefully present some results which all such collisions have in common.

When considering collisions with friction, there is a variety of literature distributed across a diverse range of fields including sports physics [31-33], mechanical engineering [34, 35], applied mathematics [36] and robotics [37]. A kinematic equation for inelastic collisions was proposed by Newton [38] in 1687, such that $v_n(\infty) = -\varepsilon v_n(0)$ where the terms $v_n(\infty)$ and $v_n(0)$ are the final and

initial normal components of the translational velocity, and ε is the empirical coefficient of restitution with $0 \leq \varepsilon \leq 1$. The coefficient is generally $\varepsilon < 1$, where dissipation occurs due to energy transfer and plastic deformation. In the case of oblique, or non-collinear collisions, the relative translational velocity is associated with a non-zero transverse component that results in sliding during the collision. If the surfaces are 'rough', friction will produce a transverse force which generates a torque that couples with the angular velocity of the particle [39]. It may be questioned where this roughness lies in the granular model, either representing the shape anisotropy of the particle, or in the form of surface friction. In the context of particles in liquid [40], it has been demonstrated that the rotation of an anisotropic cylinder with a smooth surface (or slip boundary conditions) has very similar behaviours to that of a circular cylinder with a rough surface (or non-slip boundary conditions). Thus a strict answer to the question is not of concern due to this qualitative equivalence, and the model is acceptable to study anisotropic particles as frictional spheres. A note should also be made that the model used in this case is too simple to accurately represent any physical system. The main focus is to answer some basic questions about the details of translational-rotational coupling, namely the microscopic nature of the coupling mechanism.

This Chapter aims to derive the kinematic equations of coupling between translational and rotational velocity, described by the collision between a rotating frictional particle and a single flat surface. Two limits of interest shall also be derived: the purely elastic collision of a rough sphere, and the rapid dissipation of energy associated to rolling contact. The different channels of energy dissipation arising from the frictional collisions will also be considered in detail.

In Section 2.2, the granular model will be explained in detail, describing the expressions of motion for the frictional particle. Section 2.3 introduces the 'frozen' collision assumption, where the particle is constrained to a fixed normal distance from the surface, and presenting the analytic solutions for the periodic evolution of transverse and angular velocities. The results from Section 2.3 will be used to derive the general kinematic description of the particle-surface collision, and recover the conditions for 'rough' sphere dynamics in Section 2.4. Section 2.5 will focus on the energy dissipated during the collision, and derive kinematic expressions for damped collisions and the conditions under which rolling collisions occur.

2.2 Frictional Model and Granular Dynamics

The model used in this chapter to simulate the dynamics between a spherical particle and a surface with the effect of friction, is a model developed for the studies of granular material, implemented in

the LAMMPS package [41] by Silbert [42]. The basis of the granular dynamics is the Cundall-Strack model [24] which has been widely used in various granular applications [43].

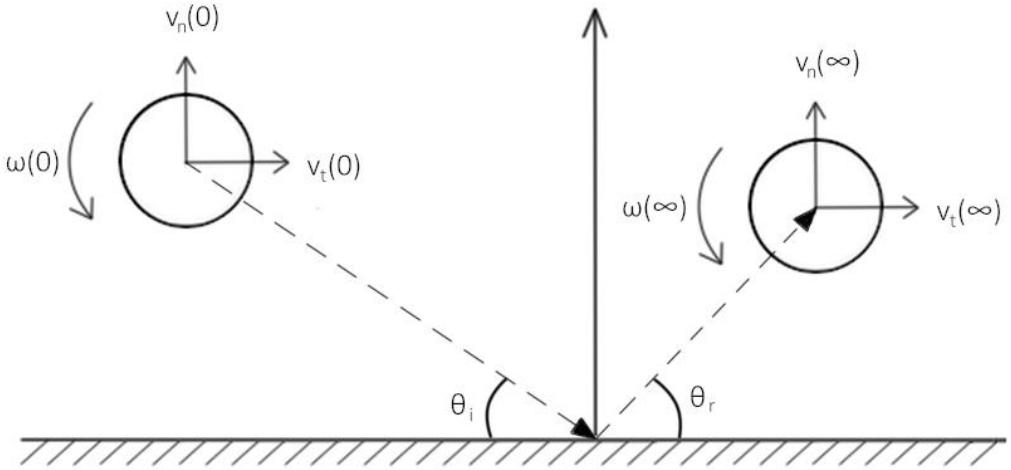

Figure 2.1. The scattering geometry of a spherical particle, indicating the initial and final components of the normal velocity v_n, transverse velocity v_t, and angular velocity ω. The incidence and reflection angles are given by $\theta_i = tan^{-1}\left(\frac{-v_n(0)}{v_t(0)}\right)$ and $\theta_r = tan^{-1}\left(\frac{v_n(\infty)}{v_t(\infty)}\right)$ respectively.

The various degrees of freedom involved in the particle-surface collision are depicted in Fig. 2.1. The translational velocity $\vec{v}$ acting on the centre of mass of the particle may be considered as two components, transverse velocity v_t and normal velocity v_n. The angular velocity of the particle follows the 'right hand rule' in vector algebra, such that a positive value corresponds to an anti-clockwise rotation in the 2D plane, and clockwise rotation for a negative value.

From the reference studies of the granular model [24,42], the forces acting between granular type interactions, particle-particle or particle-surface in this case, are defined as following in their transverse and normal components:

$$F_t = h(1 - z/r)(-k_t u - \gamma_t \dot{u})$$

$$F_n = h(1 - z/r)[-k_n(z - r) - \gamma_n \dot{z}] \qquad (2.1)$$

where k_t, k_n are the transverse and normal force constants; γ_n, γ_t are the explicit friction force coefficients; z is the normal displacement measured from the surface position at $z = 0$ (where $\dot{z} = v_n$); u is the elastic slip displacement between the point of contact between the sphere and surface at time t (as defined below as Eq. 2.2), and r is the radius of the particle. The function h indicates the spatial extent of the interaction between particle and surface, it is given here by the linear spring condition, $h(x) = 1$ for $x \geq 0$ and 0 otherwise. The friction coefficients γ_n, γ_t will be set to zero in the

following contents unless otherwise noted. The rate of change of the surface displacement u can be written as:

$$\dot{u} = v_t + r\omega \tag{2.2}$$

where $\dot{u}$ is the slip between the particle and the surface. The condition for rolling contact is zero slip via $\dot{u} = v_t + r\omega = 0$. Noting that v_t is the transverse component of the particle velocity, the associated force directly acts on the transverse and angular velocities as proposed in the following equations:

$$I\dot{\omega} = \mathrm{r}F_t \tag{2.3}$$

$$\mathrm{m}\dot{v}_t = F_t \tag{2.4}$$

where I is the moment of inertia, and m is the mass of the particle. Eq. 2.3 expresses the action of a torque as the tangential force in reduction form, where the radial length r here corresponds to the distance between the point of application of force F_t and the centre of the sphere. This value may differ from the radius of the sphere used to determine the moment of inertia. Eq. 2.4 defines the most important bit of physics in the granular model [24, 42]. Strictly speaking, the tangential force acting on the surface of the sphere at the point of contact cannot be also acting on the centre of the sphere. The kinematic linkage between the point of contact and the centre of sphere has been considered by multiple groups [34, 43].

The following parameters are used throughout this chapter unless otherwise stated:
$m = 1$, $r = 0.5$, $k_t = 1$ and $k_n = 10$.

2.3 'Frozen' Collision Assumption

The transverse and normal components of the translational velocity have separate behaviours during the collision with the surface, hence it is possible to look into them independently. The transverse velocity v_t couples with the rotation of the sphere in the plane of vector v_t and the surface normal $\hat{\vec{n}}$. The normal velocity v_n on the other hand, does not couple with the sphere rotation. It can be characterised as an elastic spring, within the contact distance set by $h(x)$ in Eq. 2.1. The approach and recoil of the sphere from the surface hence determines the duration of the collision.
In this Section, a constraint $v_n = 0$ shall be set, such that the normal distance between the sphere and the surface is fixed, allowing us to concentrate on the coupling behaviours between the transverse

velocity v_t and the rotational velocity ω. This constrained situation will be referred to as the frozen collision assumption.

By combining Eq. 2.3 and 2.4, a direct relation between the two degrees of freedom can be obtained,

$$\frac{I}{r}\dot{\omega} = m\dot{v}_t \tag{2.5}$$

followed by an integration to find the relation

$$\Delta v_t(t) = \frac{I}{mr^2} r\Delta\omega(t) \tag{2.6}$$

where $\Delta v_t(t) = v_t(t) - v_t(0)$ and $\Delta\omega(t) = \omega(t) - \omega(0)$. In this model the sphere is treated as a uniform solid, thus the moment of inertia $I = \alpha mr^2$ will have a constant value of $\alpha = 2/5$.

In order to solve for the explicit time dependence of the transverse and angular velocities, the evolution of the displacement *u* must be considered first, via combining Eq. 2.1 to 2.4:

$$\ddot{u} = \dot{v}_t + r\dot{\omega} = -k_t\left(\frac{1}{m} + \frac{r^2}{I}\right)u = -Qu \tag{2.7}$$

where

$$\mathrm{Q} = k_t\left(\frac{1}{m} + \frac{r^2}{I}\right) = \frac{k_t}{m}\frac{1+\alpha}{\alpha} \tag{2.8}$$

with a solution

$$u(t) = \frac{\dot{u}(0)}{\sqrt{Q}}\sin\left(t\sqrt{Q}\right) \tag{2.9}$$

where $\dot{u}(0) = v_t(0) + r\omega(0)$. The time dependence equations are therefore solved by substituting Eq. 2.9 into Eq. 2.3 and 2.4:

$$v_t(t) = v_t(0) + \frac{k_t\dot{u}(0)}{mQ}\left[\cos\left(t\sqrt{Q}\right) - 1\right]$$

$$r\omega(t) = r\omega(0) + \frac{r^2k_t\dot{u}(0)}{IQ}\left[\cos\left(t\sqrt{Q}\right) - 1\right] \tag{2.10}$$

The normal degree of freedom is effectively "frozen" by fixing the distance of the particle from the surface. The simple oscillations in Fig. 2.2 that are described by Eq. 2.10 explicitly represent the coupling of translation and rotation under this frozen collision, with the influence of the transverse force. As the magnitude of the rotational velocity increases, the periodic vibrations of the translational velocity diminishes, and vice versa.

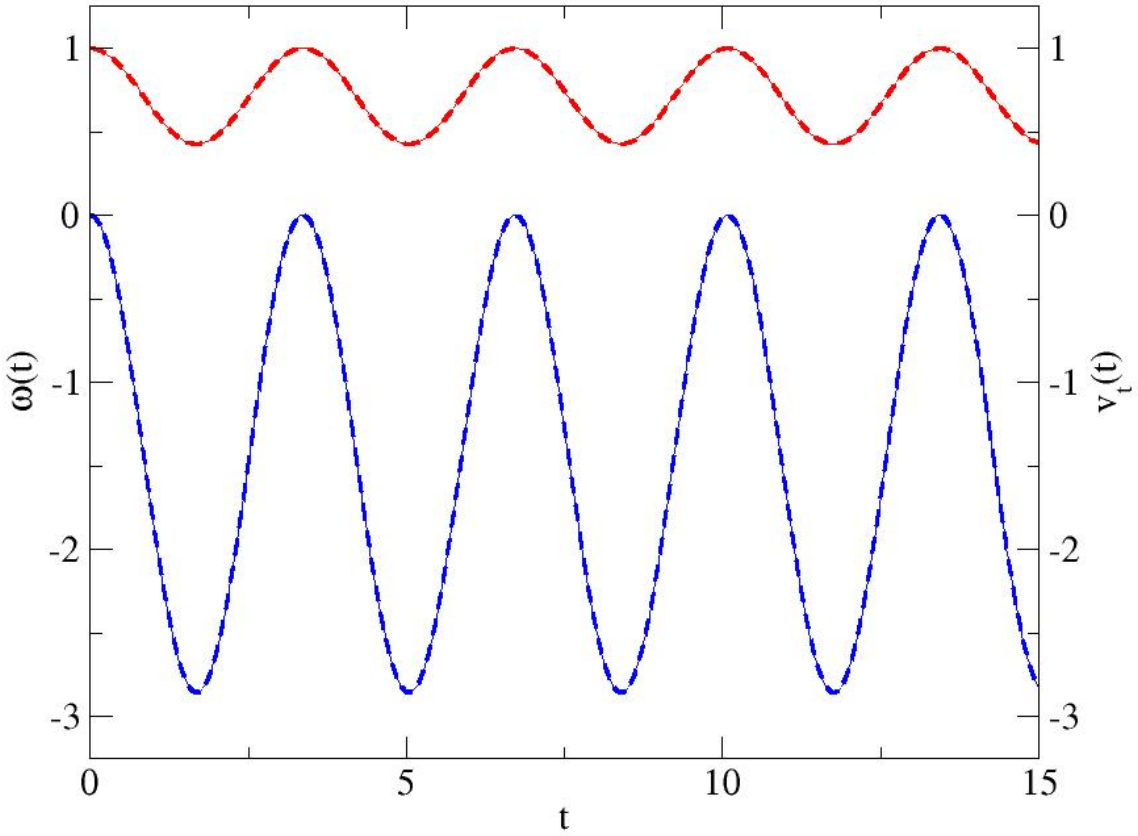

Figure 2.2. The time evolution of transverse velocity v_t (red) and angular velocity ω (blue) for a particle constrained with a vertical distance of $z = 0.1$ from the contact surface, with initial conditions $v_t(0) = 1.0$ and $\omega(0) = 0$. Each show two curves overlapping, one from the simulated model (dashed line) and the other calculated from Eq. 2.10 (thin solid line).

According to Eq. 2.10, the oscillation of v_t and $r\omega$ have non-zero mean values:

$$\bar{v}_t = v_t(0) - \dot{u}(0)\frac{\alpha}{1+\alpha}$$
$$r\bar{\omega} = r\omega(0) - \dot{u}(0)\frac{1}{1+\alpha} \qquad (2.11)$$

where $\bar{v}_t + r\bar{\omega} = 0$ corresponds to the rolling solution. This result therefore suggests that the motion described in Fig. 2.3 and by Eq. 2.10 may be better summarised as rolling accompanied with an oscillating slip, rather than a spring attached between the surface and the point of contact on the particle. It is due to the rolling motion that maintains the translation of the particle in the transverse axis, while the slip $u(t)$ transfers the energy between the particle's transverse and rotational motion.

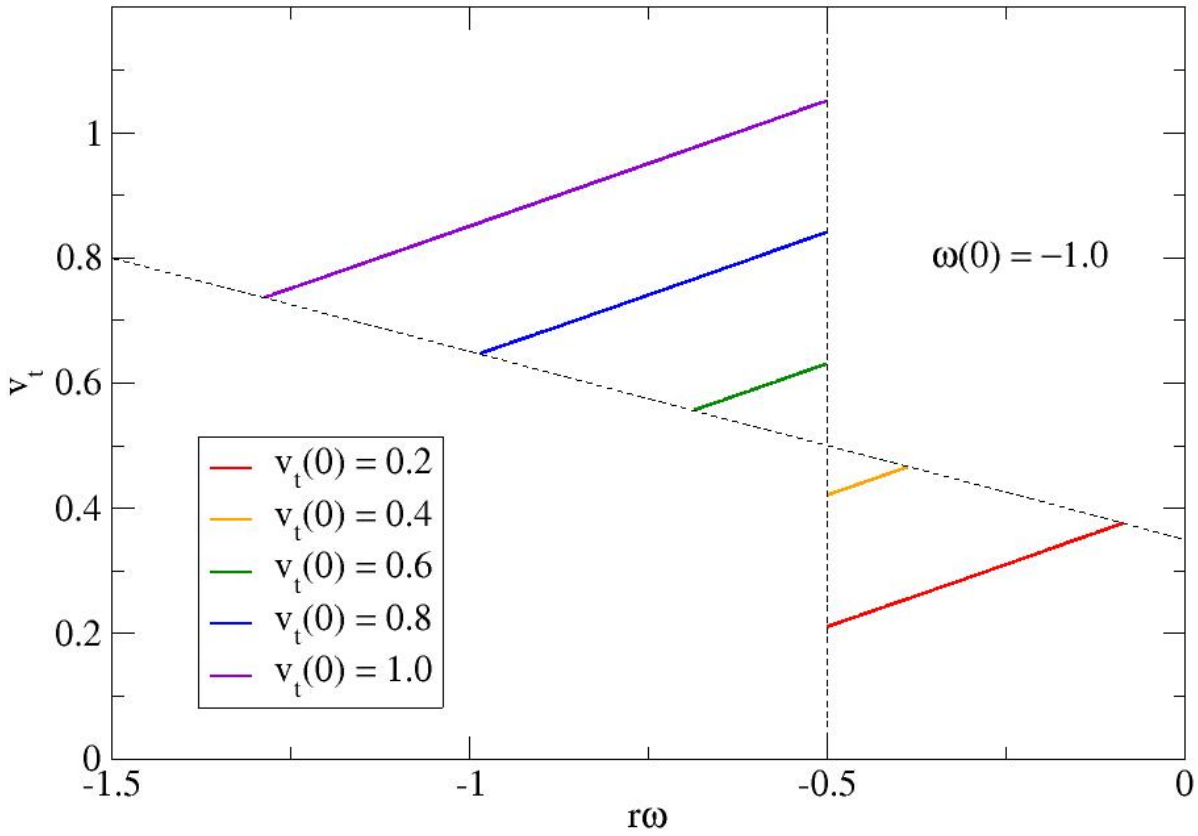

Figure 2.3. The trajectories of a particle in phase space v_t against $r\omega$ in the frozen collision with fixed normal position $z = 1$ and fixed initial rotational velocity via $r\omega(0) = -0.5$, varying the values of initial transverse velocity v_t (0).

The phase space [v_t, $r\omega$] in Fig. 2.3 illustrates the trajectory curves of the coupling of translational and rotational velocities under the frozen condition, with examples of various v_t (0) values with a fixed $r\omega(0)$ value of -0.5 . It may observed that for each curve, the motion takes place on a linear line in between two extremes of motion, that is ($v_t(0)$, $r\omega(0)$) and (v_t^m, $r\omega^m$). These values have equation:

$$v_t^m = v_t(0) - 2\frac{k_t \dot{u}(0)}{mQ}$$

$$r\omega^m = r\omega(0) - 2\frac{r^2 k_t \dot{u}(0)}{IQ} \qquad (2.12)$$

The linear appearance of the trajectories is directly due to the assumption discussed earlier, such that the transverse force of the centre of mass is considered equal to that experienced at the particle surface. In the case of a more realistic coupling [34, 43], the linear curves in Fig. 2.3 would be replaced by an elliptical orbit. The slope of each curve in Fig. 2.3 may be obtained from Eq. 2.6:

$$\frac{dv_t}{d(r\omega)} = \frac{I}{mr^2} = \alpha \qquad (2.13)$$

which would here equal to the solid sphere constant value 2/5, in agreement with the observed slope. In summary, the coupling between the translational and rotational velocities measured by the slope using Eq. 2.12, only depends on the mass distribution of the particle, as characterised by the moment of inertia *I*. The details of the interaction, included as variables in the equations, determine the boundaries of the values of v_t and rω.

2.4 Finite Interaction Times and the Scattering Matrix

After establishing the coupling relation of translation and rotation while the particle is in contact with the wall, the constraint in the normal direction may be removed and the overall outcome of the collision event shall be considered. Here τ is defined as the finite interaction time between the particle and wall, as a result of a non-zero normal translational velocity. The overall behaviour of collision may be considered approximately as the vibrations shown in Figs. 2.2 and 2.3 for some collision time τ, which is determined by the recoil of the particle in the normal direction, away from the surface. The normal velocity obeys the Hookean equation of motion as following:

$$m\dot{v}_n = \begin{cases} k_n(r-z) & \text{for } z \le r \\ 0 & \text{for } z > r \end{cases} \qquad (2.14)$$

where *z* is the normal distance between the centre of the particle and the surface, and $z > 0$ corresponds to the free space above the surface. The collision time τ is therefore defined as the time between the two instances of $z = r$. Eq. 2.4 may be solved to give

$$z(t) = r + \frac{v_n(0)}{p}\sin(pt) \qquad (2.15)$$

where $\mathrm{p} = \sqrt{\frac{k_m}{m}}$. The time τ required for the particle to return to its initial distance from the surface is then

$$\tau = \frac{\pi}{p} = \pi\sqrt{\frac{m}{k_n}} \qquad (2.16)$$

The collision time generally would be a decreasing function of the initial velocity $v_n(0)$, for example $\tau = 2r / v_n(0)$ for a hard sphere and wall interaction, however due to the harmonic interaction in this

particular case, the time t is independent of $v_n(0)$. Substituting time τ in Eq. 2.16 into Eq. 2.10, and equating values $v_t(\infty) = v_t(\tau)$ and $r\omega(\infty) = r\omega(\tau)$, the final velocities and the associated TR coupling for any collision may be estimated as:

$$v_t(\infty) = v_t(0) + \frac{k_t \dot{u}(0)}{mQ}\left[\cos\left(\pi\sqrt{\frac{mQ}{k_n}}\right) - 1\right]$$

$$r\omega(\infty) = r\omega(0) + \frac{r^2 k_t \dot{u}(0)}{IQ}\left[\cos\left(\pi\sqrt{\frac{mQ}{k_n}}\right) - 1\right] \tag{2.17}$$

Further inserting the equation of initial slip velocity $\dot{u}(0) = v_t(0) + r\omega(0)$, Eq. 2.17 may be rewritten in the following matrix form:

$$\begin{pmatrix} v_n(\infty) \\ v_t(\infty) \\ r\omega(\infty) \end{pmatrix} = \begin{pmatrix} -1 & 0 & 0 \\ 0 & 1 + \dfrac{\alpha\Omega}{1+\alpha} & \dfrac{\alpha\Omega}{1+\alpha} \\ 0 & \dfrac{\Omega}{1+\alpha} & 1 + \dfrac{\Omega}{1+\alpha} \end{pmatrix} \begin{pmatrix} v_n(0) \\ v_t(0) \\ r\omega(0) \end{pmatrix} \tag{2.18}$$

where $\Omega = \cos\left(\pi\sqrt{\frac{k_t}{k_n}\frac{1+\alpha}{\alpha}}\right) - 1$, and has value $\Omega \leq 0$ for all values of k_t and k_n. The off-diagonal terms here correspond to the explicit measures of the coupling between particle rotation and transverse velocity in this model. The relationship between v_t and ω may therefore be rewritten as:

$$\Delta v_t = v_t(\infty) - v_t(0) = \frac{\alpha\Omega}{1+\alpha}\dot{u}(0)$$

$$r\Delta\omega = r\omega(\infty) - r\omega(0) = \frac{\Omega}{1+\alpha}\dot{u}(0) \tag{2.19}$$

which clarifies that the translation-rotation coupling is directly proportional to the initial slip velocity $\dot{u}$. In this work the values $k_t = 1$ and $k_n = 10$ are used, hence $\Omega = -1.2838$ for a uniform solid sphere with $\alpha = 2/5$. It is clear in Eq. 2.19 that there will be no change in v_t or ω when $\dot{u} = 0$, via the rolling condition still ensures that no translation-rotation coupling occurs no matter the duration of a collision.

The values Δv_t and $r\Delta\omega$ against slip velocity $\dot{u}(0)$ are plotted in Fig. 2.4, for simple trajectory simulations calculated from a range of initial conditions, and the predictions calculated by Eq. 2.19 for comparison, in order to test the accuracy of the scattering matrix. The plot shows excellent agreement between the results from the granular dynamics model and our derived kinematic equations.

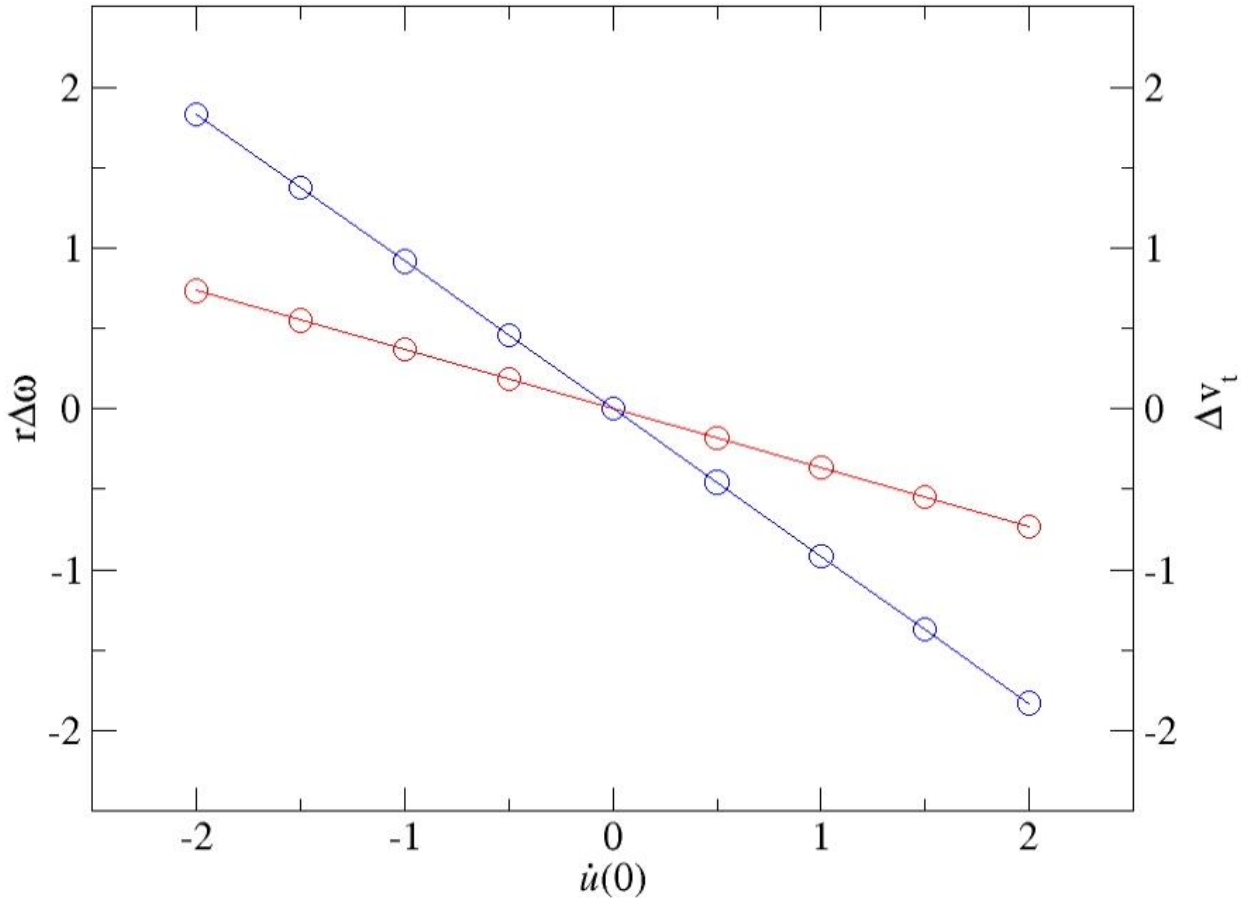

Figure 2.4. Scatter plots of Δv_t (blue circles) and $r\Delta\omega$ (red circles) against $\dot{u}(0) = v_t(0) + r\omega(0)$ for various choices of initial conditions. Straight lines represent predictions made by Eq. 2.19 for Δv_t (blue line) and $r\Delta\omega$ (red line).

In the work of Cundall-Strack [24], the equations of motion indicate that the transverse force responsible for the coupling of translational and rotational motion, arise in response to the surface slip displacement $u(t)$. When the interaction between the sphere and surface during collision is broken by the recoil of the particle, the slip displacement generally will be some non-zero amplitude. Since potential energy is associated with the slip, this will result as a dissipation of energy. This energy lost will not be considered in this Section, thus only considering the outcomes of scattering events with conserved energy. In order to avoid loss in energy, the point where interaction breaks between the particle and wall must have a slip displacement of zero. This condition can be found from Eq. 2.9 which occur at $t = n\frac{\pi}{\sqrt{Q}}$ for n = 0,1 ... via integer values, where even values n = 0,2,4 … correspond to conditions $v_t(\infty) = v_t(0)$ and $\omega(\infty) = \omega(0)$, that is a slip wall with no tangential force acting. When n is odd, a different version of the scattering matrix may be derived:

$$\begin{pmatrix} v_n(\infty) \\ v_t(\infty) \\ r\omega(\infty) \end{pmatrix} = \begin{pmatrix} -1 & 0 & 0 \\ 0 & 1-\dfrac{2\alpha}{1+\alpha} & -\dfrac{2\alpha}{1+\alpha} \\ 0 & -\dfrac{2}{1+\alpha} & 1-\dfrac{2}{1+\alpha} \end{pmatrix} \begin{pmatrix} v_n(0) \\ v_t(0) \\ r\omega(0) \end{pmatrix} \tag{2.20}$$

where $\Omega = -2$ as a result of $\tau = \pi/\sqrt{Q}$ when $n = 1$, thus forcing $\frac{k_t}{k_n} = \frac{\alpha}{1+\alpha}$. The matrix in Eq. 2.20 was originally derived by Garwin [45] based entirely on the conservation of energy and momentum, describing the kinematics of a 'rough' sphere bouncing off a surface. Several literature has considered the rough sphere model for the TR coupling between liquids. The kinetic expressions for the collisions between two rough spheres were derived by Chapman and Cowling [46]. In a series of papers by Berne and coworkers [47-49], the velocity correlations in molecular dynamics simulations of rough sphere liquids were studied. Note that the only parameter in the rough sphere model is α which characterizes the mass distribution of the sphere, with no detailed information about the transverse force between particle and surface. For the case of rolling contact $v_t(0) + r\omega(0) = 0$, Eq. 2.20 reduces to a frictionless surface result, consistent with the fact that the rolling particle experiences no transverse force.

Some example trajectories of rough sphere scattering are shown in Fig. 2.5, where it may be observed that the behaviours are rather different from slip surface collisions with no translation-rotational coupling. If we consider a solid particle with no initial rotation via $\omega(0) = 0$, then from Eq. 2.20 we may obtain a final rotational velocity of $r\omega(\infty) = -10/7\ v_t(0)$, and the final translational velocity v_t is reduced. According to the 'right-hand rule', a negative angular velocity $\omega < 0$ corresponds to a clockwise rotation, which acts as a forward roll in this particular case. Due to the transfer of momentum from transverse translational motion to rotational motion, the collision results in an angle of reflection smaller than the angle of incidence. Similarly, for a particle with some initial angular velocity and zero translational velocity $v_t(0) = 0$, via normal impact towards the surface, the particle will reflect with a translational velocity of $v_t(\infty) = -1/7\ r\omega(0)$, as indicated in Fig. 2.5d). A clear vision of rough sphere collision characteristics would be the *Wham-O Super-ball*® commercial video [50], showing bounce trajectories as shown in Fig. 2.5.

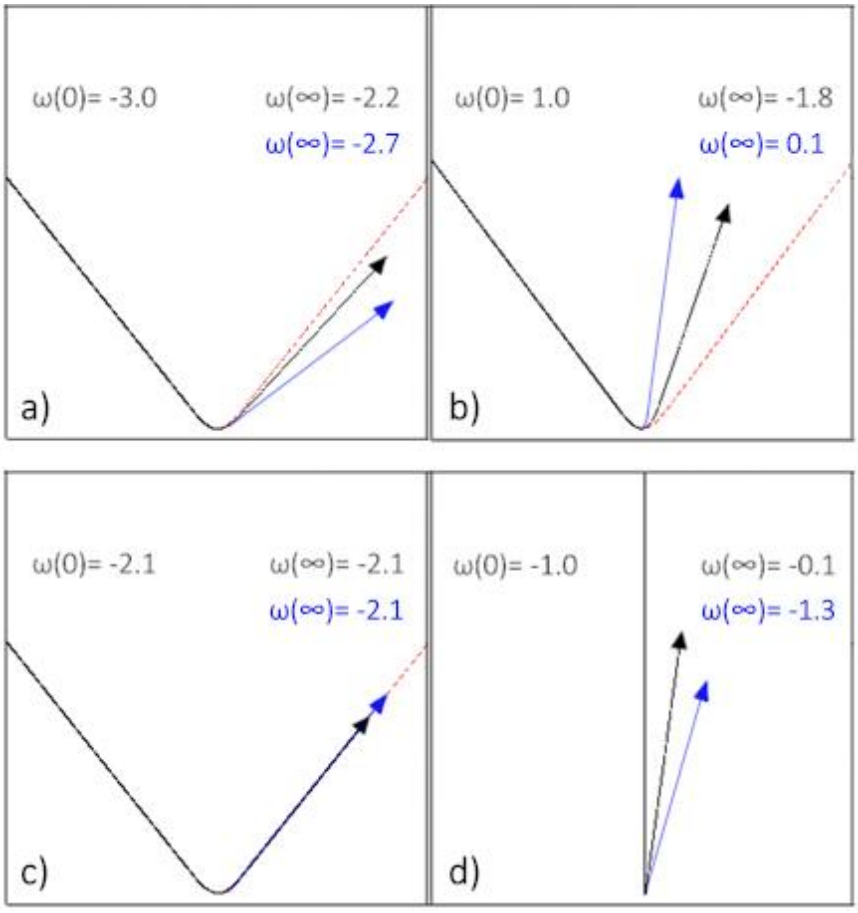

Figure 2.5. Example trajectories of particle scattering under conditions of Eq. 2.20 (rough sphere; black lines) and Eq. 2.23 (rolling condition; blue lines), in comparison with trajectories of zero transverse force (red dashed lines). The sub-figures indicates a) forward rotation for a negative initial rotational velocity, b) backward rotation for a positive initial rotational velocity, c) a rotational velocity that corresponds to the rolling condition, and d) transfer in momentum from rotational to transverse, for initial transverse velocity $v_t(0) = 0$.

2.5 Energy Dissipation

Considering the equations of motion from Eq. 2.1, energy dissipation may arise from two different features. One directly depends on the values of the explicit friction coefficients γ_t and γ_n. The other as previously mentioned, is when the interaction breaks while possessing a non-zero elastic strain, associated with an unrelaxed elastic slip displacement. The total loss in energy ΔE during a collision may be calculated as the difference between final and initial kinetic energies:

$$\Delta E = \frac{m}{2}\left(v_t^2(\infty) - v_t^2(0)\right) + \frac{I}{2}\left(\omega^2(\infty) - \omega^2(0)\right) + \frac{m}{2}\left(v_n^2(\infty) - v_n^2(0)\right) \qquad (2.21)$$

The dissipation may be defined as the fractional amount of initial kinetic energy lost in the collision via $f = -\frac{\Delta E}{E(0)}$. Since the surface slip plays an important role in energy loss, the relationship between dissipation f and the initial transverse slip $\dot{u}(0) = v_t(0) + r\omega(0)$ is presented in Fig. 2.6, where zero slip $\dot{u}(0) = 0$ leads to conservation of energy $f = 0$. The data depicted in Fig. 2.6 represent two sets of force constant values, with ratios k_t/k_n = 1/10 and 2/7 respectively. The case k_t/k_n = 2/7 corresponds to Eq. 2.20 describing the behavior of rough sphere model, and it is observed that the energy conservation shown in Fig. 2.6 is consistent with the condition of its original derivation.

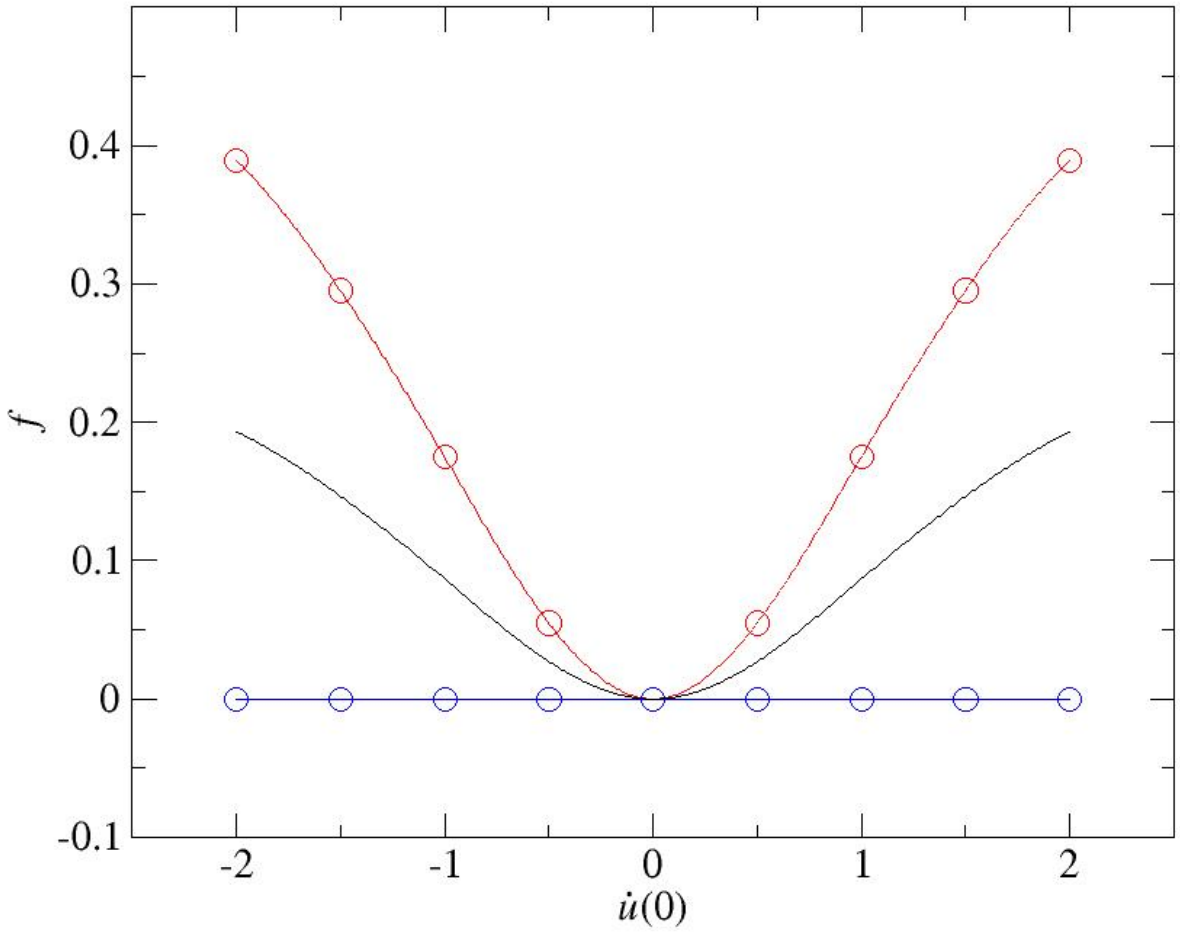

Figure 2.6. Energy dissipation $f = -\frac{\Delta E}{E(0)}$ as a function of $\dot{u}(0)$ for various initial conditions. Results are plotted for conditions k_t/k_n = 1/10 (red), k_t/k_n = 2/7 (blue), where simulation results are represented as circles, and predictions made by Eq. 2.18 as solid lines. Also plotted is the curve calculated from Eq. 2.23 for the rolling collision with a condition of large transverse damping coefficient γ_t (black).

In previous cases, the model focuses on the motion of the particle, and friction coefficients γ_t and γ_n had not been not considered. These explicit coefficients from Eq. 2.1 act as phonon modes of the surface, and provide damping, via removal of energy in an oscillating system, when the particle makes translational and normal contact with the surface. For a non-zero value of normal friction γ_n, the collision time τ increases and is dependent on $v_n(0)$, but does not apply any qualitative change in the translational-rotational coupling. Therefore only a non-zero value of the transverse friction γ_t will be considered.

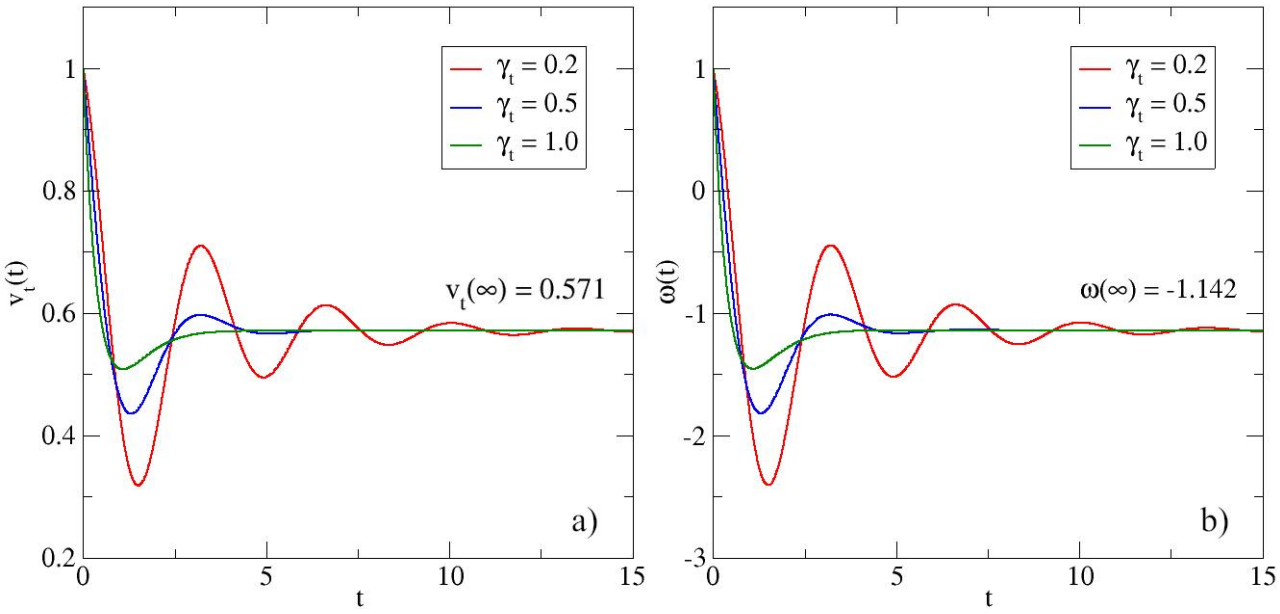

Figure 2.7. The time evolution of a) transverse velocity v_t, and b) rotational velocity ω under frozen assumption (particle constrained at a distance $z = 0.1$ from the surface), with initial conditions $v_t(0) = \omega(0) = 1.0$ for three different values of transverse friction coefficient γ_t. The velocities in every case decays to the rolling condition.

The time dependence of v_t and $r\omega$ under frozen collision assumption, similar to that of Fig. 2.2, is plotted in Fig. 2.7, for a range of values of γ_t. In each case, the oscillation of velocities decay to their mean value, in agreement with Eq. 2.11, which corresponds to the rolling solution. The decay in oscillation may be expressed by multiplying the term $\cos(t\sqrt{Q})$ in Eq. 2.10 by $\exp(\gamma_t\, t/m)$, hence the factor Ω in Eq. 2.18 may be replaced by

$$\widetilde{\Omega} = \exp\left(-\frac{\pi\gamma_t}{\sqrt{mk_n}}\right) cos\left(\pi\sqrt{\frac{k_t}{k_n}\frac{1+\alpha}{\alpha}}\right) - 1 \qquad (2.22)$$

For the condition $\gamma_t/m \gg \tau^{-1}$, where τ is the collision time from Eq. 2.16, the replaced factor $\widetilde{\Omega}$= -1 and the scattering outcome corresponds to the rolling solution as determined in Eq. 2.11, the matrix becomes:

$$\begin{pmatrix} v_n(\infty) \\ v_t(\infty) \\ r\omega(\infty) \end{pmatrix} = \begin{pmatrix} -1 & 0 & 0 \\ 0 & 1-\frac{\alpha}{1+\alpha} & -\frac{\alpha}{1+\alpha} \\ 0 & -\frac{\alpha}{1+\alpha} & 1-\frac{\alpha}{1+\alpha} \end{pmatrix} \begin{pmatrix} v_n(0) \\ v_t(0) \\ r\omega(0) \end{pmatrix} \tag{2.23}$$

The possibility that the recoil of a particle after collision ends by satisfying the rolling condition, was the basis of a kinematic treatment proposed by Brody [51] in 1984. Examples of trajectories described by Eq. 2.23 are depicted in Fig. 2.5. In comparison with the energy conserving rough sphere collisions, the rolling collisions show even larger deviations away from the frictionless case. In Fig. 2.6, the energy dissipation f of rolling collisions is also plotted, and proves that a non-zero dissipation coefficient may result in a reduce in total dissipation, where energy is lost when recoil of particle occurs while elastic energy is still present in the transverse slip.

2.6 Conclusions

This Chapter focuses on the physics behind the coupling between translational and rotational motion of a frictional sphere in collision with a smooth surface. In conclusion, the translational and rotational velocities lose their unique characteristics during the collision, and are converted into a set of coupled vibrations with a mean value of the rolling solution. Translational-rotational coupling therefore describes the exchange of momenta between temporarily coupled vibrational degrees of freedom. Collision performed between particle and surface with a non-zero normal velocity will have some finite contact time, and the outcome of the scattering event depends on the final position of the system along the coupled vibration trajectory. In general the collision will end with energy dissipation due to elastic energy stored within the unrelaxed slip displacement. Loss in energy may be avoided by setting the force constant parameters as k_t/k_n = 2/7 for the solid sphere case, as a specific characteristic of the Hookean style interaction. This adjustment allows the collision time to equal half of the translation-rotation oscillation period, and the friction particle may be modelled under conserved energy and momenta, in conformance with the rough sphere model. This study is believed to be one of the first examples of spherical model with the inclusion of translational-rotational energy transfer that can be simulated by molecular dynamics with energy conservation, in

contrast with an event-driven algorithm where the collision outcomes are determined by kinematic rules [47-49].

When considering the energy dissipation factors related to the equations of motion, two conclusions may be noted. One is in the limit of rapid dissipation due to the explicit friction coefficient, both translational and rotational velocity of the scattering outcome decays till reaching the rolling solution, for which dissipation is no further possible. The second is, depending on the choices of force constants k_t/k_n as presented in Fig. 2.6, collision involving a large friction may result in less dissipation than a zero friction case.

The rolling solutions that arise from the collision between frictional particle and smooth surface act as natural stationary points, and are a specific feature of particles with circular cross sections. This however, is only an identity in the case of a single surface. When considering collision of a spherical particle between multiple walls, the rolling condition can only be satisfied by pure normal motion.

With the detailed study of translational-rotational coupling in this Chapter, a more complex situation regarding the kinetics and TR coupling of a particle between two parallel walls will be considered in the following Chapter. Future work such as how TR coupling influences transport through pores, and the nature of TR coupling in liquids of frictional spheres with atomistic interaction potentials in also of interest.

Chapter 3. Translational-Rotational Coupling and the Kinematics of Non-Slip Boundary Conditions: A Rough Sphere between Two Sliding Walls

3.1 Introduction

One common type of boundary condition for fluid dynamics is the wall boundary condition, which is applied to reduce the constraint in fluid flow due to strong adhesive forces. The more appropriate representation is the non-slip boundary condition, which introduces the concept of slip length [52], defined as the distance from the boundary for which the velocity of fluid gradually vanishes. The non-slip boundary condition applies two limitations to the fluid as following:

$$v_n = 0$$
$$v_t^{wall} = V_{wall} \tag{3.1}$$

where the normal component of the fluid velocity v_n is set to zero, and the transverse component of fluid velocity v_t adjacent to the wall is set to the same velocity as the wall. The implementation of Eq. 3.1 at a microscopic level would be problematic, as it would require a discontinuous change in the velocity of particles upon the contact with the wall. In real life physics, the dynamics of particles in direct contact with the wall are determined by the morphology of the wall surface and the attractive interactions between wall and particle [53]. In this case, the conditions of non-slip boundaries arise as a result of resistance in motion caused by microscopic variations in the surface of the wall. Such variations cause difficulty in the smooth movement of particles, and results in more complex boundary conditions than expressed in Eq. 3.1, influenced by factors such as wall roughness and the interactions between wall and liquid particles. Due to this complexity of coupling between liquid and wall, substantial literature has been produced [54-56] for liquid-wall interface with consideration of the slip dependence on shear rate. The goal is to propose a functional but simple model with the ability to analyse the generic consequences of the microscopic coupling between wall and particle, and give results that are general enough to be made common use of. Again, the model only serves for answering some physical questions behind the wall-particle coupling, and does not represent any particular physical system.

This Chapter follows the contents on rough sphere translational-rotational (TR) coupling presented in the previous Chapter, to study the dynamics of the particle between two sliding parallel walls. The

non-slip properties associated to the rough sphere, which is also the source of the coupling between translational and rotational motion upon collision with the wall, is a simple representation of a microscopic non-slip condition.

The distinguishing feature of the rough sphere is the reversal of the transverse component of the particle's surface velocity, relative to the wall during collision. This reversal in addition to the sign flip of the normal velocity is a standard property for elastic collisions of smooth particles. This simple model, with sufficient interest, has been independently invented at least three times in different physical contents. It was first presented by Bryan [57] in 1894, and followed by Pidduck [58] in 1922, deriving the Chapman-Enskog equations for the kinetics of a dilute glass of rough sphere. Later in 1966, Dahler and co-workers [59, 60] further developed the kinetic theory of rough sphere gases. An extensive discussion was made on the model in the 1970 edition book [61] by Chapman and Cowling on gas kinetic theory. Another take on the model was by Waldmann [62] in 1963, who considered the kinetics of the rough sphere Lorentz gas, and commented that the TR coupling results in a significant decrease in the diffusion constant in comparison to the hard sphere. This model was extended to dense liquids by O'Dell and Berne [63], and Kravchenko and Thachuk [64, 65]. The second invention on the rough sphere model was in the late 1960's by Strobel [66] and Garwin [67] who rederived the kinematic equations for the model. Their inspiration was partly due to the appearance of the marketed toy 'Superball' [68], which exhibits unusual bounces due to strong TR coupling. The Garwin's model was later extended by Hefner [69] and Travares [70], in consider of motion between two walls. The purpose of these literatures appears to be largely for education use, although application on the phenomena of sports physics has also been seen [71]. The third incarnation of the rough sphere occurred in 1993 when Broomhead and Gutkin [72] introduced the model to study the dynamics of billiard with no-slip conditions in a confined space. This application of the rough sphere model was extended by Cox, Feres and Zhang [73] in the study of mathematical billiards. Again noted, a result from the previous Chapter shows that the rough sphere kinematics arises as a special case of the Cundall-Strack [24] frictional particle model, widely used in the modelling of granular material.

In Section 3.2, the kinematic equations of the rough sphere between sliding walls will be derived. Section 3.3 shall focus on an analytical expression [70] for the trajectories of the motion of the particle, and present observations of the rough sphere in a truncated channel, for use in the next Section. The consequences of the kinematic equations shall be considered for the case of stationary walls in Section 3.4. Finally, the influence of sliding walls on the dynamics of the particle shall be addressed in Section 3.5.

3.2 Rough Sphere Kinematics

Considering a rough sphere with radius *r* and mass *m*, its collision between two parallel walls with separation distance d+2r is as shown in Fig 3.1. The translational velocity of the sphere can be decomposed into normal and transverse components v_n and v_t where v_t lies along the x axis.

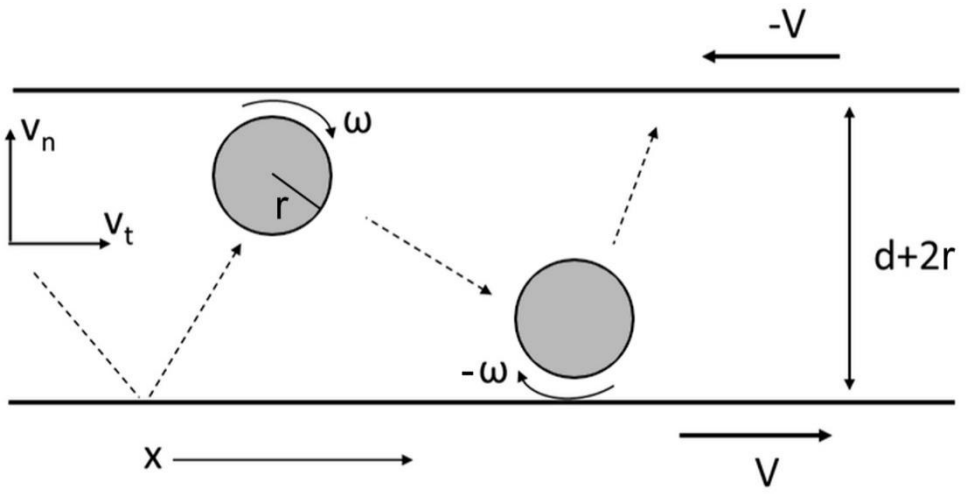

Figure 3.1. The 2D geometry of particle-channel system, indicating the width of the channel (d+2r), the transverse and normal directions of the particle (v_t, v_n), the radius of the particle (a value of r = 1 will be used for calculation simplicity throughout the Chapter), the motion of upper and bottom walls (*V*, -*V*), and the x coordinate. Note that the sign of the velocity acting on the surface of the sphere changes upon contact, depending on the reference frame (the upper wall or the bottom wall).

After each *i*th collision, let $v_n(i)$ and $v_t(i)$ be the normal and transverse components of the translational velocity of the centre of mass, and ω(*i*) be the angular velocity. The kinematic expression of the first collision of the rough sphere with the wall can be described as:

$$\begin{pmatrix} v_n(1) \\ v_t(1) \\ r\omega(1) \end{pmatrix} = \begin{pmatrix} -1 & 0 & 0 \\ 0 & M_{tt} & M_{tr} \\ 0 & M_{rt} & M_{rr} \end{pmatrix} \begin{pmatrix} v_n(0) \\ v_t(0) \\ r\omega(0) \end{pmatrix} \tag{3.2}$$

which is explicitly the scattering matrix for rough sphere model. Here the components measuring coupling between translational-rotational velocity is represented as:

$$M = \frac{1}{1+\alpha} \begin{pmatrix} 1-\alpha & -2\alpha \\ -2 & -(1-\alpha) \end{pmatrix} \tag{3.3}$$

with the conservation of kinetic energy and angular momentum about the point of contact [67]. The value α again is the mass distribution of a sphere in the expression for moment of inertia $I = \alpha mr^2$. The uniform solid sphere has α = 2/5, while the possible values of α range from 0~2/3. Zero corresponds to mass concentrated as a point in the centre, and 2/3 for a thin spherical shell.

The normal component of the translational velocity does not couple with other degrees of freedom, and only undergoes a reverse in sign after each collision, therefore it may be removed from the analysis which leaves the matrix with:

$$\begin{pmatrix} v_t(1) \\ r\omega(1) \end{pmatrix} = M \begin{pmatrix} v_t(0) \\ r\omega(0) \end{pmatrix} \tag{3.4}$$

The second collision comes in contact with the opposite wall, and as indicated in Fig. 3.1, the rotational component associated with the transverse motion of the particle surface changes sign in reference of the upper wall. That is, forward spin relative to the bottom wall would be backspin relative to the top wall. Thus the equation of the second collision is presented as:

$$\begin{pmatrix} v_t(2) \\ -r\omega(2) \end{pmatrix} = M \begin{pmatrix} v_t(1) \\ -r\omega(1) \end{pmatrix} \tag{3.5}$$

A rotation matrix defined by Travares [70] may be introduced as:

$$D = \begin{pmatrix} 1 & 0 \\ 0 & -1 \end{pmatrix} \tag{3.6}$$

therefore the *i*th collision may have:

$$\vec{v}_i = \begin{cases} M\vec{v}_{i-1}, & \text{for odd } i \\ D^{-1}MD\vec{v}_{i-1}, & \text{for even } i \end{cases} \tag{3.7}$$

where

$$D^{-1}MD = \frac{1}{1+\alpha}\begin{pmatrix} 1-\alpha & 2\alpha \\ 2 & -(1-\alpha) \end{pmatrix} \tag{3.8}$$

and $\vec{v}_i = \begin{pmatrix} v_t(i) \\ r\omega(i) \end{pmatrix}$

By considering the rough sphere collision with reference of the moving walls, the wall velocity *V* may be applied into the kinematic equations with energy conservation condition, and the reversal of particle surface velocity at contact:

$$\vec{v}_i = \begin{cases} \vec{Q} + M(\vec{v}_{i-1} - \vec{Q}), & \text{for odd } i \\ -\vec{Q} + D^{-1}MD(\vec{v}_{i-1} + \vec{Q}), & \text{for even } i \end{cases} \tag{3.9}$$

where $\vec{Q} = \begin{pmatrix} V \\ 0 \end{pmatrix}$. As a result of change in reference frame, the effective transverse velocity of the centre of mass of the particle is adjusted, while the angular velocity remains unchanged. This points out a separation in the translational and rotational degrees of freedom. Due to opposite motion of the two walls, the associated sign of $\vec{Q}$ will change depending on odd or even collision numbers.

3.3 Particle Motion in a Truncated Channel

Having derived the kinematic expressions for the *i*th collision, the actual motion of the particle colliding between two parallel rough walls is considered for a basic situation of a truncated channel with no wall motion. As shown in Fig. 3.2, the particle is injected from the open end, into a truncated channel with separation d+2r. The first collision will have a position on the x axis within a range of 0~dv_t,/v_n.

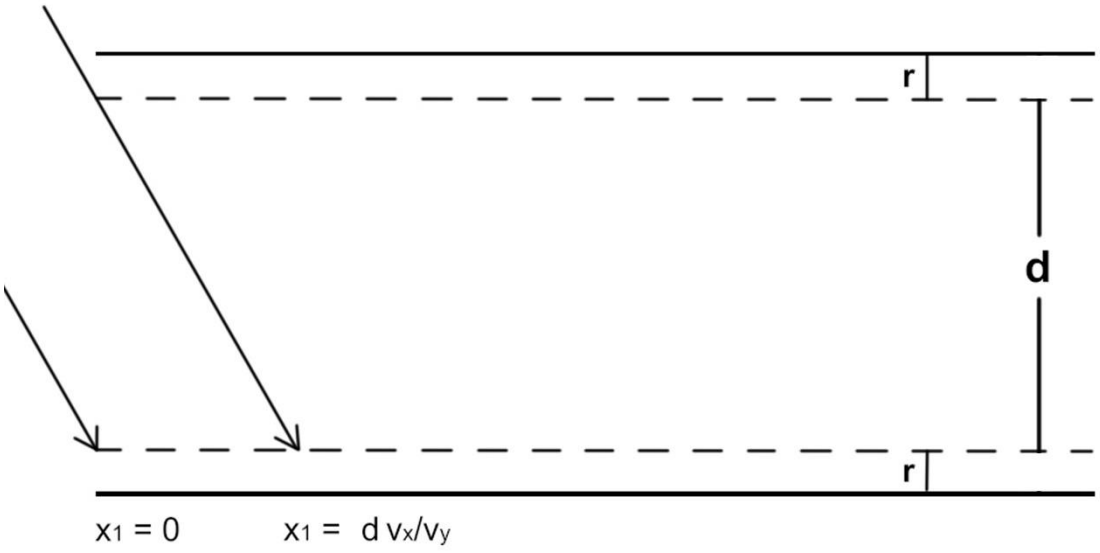

Figure 3.2. Injection of the particle through the open end of channel, indicating the geometrical definition of the maximum and minimum values of the position of first collision x_1. Channel has width d+2r.

An analytical expression has been derived by Travares [70] to solve for x_n, the position of particle along the x axis at the nth collision:

$$\Delta_n = x_n - x_1 = \frac{A\Delta t}{2}\left[\frac{\sin\left(\frac{(n+1)\theta}{2}\right)\cos\left(\varphi + \frac{n\theta}{2}\right)}{\sin\left(\frac{\theta}{2}\right)} - \cos(\varphi) - \cos(n\theta + \varphi)\right] \tag{3.10}$$

where

$$A = \sqrt{v_{0,t}^2 + \alpha\bar{\omega}_0^2}$$

$$\varphi = \arctan\left(\frac{\sqrt{\alpha}\bar{\omega}_0}{v_{0,t}}\right) \tag{3.11}$$

and

$$\cos(\theta) = \frac{1-\alpha}{1+\alpha}$$

$$\sin(\theta) = \frac{2\sqrt{\alpha}}{1+\alpha} \tag{3.12}$$

Two terms $\mathrm{P} = \sqrt{\alpha}\frac{r\omega(0)}{v_t(0)}$ and $\mathrm{Q} = \frac{v_t(0)}{v_n(0)}$ may be defined, then the expressions become

$$\Delta_n = d\frac{Q}{2}\sqrt{1+P^2}f(n,P)$$

$$x_1 = dQ \tag{3.13}$$

For a particle which is injected to the channel at maximum depth will rebound, as shown in Fig. 3.3a), eject the channel at the same open end of injection, if $\Delta_n/x_1 > -1$ for any value of $n > 1$. From Eq. 3.11 it can written:

$$\frac{\Delta_n}{x_1} = \frac{1}{2}\sqrt{1+P^2}f(n,P) \tag{3.14}$$

which indicates that the rebound condition only depends on *P*, and is independent of the term *Q*.

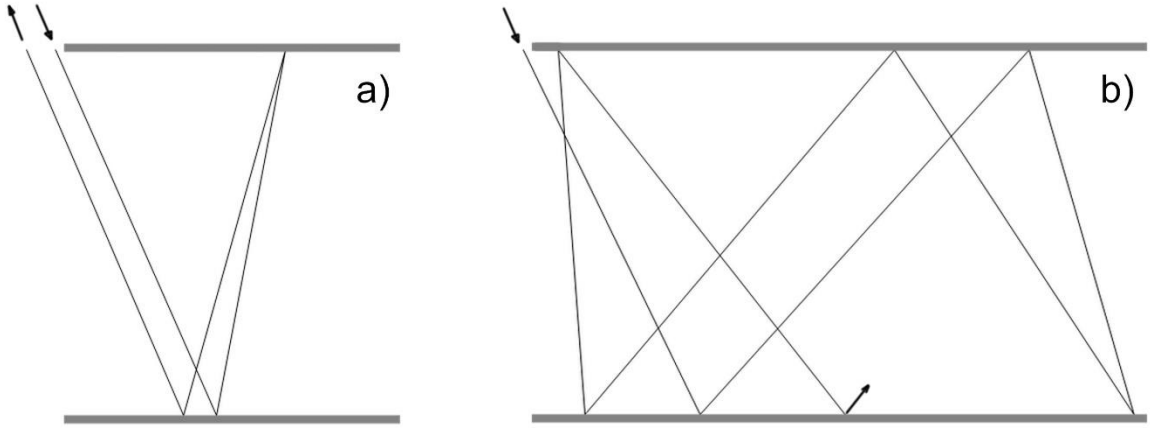

Figure 3.3. Example trajectories of a) rebound of the particle from the injection end with initial conditions $v_t(0) = 1$ and $\omega(0) = 0$, and b) particle trapped within channel with initial conditions $v_t(0) = 1$ and $\omega(0) = -2.5$.

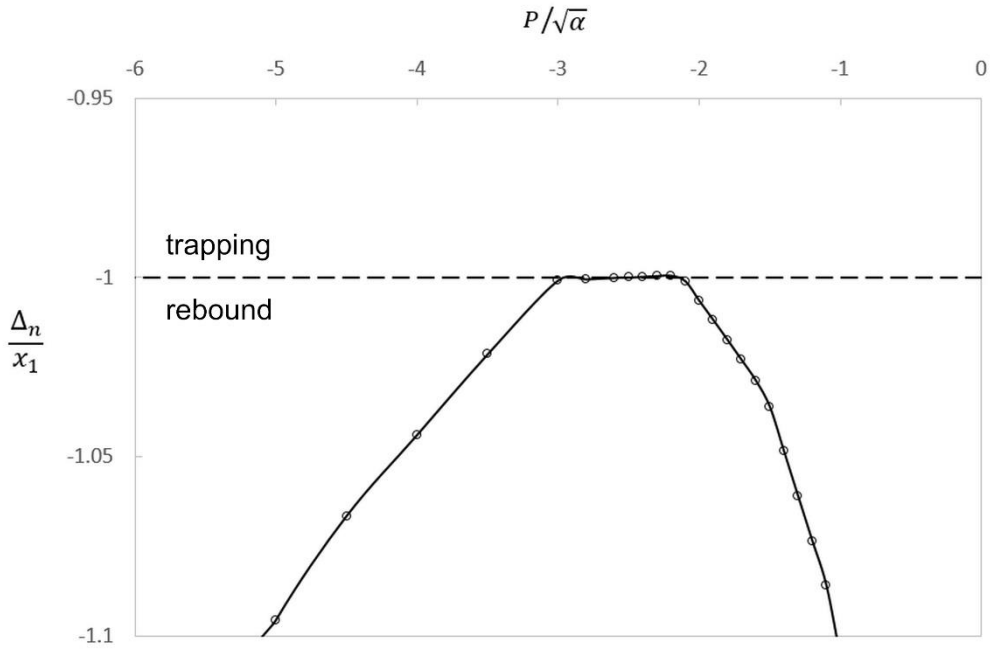

Figure 3.4. The minimum values $\frac{\Delta_n}{x_1}$ against $\frac{P}{\sqrt{\alpha}} = \frac{r\omega(0)}{v_t(0)}$ for a variety of initial conditions for first particle collision with the bottom wall. The threshold between trapping and rebound is $\frac{\Delta_n}{x_1} = -1$, and the range $-3.0 < P/\sqrt{\alpha} < -2.2$ shows 'marginal trapping'.

For a range of initial conditions $P/\sqrt{\alpha}$, the minimum value of Δ_n/x_1 is calculated as shown in Fig. 3.4. Note that the truncated channel is long enough such that the particle will not pass through the opposite end. It is observed that apart from the range $-3.0 < P/\sqrt{\alpha} < -2.2$, all other values satisfy the condition for rebound (Fig. 3.3a)). In the limited range of initial angular velocities, the

trajectory of particle reaches a position extremely close to the open end of the truncated channel, and the particle is considered under the situation of *marginal trapping* (Fig. 3.3b)), where there exists a transverse bound such that the particle trajectory lies within this bound for a significant amount of collisions. In this case the result only considers first collision with the bottom wall. For first collision of the particle with the upper wall, the sign of angular velocity will be flipped, thus the 'marginal trapping' will have range $2.2 < P/\sqrt{\alpha} < 3.0$. Combining both situations in Fig. 3.5, there will be two regions of where marginal trapping may occur, $2.2 < |P|/\sqrt{\alpha} < 3.0$, depending on whether the particle first collided with the bottom or upper wall. For all other initial choices of angular velocity, the particle will show rebound behaviour, exiting the truncated channel from the same open end as injected.

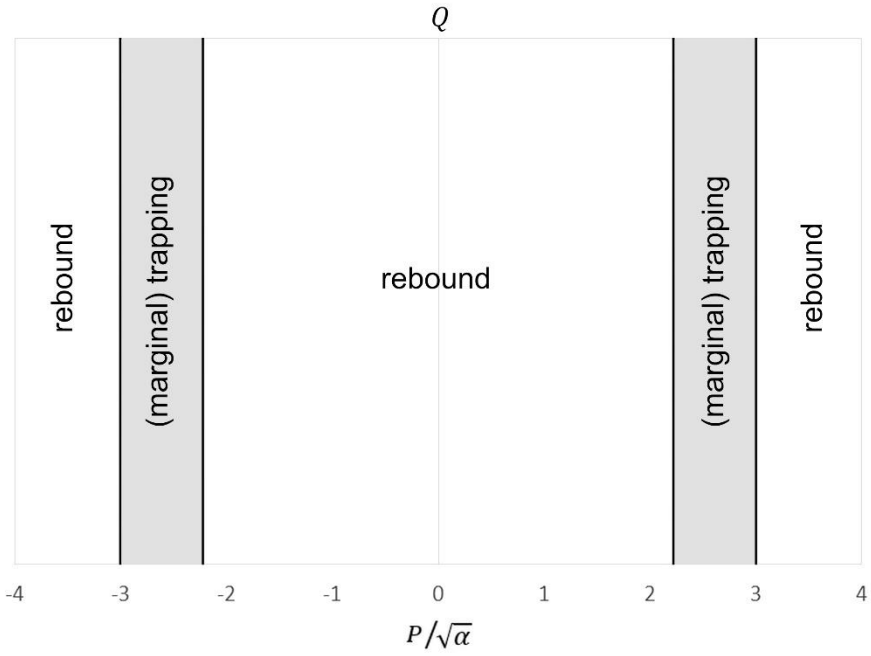

Figure 3.5. Plot summarizing the outcome of a rough sphere injected into a truncated channel for a variety of initial velocities. The region $2.2 < |P|/\sqrt{\alpha} < 3.0$ shows 'marginal trapping' for the particle making first collision with either the upper wall or the bottom wall.

3.4 Rough Sphere Dynamics between Stationary Walls

Having derived the expressions for particle motion, the particle dynamics in the 2D phase space will be analysed in this Section for two stable walls ($V = 0$). This problem was earlier raised by

Garwin [67], later studied by Travares [70] who demonstrated interesting spatial confinement that arises from the coupling of translational and rotational velocity. A 2D phase space showing the changes in translation v_t and rotation $\sqrt{\alpha}R\omega$ conveniently maps the dynamics of a particle, where the oscillations associated with the coupling behaviour may be observed. The 2D phase space maps and the trajectories in physical space [x,y] are both presented in Fig. 3.6, respectively. Four different mass distributions α of the rough sphere are chosen, for a trend between the range $2/5 \geq \alpha \geq 1/3$, that is from a core within the sphere with 1/2 radius of the whole, to a uniform solid sphere.

The oscillations in translational and rotational velocities may be observed in the left figures of Fig. 3.6, where the period τ, in number of collision, has the expression [70]

$$\tau = \frac{2\pi}{cos^{-1}(\frac{1-\alpha}{1+\alpha})} \tag{3.15}$$

For values $2/5 \geq \alpha \geq 1/3$, the period ranges from 5.57 to 6 exactly, thus it is clear that the non-integer periods result in aperiodic oscillations. From the work of Garwin [67], it had been noted that the velocity in the transverse direction of a rough sphere reverses after approximately three collisions between two parallel walls, in agreement with the period of roughly 6 collisions. Also noted by Broomhead and Gutkin [72], is the consequence of bounded oscillations between parallel walls is due to the fact that rough spheres are insensitive to perturbations, which in the elastic sphere case will result in motion away from the bounded region. This suggests that rough sphere trajectories in a stadium, that is a fully enclosed area, with parallel walls cannot be ergodic.

The result of the circular shape of the phase map due to continuous collisions of the particle show an explicit picture of translational-rotational coupling. Two conditions are essential for this coupling behaviour, the conservation of angular momentum and energy. The latter may be described as following, the centre of the circular phase map:

$$v_t^2 + \alpha(r\omega)^2 = \frac{2}{m}E \tag{3.16}$$

where E is the total kinetic energy of the particle. It follows that the circular phase spaces in Fig. 3.6 (left) have radius $\sqrt{2E/m}$. The result of translational-rotational coupling in the channel geometry is a single coupled oscillation of the two velocities. It may be observed as the mass distribution increases from solid sphere, the oscillation eventually reaches periodic orbit by the continuous closing of the gap between the start and end of the six-collision sequence. At α = 1/3, the points in the phase space concentrate at six averagely distributed points due to periodic motion.

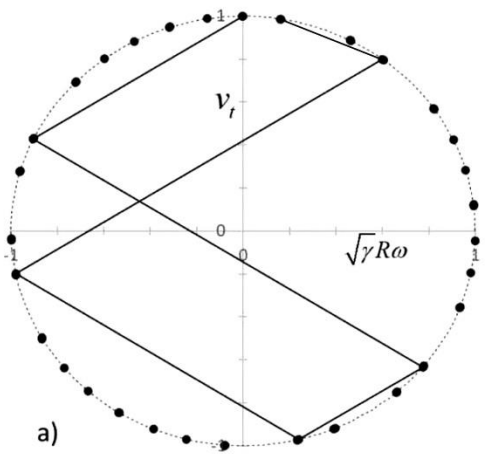
v_t
$\sqrt{\gamma}R\omega$
1
0
-1

a)

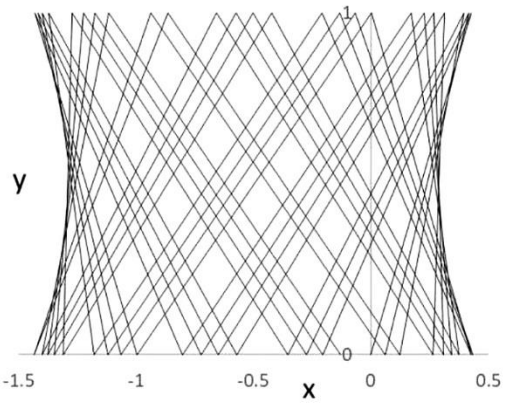
y
x
1
0
-1.5
-1
-0.5
0
0.5

b)

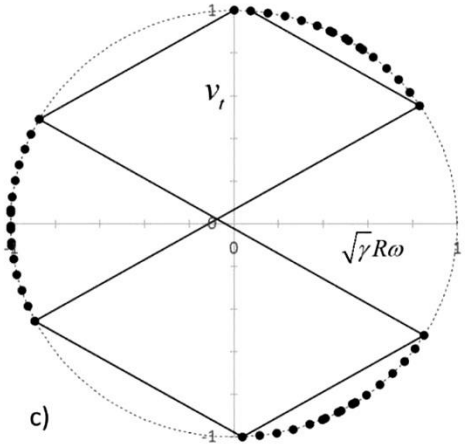
v_t
$\sqrt{\gamma}R\omega$
1
0
-1

c)

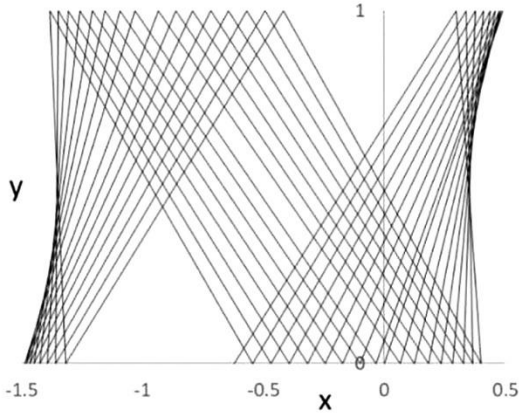
y
x
1
0
-1.5
-1
-0.5
0
0.5

d)

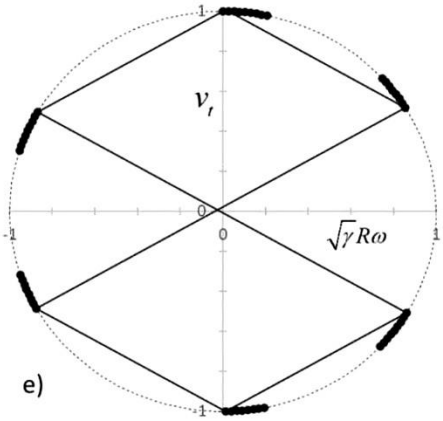
v_t
$\sqrt{\gamma}R\omega$
1
0
-1

e)

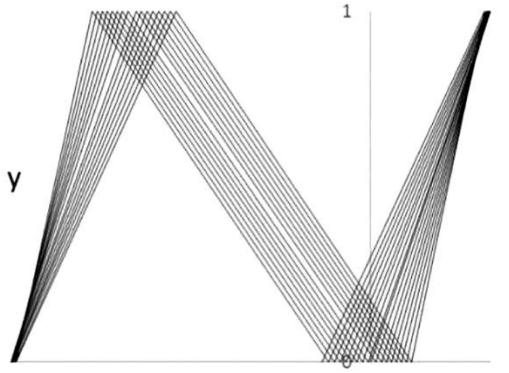
y
x
1
0
-1.5
-1
-0.5
0
0.5

f)

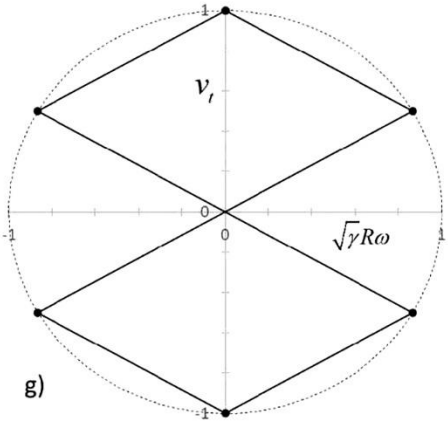
v_t
$\sqrt{\gamma}R\omega$
1
0
-1

g)

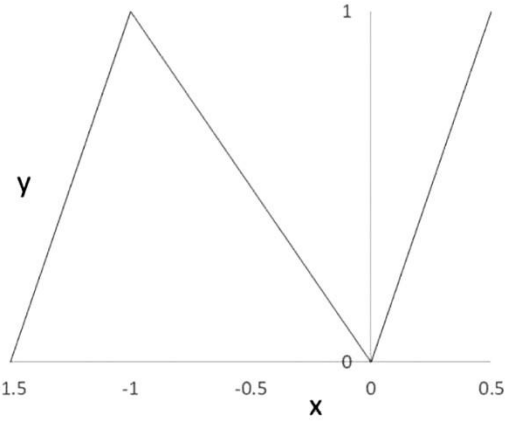
y
x
1
0
-1.5
-1
-0.5
0
0.5

h)

Figure 3.6. Phase space maps for v_t against $\sqrt{\alpha}R\omega$ (left) and trajectories in the x-y space (right) for four values of α: a) & b) 2/5 (solid sphere), c) & d) 0.3433, e) & f) 0.3367, and g) & h) 1/3 (core with 1/2 radius). Subsequent phase space points are connected with solid lines for the first six continuous collisions. The initial conditions for all cases are $v_t(0) = 1$ and $\omega(0) = 0$, and the trajectory maps have first collision with the bottom wall at position x = 0.

In each case of the phase maps, both translational v_t and rotational ω velocities have average values of zero and fluctuate about this mean, due to the non-slip boundary condition applied to the particle. This gives evidence to the fact that the non-slip condition does not apply a constraint for the translational velocity alone, but is applied to detailed coupling of translational and rotational motion during the collision.

Another clear observation is that the trajectories of the rough sphere between parallel walls is bounded along the transverse direction, due to the roughly periodic sign reversal of the transverse velocity. Fig. 3.7a) plots the spatial extent of the bounded region for various values of mass distribution α against the position of the particle at the *n*th collision Δ_n/x_1, derived in the previous Section. The bounded region shows to be roughly independent of α above the value of ~0.1, then diverges dramatically to a wider boundary. The magnitude and position of the bounded region, relative to the position of first collision, varies with the choice of initial conditions, shown in Fig. 3.7b).

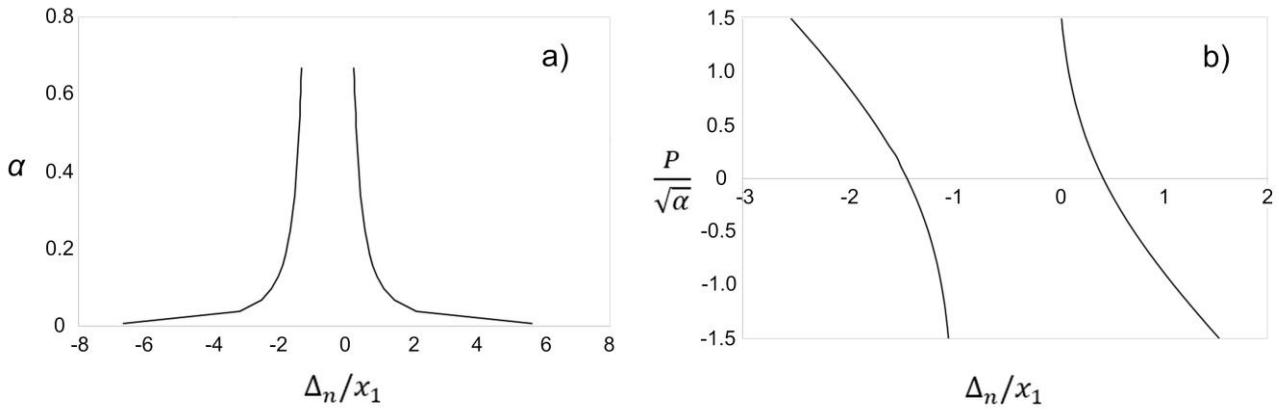

Figure 3.7. a) The bounded region of particle motion along the x axis as a function of $0 < \alpha \leq 2/3$ for initial condition $\omega(0) = 0$ with x = 0 representing the position of the first collision; b) The bounded region for the particle motion along the x axis for the solid sphere case ($\alpha = 2/5$) for a variety of initial conditions ($\frac{P}{\sqrt{\alpha}} = \frac{r\omega(0)}{v_t(0)}$).

The plot of Fig. 3.7b) demonstrates the control of position and width of the bounded domain, is another representation of the truncated channel situation discussed in the previous Section. If the end of the channel lies within the region of the particle's bounded motion, the particle will escape the channel from the same opening as injection, defined as rebound (Fig. 3.3a)). If the truncated channel fully covers the bounded region, then particle motion will be 'marginally' trapped within the parallel walls, as shown in Fig. 3.3b).

With enough samples of collision points, the non-periodic oscillations of the rough sphere between parallel walls will cover the whole circle on the 2D phase map, as shown in Fig. 3.8. The closer the value of α is to the periodic value, the greater the number of collisions required.

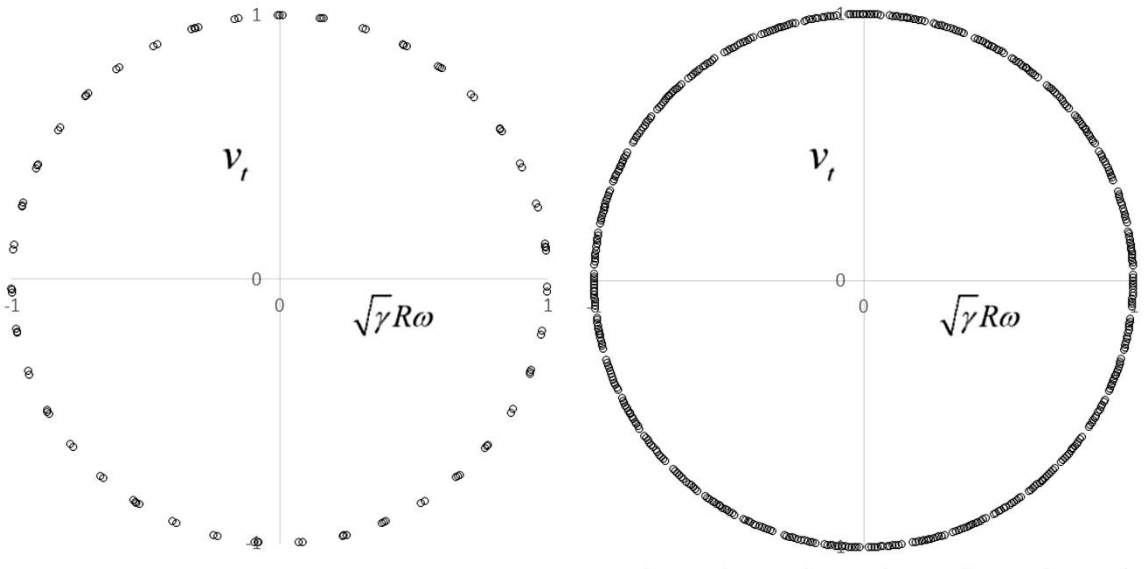

Figure 3.8. The coverage of the circular 2D phase space for 100 collisions (left) and 500 collisions (right) for the solid sphere case ($\alpha = 2/5$).

When considering the reversal of transverse velocity via the trapped motion of the rough sphere, the phenomenon arises from the change in sign of the rotational component of the particle surface velocity with each collision. The role of rough collisions against both walls is essential, where collision conditions with one rough and one smooth wall, along with two smooth walls is depicted and compared, with unchanged initial conditions, in Fig. 3.9. The latter case simply shows passing of the particle through two walls, while the former case shows change in reflection angle due to TR coupling of the particle with the rough wall, but shows no reversal of the transverse velocity, and hence no oscillations along the transverse direction.

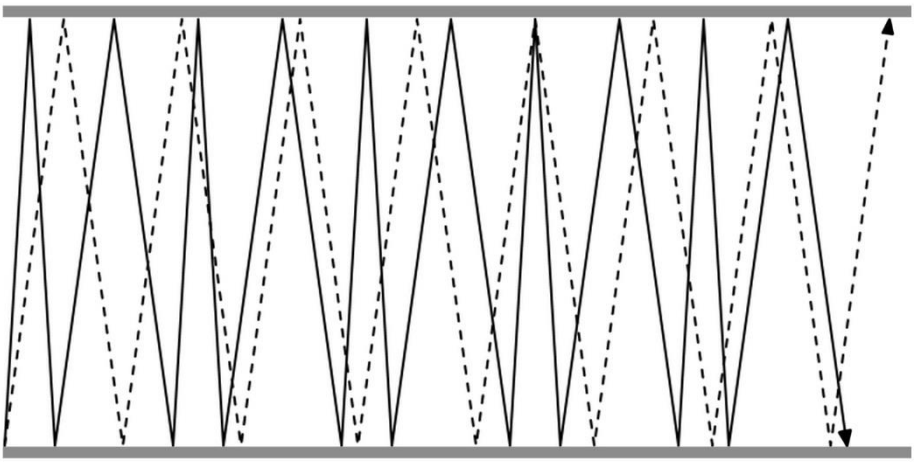

Figure 3.9. Two trajectories with unchanged initial conditions $v_t(0) = 1$ and $\omega(0) = 0$, for particle collisions with two smooth walls (dashed line), and rough bottom wall with smooth upper wall (solid line).

3.5 Rough Sphere Dynamics between Sliding Walls

The next case to consider is when the parallel walls exhibit a sliding motion ($V \neq 0$). The 2D phase space maps a variety of wall velocities are presented in Fig. 3.10 for the solid sphere case ($\alpha = 2/5$). It is clear that the phase maps still take form of circles, but the centre and radius depends on the value of V. The centre of the circular phase map in this case may be described as:

$$v_t^2 + \alpha(r\omega - V)^2 = C_o \tag{3.17}$$

where $C_o = v_t^2(0) + \alpha(r\omega(0) - V)^2$. The associated particle trajectories in the physical phase show similar transverse direction bounded oscillations as the stationary walls case, but with an extension in the bounded region as V increases.

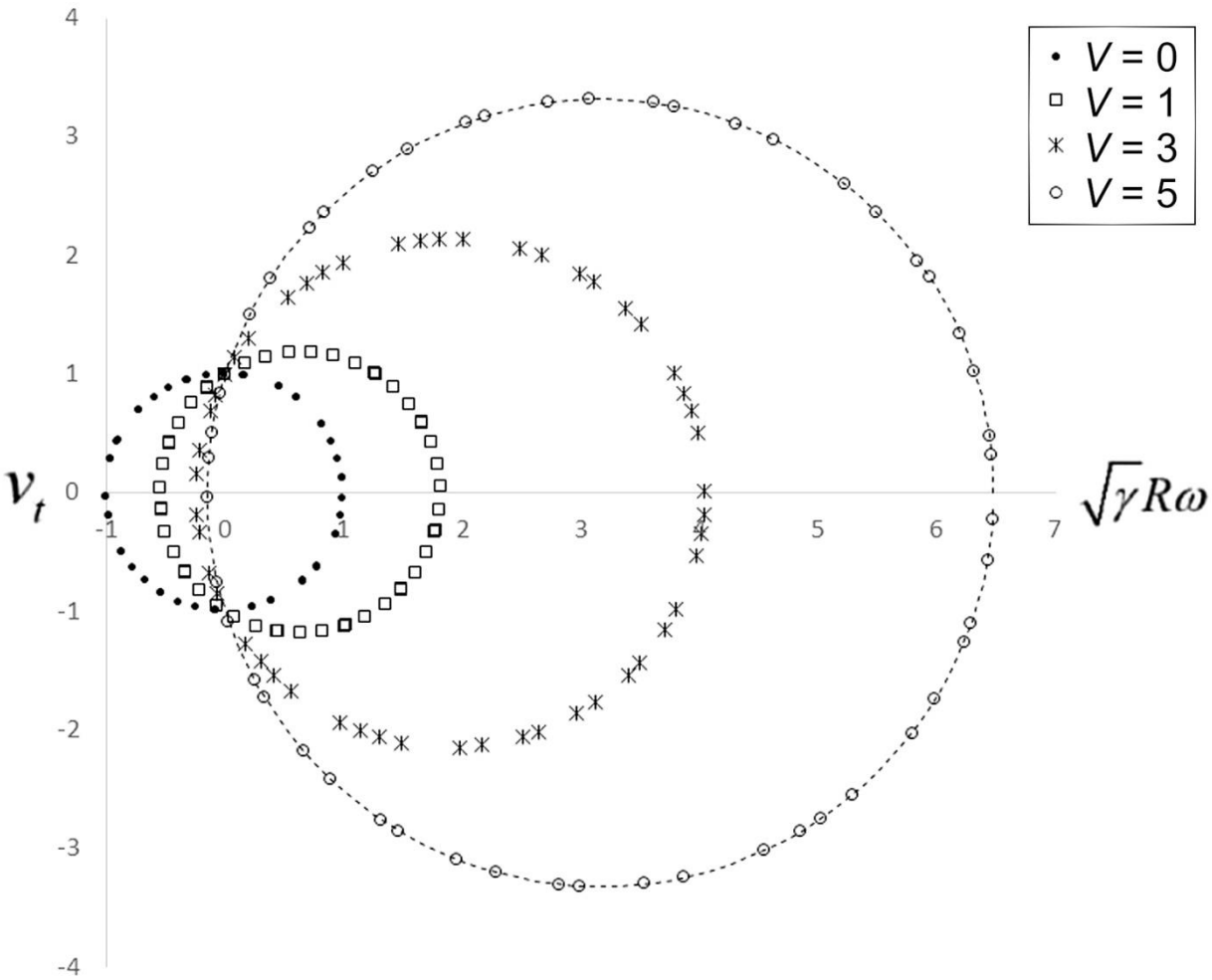

Figure 3.10. The 2D phase space maps of the rough sphere collision within sliding parallel walls with wall velocity V = 0, 1, 3, and 5 as indicated respectively. The calculated circle from Eq. 3.17 for $V = 5$ is shown in dashed line. The initial conditions are $v_t(0) = 1$ and $\omega(0) = 0$ for uniform solid sphere ($\alpha = 2/5$).

A first observation made from Eq. 3.17 is that the quantity C_o is conserved, however there was no intension for such condition. Second is from Fig. 3.10, showing a shift in the mean values of angular velocity depending on V. Yet in the kinematic equations defined due to change in reference frame (Eq. 3.9), the component related to V was the translational velocity of the rough sphere. To analyse this problem in detail, a fixed point in the phase space may be established, that is the values of the initial velocities which remains unchanged during the collision. This fixed point is defined as:

$$\begin{pmatrix} v_t(0) \\ r\omega(0) \end{pmatrix} = \begin{pmatrix} 0 \\ V \end{pmatrix} \tag{3.18}$$

which can be verified by substitution into Eq. 3.9 for both odd and even collision numbers. It is necessary to assign the wall velocity V to the rotational component, as an offset to the similar term in

v_t of Eq. 3.9. The point in Eq. 3.18 is considered fixed for both odd and even collision numbers, due to the same sign reversal of wall velocity and rotational velocity as the particle collides between top and bottom walls. An arbitrary set of equations can be written for the velocities in accordance of the fixed point:

$$\begin{pmatrix} v_t \\ r\omega \end{pmatrix} = \begin{pmatrix} 0 \\ V \end{pmatrix} + \begin{pmatrix} v_t \\ r\omega - V \end{pmatrix} \tag{3.19}$$

which results in the following equations by substitution into the kinematic equations:

$$\begin{pmatrix} v_t(i) \\ r\omega(i) - V \end{pmatrix} = M \begin{pmatrix} v_t(i-1) \\ r\omega(i-1) - V \end{pmatrix} \qquad \text{for odd } i$$

$$\begin{pmatrix} v_t(i) \\ r\omega(i) - V \end{pmatrix} = D^{-1}MD \begin{pmatrix} v_t(i-1) \\ r\omega(i-1) - V \end{pmatrix} \quad \text{for even } i \tag{3.20}$$

These equations are consistent with the case of stationary walls, where the shift in reference frame arising from the wall movement have been accounted for by the fixed point component, and therefore has disappeared from Eq. 3.20. Equations with the form of Eq. 3.20 are confirmed for the conservation of associated energy, thus Eq. 3.12 is also proven for this characteristic.

The total energy however, is not conserved when the parallel walls are in motion. Evidence is shown in Fig. 3.11a) for the plot of energy as a function of collision numbers for various V values. The total energy shows oscillation when $V \neq 0$ with a principal period of roughly 3 collisions, which is consistent with the reversal of transverse velocity as previously identified, and a longer period of roughly 25 collisions. This longer frequency corresponds to the period between every maximum (or minimum) rotational velocity.

The mean total energy plotted in Fig. 3.11b), shows quadratic increase with V according to Eq. 3.17:

$$\frac{2}{m}E = \langle v_t^2 \rangle + \alpha \langle (r\omega)^2 \rangle = 2\alpha V^2 - 2\alpha V r\omega(0) + \frac{2}{m}E_0 \tag{3.21}$$

where E_0 is the initial total energy. The proportion of energies in the translational and rotational degrees of freedom is also presented in Fig. 3.11b), where it may be observed that the increase in energy is dominated by the rotational component. Given the relation between the energies of the two degrees of freedom, an expression may be written based on Eq. 3.17:

$$\alpha \langle (r\omega)^2 \rangle = \alpha V^2 + \langle v_t^2 \rangle \tag{3.22}$$

The additional energy in the rotational degree of freedom arises directly from Eq. 3.18, the shift in the phase space fixed point. The choice of rotation in this case is due to the common symmetry with

the shear force. The implementation of non-slip condition in the microscopic level has coupled the degrees of freedom of the rough sphere to the global arrangement of the driven walls. This results in a forced spin of the particle due to interaction with the two walls.

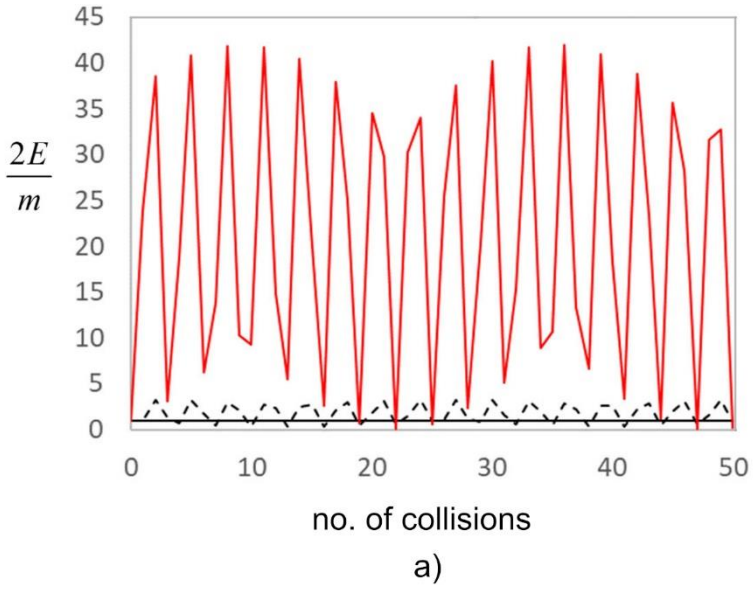

a)

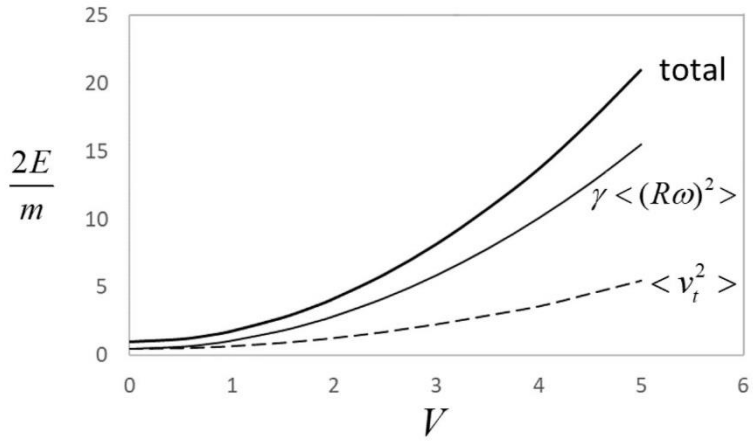

b)

Figure 3.11. a) The total energy as a function of the number of collisions for values $V = 0$(black line), 1(dashed line), and 5(red line); b) The mean of total, rotational and translational energy as a function of V. The initial conditions in all cases are $v_t(0) = 1$ and $\omega(0) = 0$ for uniform solid sphere ($\alpha = 2/5$).

Finally these results shall be compared with the expectation of flow under macroscopic non-slip boundary conditions. Since the condition focusses on the constraint in the transverse component, a

flow field $v_t(y) = -2Vy$ may be assumed, along the direction normal to the walls, then there will be $\langle v_t^2 \rangle \propto V^2$. The similar expression for the rough sphere system is:

$$\langle v_t^2 \rangle \propto (v_t^2(0) + \alpha(r\omega(0) - V)^2) \tag{3.23}$$

While both expressions describe a quadratic dependence of the translational kinetic energy on *V*, a significant difference arises from the translational-rotational coupling. In the rough sphere case, the term $\langle v_t^2 \rangle$ becomes independent of *V* when the condition rω(0) = *V* is met, noting the fact that microscopic energy transfer from the motion of the wall to the adjacent particle is controlled by the rate at which the particle surface is moving relative to the wall.

2.6 Conclusions

As described in the Introduction, more complex boundary conditions, such as shear rate dependent slip and so on, arises from the implementation of realistic physical interactions between the particle and the wall surface in the microscopic level, in comparison with the simple non-slip boundary typically applied in the modelling of macroscopic flows. It has been examined in this Chapter, a model case in which a non-slip boundary condition can be directly made use of in the microscopic level. Despite imposing explicit non-slip conditions at the level of individual collisions, much more complex behaviours is still observed in comparison with the predictions made by the usual non-slip boundary condition. For the rough sphere case, this complexity directly arises from the TR coupling that results from the non-slip kinematics, a coupling that effectively binds the translational and rotational velocities together into a single oscillatory mode. The particle being trapped along the transverse direction is a direct result of the reversal of the translational velocity, where the consequence of this transverse oscillation is observable in the rebound of a particle in the truncated channel case. It has been proved that complete trapping behaviour only remains possible for a narrow range of initial rotational velocities in the open channel case, whereas the truncated channel only exhibits ‘marginal trapping’.

No dramatic change is observed for the bounded collisions in the case of sliding walls. The result of two parallel walls moving in opposite directions with a relative velocity of 2*V* is to increase the average rotational velocity to a value of $\langle \omega \rangle = V / R$, and to alter the oscillatory component of the energy C_o as presented in Eq. 3.17. This specific selection of rotational velocity over translational for the deposition of energy, is a direct consequence of the coupling between the rotational character of the motion of the two walls and the rotation of the particle. The analysis of the influence of stick

boundaries has been restricted to the ideal gas limit in which the effect of collisions between particles can be ignored. The striking coupling that has been found between the relative velocity of the walls and the rotational velocity is a direct consequence of the unperturbed translational and rotational motion between sequential wall collisions. Molecule-molecule collisions will i) decorrelate the rotational and transverse velocities between wall collisions and ii) couple the normal velocity to the transverse translations and the rotations (something the planar walls cannot achieve) and so produce a distribution of time intervals between wall collisions. The extension of this study to include the impact of intermolecular collisions and, hence, density dependence represents an obvious subject for future work. Possible lines of study could include treating collisions using a Lorenz gas [62], by using the Boltzmann equation at low density [64,65,74] and connecting with theories [75] that include rotational velocities at the coarse-grained level of hydrodynamics.

A final observation regarding the extension of these results in particles interacting via potentials with non-zero length scales. As discussed in the previous Chapter, careful care would need to be taken when applying molecular dynamics to the rough sphere kinematics, where specifically two conditions need to be met. The first condition is that the interaction between particle and wall must generate some sort of transverse force/torque on the particle, which typically results in a transient rotational-vibrational oscillation. The second condition notes that the collision duration must be equal to the period of this transverse oscillation, otherwise the collision will result in energy dissipation. The motivation of this Chapter was the need to set aside many of the complexities arising from collisional coupling between rotations and vibrations. The results, especially the strong coupling between the sliding walls and the particle rotation, suggest that more realistic models of molecule-wall collisions may result in a surprising variety of dynamic consequences.

Chapter 4. Structural Diversity and the Spectrum of Structures between Crystal and Amorphous Order

4.1 Introduction

Glass and crystal are two typical forms of solid material which may be sketched on the same phase diagram with a liquid. However depending on the method of cooling, the two materials show explicit difference in their microscopic structures, and exhibit a number of distinct characteristics. Especially of interest in this chapter, is the difference in the arrangement of atoms and the associated local structures.

In early studies of silica glasses [76], it has been commented that silica glasses can be considered as a natural extension of crystalline silicates, where the sub-lattices SiO_2 and the modifier component are bonded together by random, instead of a layer or chain structure. The previous study [77] in the estimate of $Cu_{50}Zr_{50}$ glass has been proved to have 95 topologically distinct coordination shells. This intrinsic randomness, or namely the amorphous characteristic of glass, results in the lack of long-range order and an increase in the multiplicity of local structures. Crystals on the other hand, are typical for their periodic arrangement, and are made up of very few local structures. In 1996, Daams and Villars [78] reviewed over 4000 crystallizing compounds and found that 88% of the compounds belong to four or less environments. In a more recent study [79], over 170,000 molecular components were obtained from more than 100,000 organic crystal structures, and it was identified that roughly 60% of the molecules lie in crystal environments below five, where the single environment itself dominates over 87,000 molecules. Given these dramatically different numbers, a robust quantitative measure of the number of local structures in a material can be raised, to distinguish a crystal from a glass (without needing to establish long-range periodic order) and, potentially, distinguish one amorphous structure from another. This latter capability is of considerable interest as it would allow us to resolve the huge space of structures currently classified under the single umbrella heading of ‘disordered’.

The count of the number of local structures in a material (without regard to the actual form) shall here be referred to as a measure of the structure. Several questions can be raised regarding the large gap between the crystal and glass diversities – is there more to the structural properties of materials beyond the dichotomy of ‘crystal’ and ‘glass’? Are there structures that lie within this gap, intermediate between the ends of the structural spectrum, or are intermediate diversities a structural

‘no-man’s land’, unstable with respect to either the crystal or glass configuration? Is there an upper limit to the diversity in a crystal? A lower limit to the diversity of a glass? And just what types of structure exhibit these intermediate values of diversity? There are a diverse range of disordered materials that are known to retain a degree of regularity in their local order. These include complex oxides [80], gels [81], disordered molecular framework materials [82] and the melts of chalcogenide phase change materials [83]. This Chapter we shall explore how an explicit measure of diversity allows us to expand our description of material structure and, as a result, allows us to develop a more comprehensive framework for exploring structural stability.

The first task is to decide how to measure structural diversity of a material starting from data of the frequency with which the local structures occur [84-86]. In 2011 Kurchan and Levine [87] proposed characterising amorphous structure based on the frequencies of different classes of configurational ‘patches’. A patch is a subvolume of a configuration (typically the particles in a sphere of radius R) [88,89] and two patches are assigned the same class if, when overlayed and rotated, their respective particles can be made to overlap to within a threshold distance. The degree of order is then quantified by the complexity defined as an entropy based on the number and populations of the classes of patches. An analysis similar to the patch classification constitutes the core of standard data compression tools like the Lempil-Ziv algorithm [90] which rely on an automated version of the patch analysis to construct libraries of clusters; the smaller the library needed, the greater the data compression achieved. Martiniani, Chaikin and Levine [91] have employed this feature of data compression to generate a similar measure of structural complexity.

Patch analysis avoids the need to specify a target structure in advance (a feature celebrated as structural agnosticism) or to identify the structures of the various patch classes post analysis. This leaves something of a gap between this information theoretic perspective of structure and the more conventional geometric/topological approach that seeks to provide an explicit description of structure based on the distribution of different local structures present. Some of the attractions of this latter approach are that it assists in connecting the frequency of specific structures with the stability imparted by the particle interaction potentials, allows for analysis of frustration [92], and, generally, represents a natural extension of the conventional framework of structural analysis of materials to include amorphous solids. In this paper we develop an approach that incorporates the benefits of both approaches by adapting entropy-based measures of diversity based on explicitly identified local topological clusters.

This problem is not unique to material science. The challenge of quantifying biodiversity, that is the effective number of species, in an ecological system, is of central importance in ecological research and environmental monitoring [93, 94]. The literature on measuring biodiversity provides a

wealth of valuable ideas and insights into the problem of quantifying complex populations [95-97], here providing a brief overview. The following three distributions are representations of potentially useful approaches to characterising and classifying different distributions of local structure. Each distribution has proven useful in describing species distribution in ecologies. The three distributions are i) the lognormal distribution, originally applied to ecological data by Preston in 1948 [98]. In general, log normal distributions are associated with the distribution of a quantity arising from the product of random numbers; ii) MacArthur's 'broken stick' distribution devised in 1957 [99], which calculates the abundance of a particular species related to the length of a stick randomly fragmented; and iii) a geometric series [100] which is arrived at when the number of the top ranked species, is a fraction k of the total number of species, and the number of second ranked species is equal to k times the remaining number of individuals, and so on.

In the following Section, a brief review on the literature on measuring biodiversity will be provided, and a number of candidate definitions of diversity will be identified. These measures will be tested on a simple model of a material, the Favoured Local Structure model [101], described in Section 4.3, that allows considerable control over the structural diversity of the system and the outcomes of the fairly simple systems will be discussed in Section 4.4. Using this model, the various measures of diversity shall be tested in Section 4.5. Having selected the most reliable measure of structural diversity, Sections 4.6, 4.7 and 4.8 will examine how diversity arises from the choice of favoured local structures, and how the magnitude of the diversity determines the extended structure in the phase.

4.2 Defining Diversity

An ecological community may be characterized by the number of individuals within each species, noted by N_i for the number of individuals of species i, and $N_T = \sum_i N_i$ for the total number of individuals in the whole community. The distribution is generally represented in the following two forms. One as an abundance-rank distribution with $p_i = N_i/N_T$ plotted against the rank i, where $i = 1$ corresponds to the most frequent species, $i = 2$ for the second most frequent species, and so on. The second is in the form of $S(N)$, the number of species contained between N and $N+dN$ species.

Two general strategies have been adopted to characterise these distributions. The first is to match the distribution to a model form, where the three forms overviewed in the Introduction have proven particularly useful.

A more general characterization of a species distribution, is the idea of effective species number, defined by Hill [102] in 1973. The family of effective numbers were proposed as the following:

$$S_a = \left(\sum_{i=1}^{S_0} p_i^a \right)^{1/(1-a)} \tag{4.1}$$

where $p_i = N_i/N_T$, and a for the order of the diversity number. An associated quality arises, proposed by Renyi [103], which corresponds to a generalized entropy:

$H_a = \ln(N_a)$

When a = 0, the value S_0 directly represents the total number of species, which also may be referred to as the "richness" of a biological community, however this value gives no details in the actual distribution of species in the system. That is for two systems with equal S_0 species present, one may be dominated by a single species, while the other may have equal frequencies pi of each species. For a = 1, the equation becomes

$$S_1 = exp\left(-\sum_{i=1}^{S_0} p_i \, ln \, p_i \right) \tag{4.2}$$

where $H_1 = -\sum_{i=1}^{S} p_i \, ln \, p_i$, corresponds to the Shannon's entropy [104]. For a = 2, the equation is simply

$$S_2 = \left(\sum_{i=1}^{S_0} p_i^2 \right)^{-1} \tag{4.3}$$

which is also a form of Simpson's diversity index [105], a measure of the probability that two random individuals from the total population belong to the same species. For increasing order of a, the more common species will be increasingly weighted, until $a \to \infty$ we have $S_\infty = p_1^{-1}$ where p_1 is the frequency of the commonest species.

This definition of biodiversity S_a will be applied to characterize structural diversity of local structures, in particular for a single configuration. In Section 4.5, a value of α that balances an accurate representation of the number of species, with the benefits of filtering out noise in the generation and sampling of configurations will be chosen.

4.3 Favoured Local Structure model

In order to accomplish the aims and calculations in this project, the basic concepts from the Favoured Local Structure (FLS) model will be borrowed, which was presented in earlier works [101]. The model is set up as a triangular lattice in a 2D plane, where each site may be considered as Ising spins, either up-spin or down-spin, as representation of two different atomic species. The local environment of a site, irrespective of the sign of the site itself, is defined as the 6 nearest neighbours surrounding it, and the local structure (LS) is determined by the possible spin sequences of these 6 neighbours. It has been proved there are in total 14 distinct local structures (Fig. 4.1), which cannot be related by a rotation.

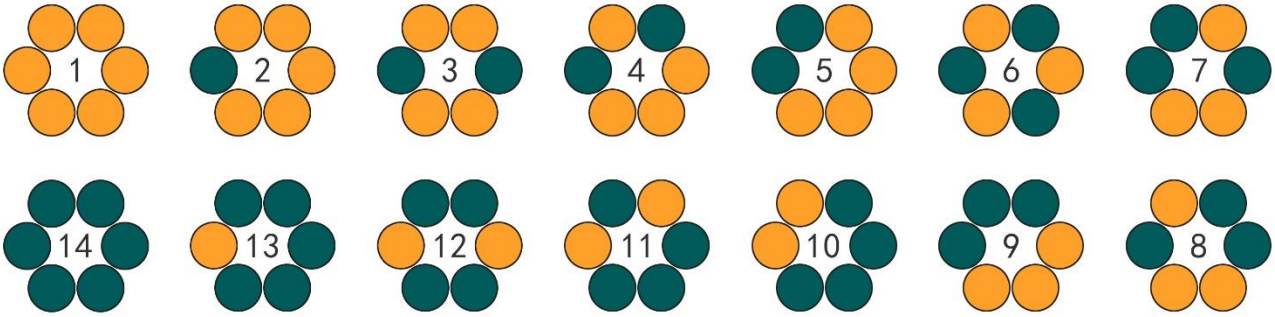

Figure 4.1. Total of 14 distinct local structures, each numbered for identification, where yellow represents up-spin and dark turquoise for down-spin. Structures {14~10} represent the inversion of the spin sequences of {1~5}, structure {8} is a chiral enantiomer of {7}, and structures {6} and {9} are unique.

In each system, the chosen favoured local structures are given an energy of -1 and an energy of 0 otherwise. In most cases where the system has low complexity, the model is carried out via the standard Metropolis Monte Carlo (MC) algorithm [106], which works as the following: 1) A random site X is chosen with uniform probability, and the sign is reversed; 2) The reversal of site X directly changes the LS of the 6 surrounding neighbours, resulting in an energy difference ΔE, which is calculated as the sum of the energies of the 6 surrounding local structures; 3) A random fraction R is chosen over an interval of [0,1), then compared with the probability of the system accepting the sign reversal, which is defined as P where

$$\mathrm{P} = \begin{cases} 1, & \Delta \mathrm{E} \leq 0 \\ \mathrm{e}^{(-\Delta E/kT)}, & \Delta \mathrm{E} > 0 \end{cases} \tag{4.4}$$

k being the Boltzmann constant and *T* is absolute temperature; 4) The sign reversal is accepted if $R \geq P$, otherwise the site remains as its original spin.

In cases with high complexity, the model is carried out via the *n*-fold way, an algorithm proposed by Bortz, Kalos and Laboweitz (BKL) [107]. Upon the basis of MC modelling, the BKL algorithm may be considered as a rejection-free method, thus highly improving the efficiency of spin flipping especially at low temperatures. Instead of directly choosing a random site with uniform probability, all sites are classified depending on the energy difference ΔE associated with the spin flip. The probability of choosing a site is therefore proportional to the weight of each class with the probability of making a successful flip, and the selected site is guaranteed a reversal in sign. Each BKL move is estimated with the equivalent number of MC cycles (1 MC cycle = N attempted moves, where N is the total number of sites in the system).

Unless otherwise noted, the simulations are performed with periodic boundary conditions, with a system size of 50*50 sites, and ground states generated with cooling from T = 1.6 at a rate of 6.25×10^{-5} per MC cycle.

4.4 Ground State Crystals

In the studies introduced by Ronceray and Harrowell [101], the ground state crystals of 1FLS structures have been identified, as shown in Fig. 4.2. The associated value S_0 is also noted, and observation can be made such that apart from FLS {1} and {14}, the total number of local structures in each ground state is larger than 1. This points out that apart from the FLS itself, extra ‘companion’ structures are included within the ground state crystals. This appearance is a direct consequence for which most structures are unable to perform perfect packing with only the FLS itself, and is referred to as the term *geometric frustration*, and has generated a considerable literature [108-110], most focusing on the role of frustration in either supressing crystal nucleation or stabilizing amorphous phases. This term will be returned to in later Sections.

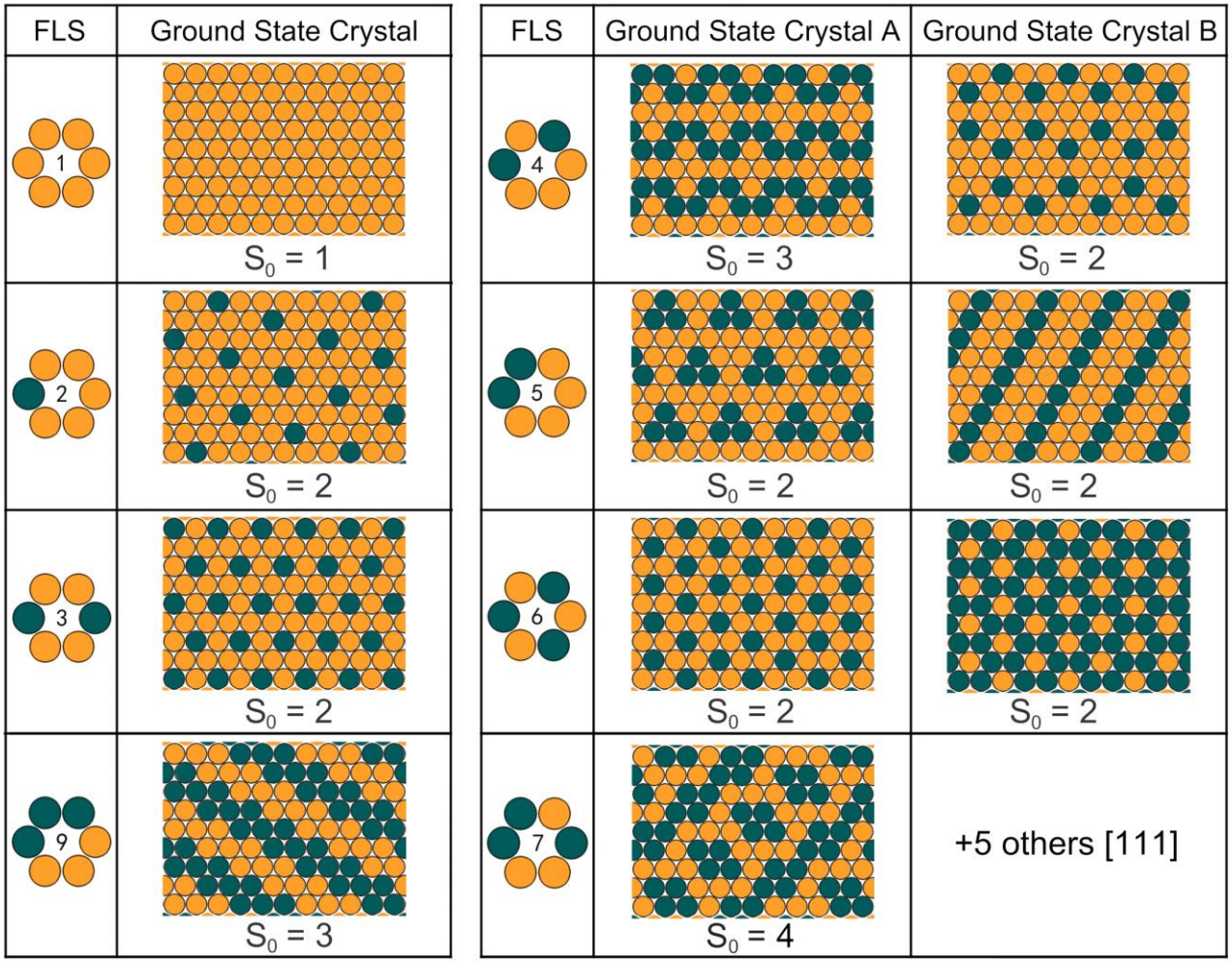

Figure 4.2. The ground state crystals of 1FLS structures (excluding structures {14~10} which form the exact same ground states as {1~5} but with an inversion of spins; the chiral enantiomer structure {8} is included in the structure of {7} with a proportion of 1:1), along with their total number of local structures S_0. Note that structures with multiple ground state crystals may have different values of S_0. Structure {7} theoretically has up to five more ground state crystals [111] but are not studied here in detail.

One clear result of the study of the 1FLS systems, both in 2D [101] and 3D [112], is that they all crystallize quite readily, irrespective of the symmetry of the FLS. To achieve a situation closer to what was found in glass forming liquids using the FLS model, systems with multiple FLS must be considered. The number of distinct systems increases rapidly with n, the number of FLS. This complexity shell be dealt by considering the n = 2 case completely, with particular focus on the new types of ground states we find.

In Fig. 4.3, all 91 possible combinations of a 2FLS system is listed, identified as one of the four structure outcomes. It may be observed that, a large proportion of systems result as 1FLS ground

state crystals, as indicated in Fig. 4.2. This outcome may be explained by the total energies, or in this case, the values of S_0 of the systems. A simple example would be the combination of {1} with any other local structure (apart from {2}, which will be discussed later). It is clear that structure {1} on its own is able to form a crystal structure with perfect packing of only up-spins via $S_0 = 1$. The addition of a second FLS into the pure up-spin system would not be difficult, since it may lie freely on any site. However, a problem arises such that when substituting one site with a second FLS, there will be up to six spin flips associated with the change, and therefore will also influence the local structures of the surrounding sites. Thus the effective number in this case, the existence of companion structures will increase the value of S_0 to a number greater than 2, via including structures that are not favoured. Considering it in the angle of total energy, inclusion of unfavoured local structures will increase the total energy to something above -1, in comparison with the pure up-spin system with total energy -1, is unfavoured. Overall, the FLS model in general will choose the ground state structure with the lowest total energy.

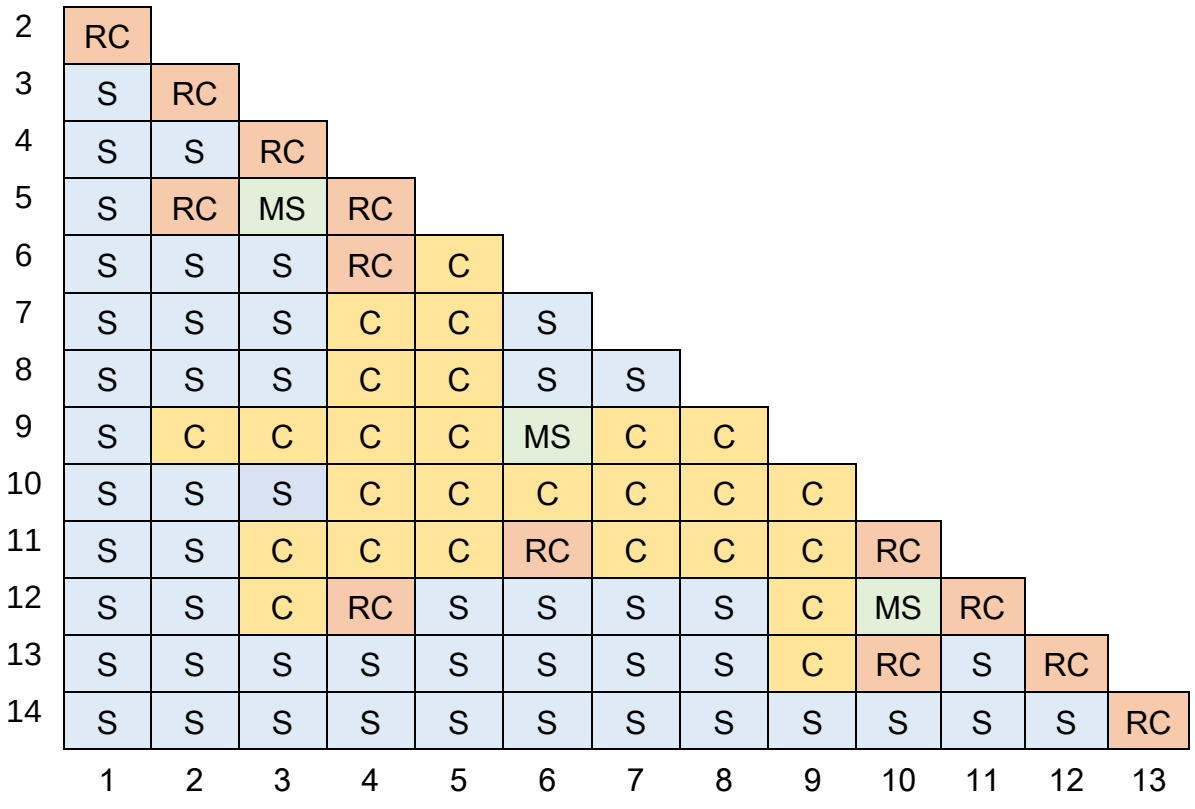

Figure 4.3. The matrix of all 91 possible combinations of 2FLS, where the numbers indicate local structures as proposed in Fig. 4.1. Ground state structures are indicated as 1FLS single crystals (S), a polycrystal of two 1FLS structures (MS), 2FLS compound crystals (C), or 2FLS random compound crystal (RC).

For cases where the 2FLS combination successfully arranges into a ground state structure with total energy lower than both of the two chosen structures' 1FLS crystal, the structure will be defined as a compound crystal. Some examples of compound crystals are shown in Fig. 4.4 where diversity maps are sketched along with ground state structures, and gives a clear vision of the associated diversity S_0 stating the total number of local structures present. From Fig. 4.3 it may be noticed that, compound structures tend to frequently appear around the centre of the table, specifically in the squared region of structures {4~11}. This phenomenon man be explained by two features, first would be the ground state energy of these 1FLS'. As noted in the Ronceray paper [101], local structures {1} ({14}), {2} ({13}), and {3} ({12}) have ground state energies below $E_0 = -2/3$, while all others are greater or equal to this value ($E_0 = -4/5$ for {7} considers both structure {7} and {8} as a whole, each structure separately has $E_0 = -1/2$). Therefore the ground state crystals of local structures {4~11} are considered less stable, and there would be a greater probability of forming a compound structure with lower ground state energy. The second feature introduces a term multiplicity g [101], which indicates the number of distinct orientations of the FLS. Apart from structure {6}, the structures {4~11} have $g = 6$, that is for each specific local structure, a rotation of 60° is unique and unable to overlap with any other degrees of rotation. This property provides freedom for these structures to arrange themselves with another FLS along the triangular lattice, thus decreasing the difficulty of the formation of a low energy ground state. Multiplicity g also gives an idea for the reason why {6} in particular forms a large amount of 1FLS crystals instead of compounds, while having a rather high energy ground state. Due to the characteristic of the spin sequence of structure {6}, there are only two unique rotations via $g = 2$, which restricts its capability of arrangement with distinct structures.

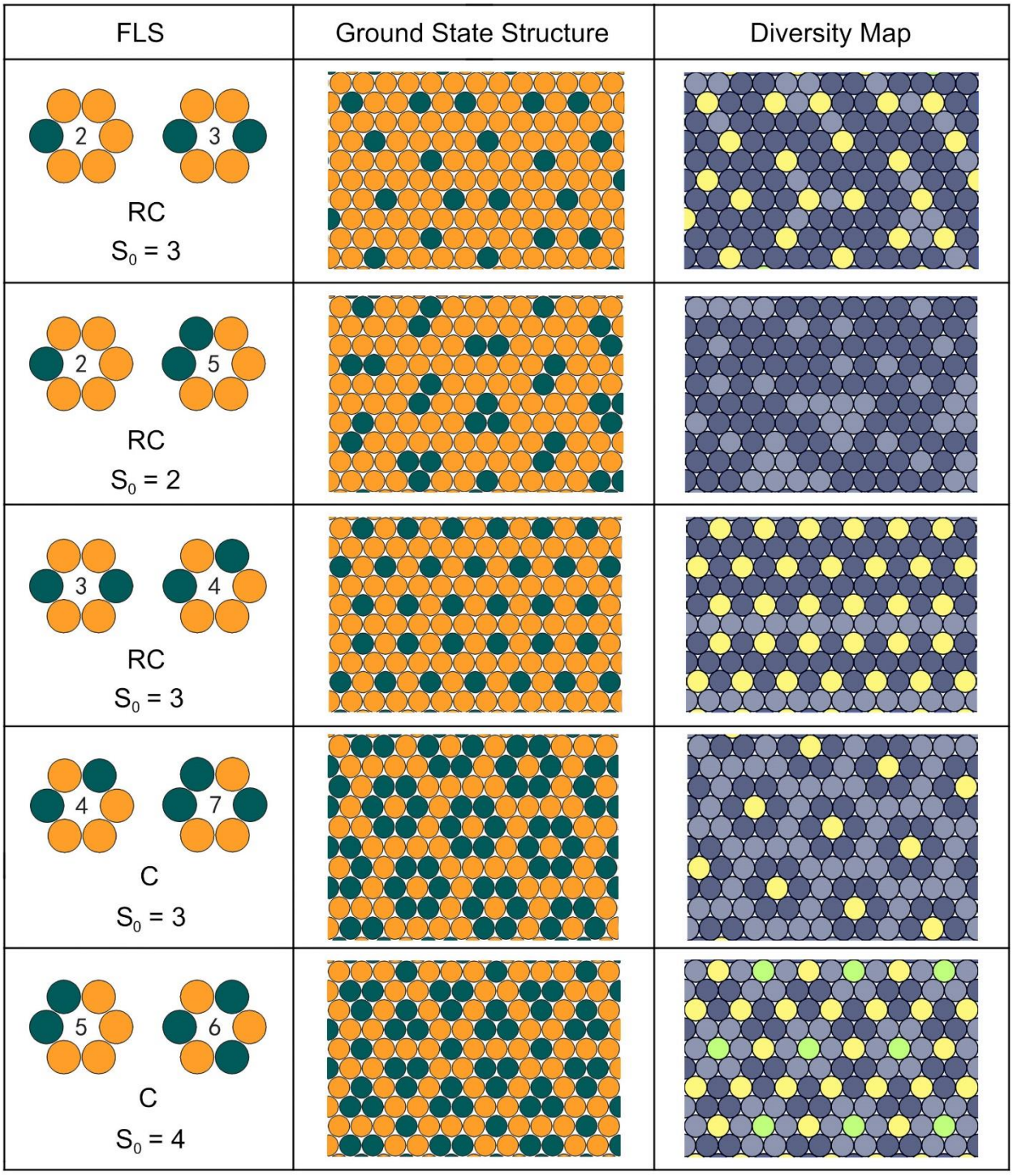

Figure 4.4. Choices of 2FLS systems, each identified as compound or random compound, along with the associated diversity values S_0. Ground state structure indicates the distribution of Ising spins, and the diversity map indicates the specific local structure of each site (blue shades for FLS choices, and bright colors for companion structures).

A more surprising result from the 2FLS model is we find randomness in the structure of a crystalline lattice. Fig. 4.4 shows examples of the ground state structures and the distribution of FLS

along with companion structures for random compound crystals. Despite the fact that there is no clear unit cell, the ground state structure exhibits low energy and is stable under low temperatures. This randomness generally takes the form of the random insertion of point fluctuations, stacking faults or in the random orientation of clusters within a crystalline framework.

4.5 Diversity and Noise

As the number of FLS is increased beyond 2, the number of model systems and the potential complexity of their ground states makes it increasingly difficult to carry out slow quenches to establish accurate ground state structures for every case. This means that we must deal with structural noise introduced by the quenches. In Fig. 4.5 an example (the {5,6} system) is presented, showing the substantial increase in S_0 with increase of cooling rate. The magnitude of the structural 'noise' introduced by fast cooling can be quantified and compared with the value of S_0 obtained via a quench with the value for the ideal crystal ground state. Since the kinetically trapped structures are likely to be few in number, some of this noise can be filtered out by using a measure of diversity that weights for the more frequent LS. In Fig. 4.5 it is shown that S_1 and S_2 exhibit significantly less dependence on the cooling rate than S_0, representing attractive alternatives as a general and effective measure of the intrinsic diversity of a structural system. One disadvantage is that, even in the case of perfect order, $S_\alpha(\alpha > 0) < S_0$ except for the case where the perfect order is characterised as equal probabilities for all structures where $S_\alpha(\alpha > 0) = S_0$.

To decide which of S_1 or S_2 is the better choice, both quantities are calculated for the 2FLS systems that are marked as C or RC in Fig. 4.3 and plotted, in Fig. 4.6, the distributions of the difference between these values and the diversity of the ideal crystals. It is found that, at the low cooling rate of 6.25×10^{-5} (see Fig. 4.6a)) that is used to generate the ground states, S_1 provides results which are closer clustered around the ideal results. At an increased cooling rate of 1.625×10^{-3}, it may be observed that S_2 provides the better estimate of the intrinsic diversity. On this basis, S_1 shall be used for the measure of diversity, but note that in cases of increased structural noise (due to fast cooling rates, uncertainty in local structure identification, etc.), S_2 or, possibly, an even higher order S_α may be more useful.

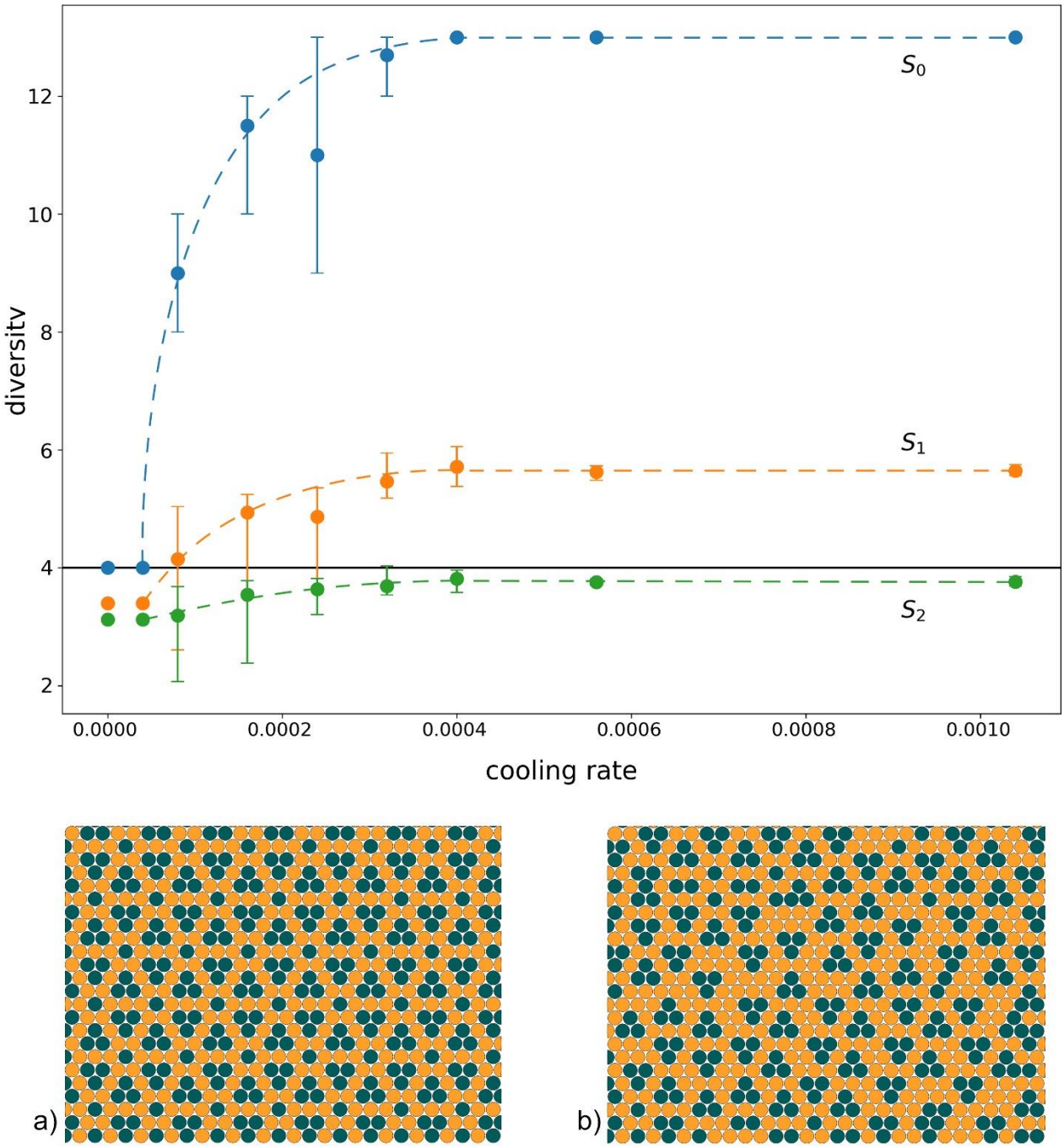

Figure 4.5. The effect on diversity S due to the change of cooling rate for 2FLS {5,6} system with a size of 40*40 sites. The values of S_0, S_1 and S_2 show logarithmic growth as the cooling rate increases, where the horizontal line at S = 4 represents the diversity for perfect ordering. Subfigures show structures a) perfect order under slow quench 6.25×10^{-5}, and b) trapped disorder due to rapid quench 1.625×10^{-3}.

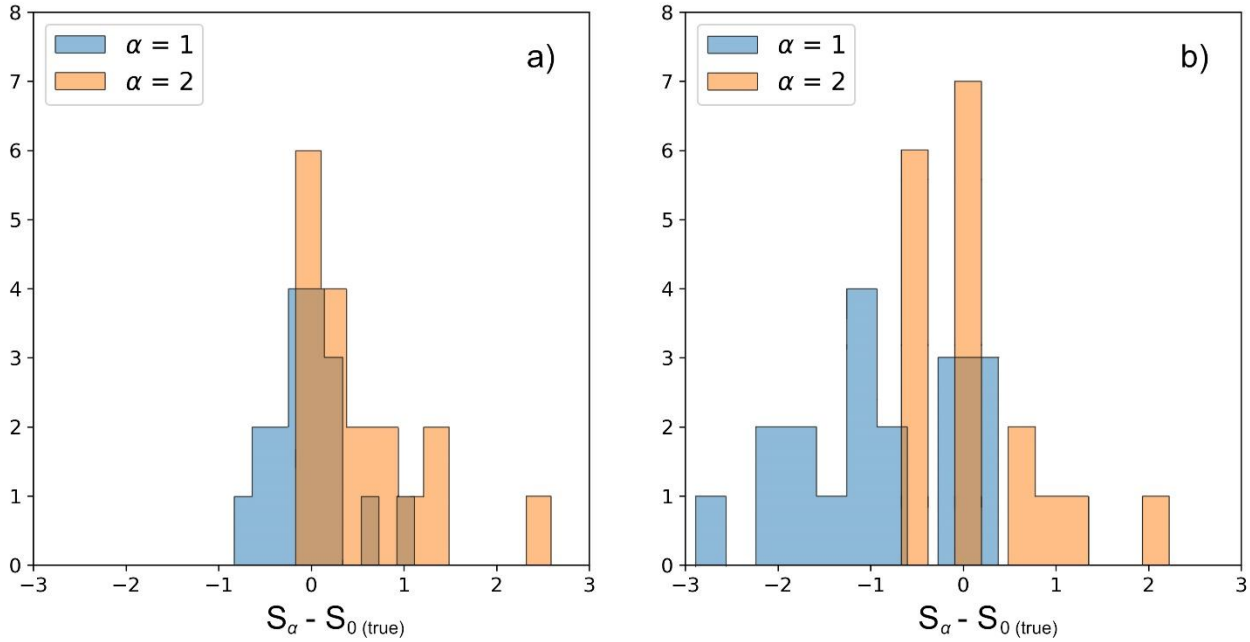

Figure 4.6. Histograms of the difference between S_a and $S_{0\,(true)}$, for a) slowest cooling rate 6.25×10^{-5} and b) fastest cooling rate 1.625×10^{-3} for compounds of 2FLS systems. Plotted are histograms for *a* = 1 and 2.

In addition to fast cooling, extra structures can be introduced into a system due to the influence of the choice of the confining shape. This influence of system size and shape is most obvious when the ground state is crystalline. In Fig. 4.7 the case of structure {9} is presented where, by varying system size, stacking faults or grain boundaries may be introduced. These extended defects can increase S_0 significantly in some cases, clearly noted in Fig. 4.7. S_1, in comparison, shows little sensitivity to these artefacts.

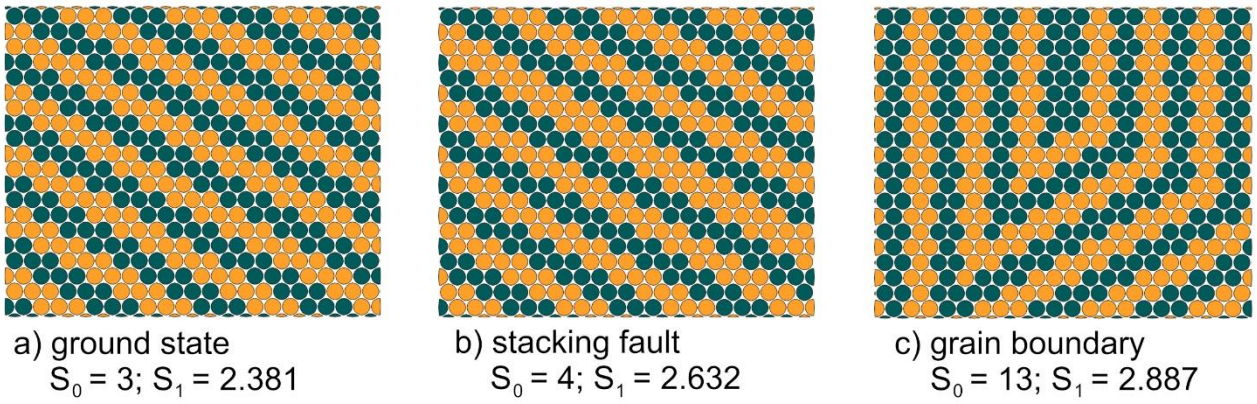

Figure 4.7. Stable states of structure {9} along with values of S_0 and S_1, showing the ideal structure and two different examples of defects due to choices of unsuitable system size.

4.6 Diversity and the Number of Favoured Local Structures

Having chosen S_1 as a measure of choice for structural diversity, a fundamental question may arise such that, what is the relationship between the Hamiltonian (the choice of FLS in this case) and the resulting structural diversity? It would be simple to imagine that the diversity is explicitly the value of n, the number of FLS. However, as already seen in the study of the 2FLS system, a system may choose to 'ignore' some FLS in favour of a more stable structure. This stable structure is built from a subset of the stable local structures, and therefore result in a diversity smaller than the actual chosen number of FLS. If systems are extended to $n > 2$, this trend could produce the structural no-man's land for intermediate diversities suggested in the Introduction.

In Fig. 4.8, the values of S_1 evaluated for nFLS model systems are presented, where n is varied from 1 to 14, the entire range of possible values. Note that only a random sampling of the possible combination of FLS for $3 \leq n \leq 12$ are included. Structures with energies within a threshold ($E < -0.97$) of the absolute minimum, $E = -1$, are indicated as black circles while the higher energy structures are plotted as red stars. It is found that the value of S_1 can differ considerably from the value of n, where i) a positive deviation of S_1 from n that is maximum at $n=2$ and decreases quickly for $n > 2$, and ii) a negative deviation of S_1 from n for larger values of n with a broad maximum around $n = 8$. Two competing effects contributing to the diversity of the ground states is observed. At low values of n, the optimised ground state includes non-favoured structures. These additional structures, which shall be called *companion structures*, are a direct consequence of geometric frustration, as evidenced by their higher energy. If the FLS are unable to completely fill the space due to geometrical incompatibility, then additional structures are inevitably required to occupy these unfilled spaces. Companion structures are, therefore, a general feature of the ground states of frustrated systems and contribute to an increase in diversity.

There is an interesting parallel between companion structures in materials and traits of biological organisms christened 'spandrels' by Gould and Lewontin [113]. Both are characterised as features that, while not intrinsically favoured, occur with an elevated frequency by virtue of filling a structural niche. The purpose of the authors of ref. [113] was to challenge the assumption that a high frequency of occurrence of a feature was direct proof of its inherent favoured status. In the same spirit, we note that the observed abundance of a local structure in low energy configurations cannot be automatically interpreted as evidence of that it corresponds to a low energy structure. As the number of FLS increase, structural niches will, increasingly, be filled by FLS's instead of companion

structures so that frustration is eliminated with increasing n. In Fig. 4.8 the frustrated structures are restricted to those plotted as red stars.

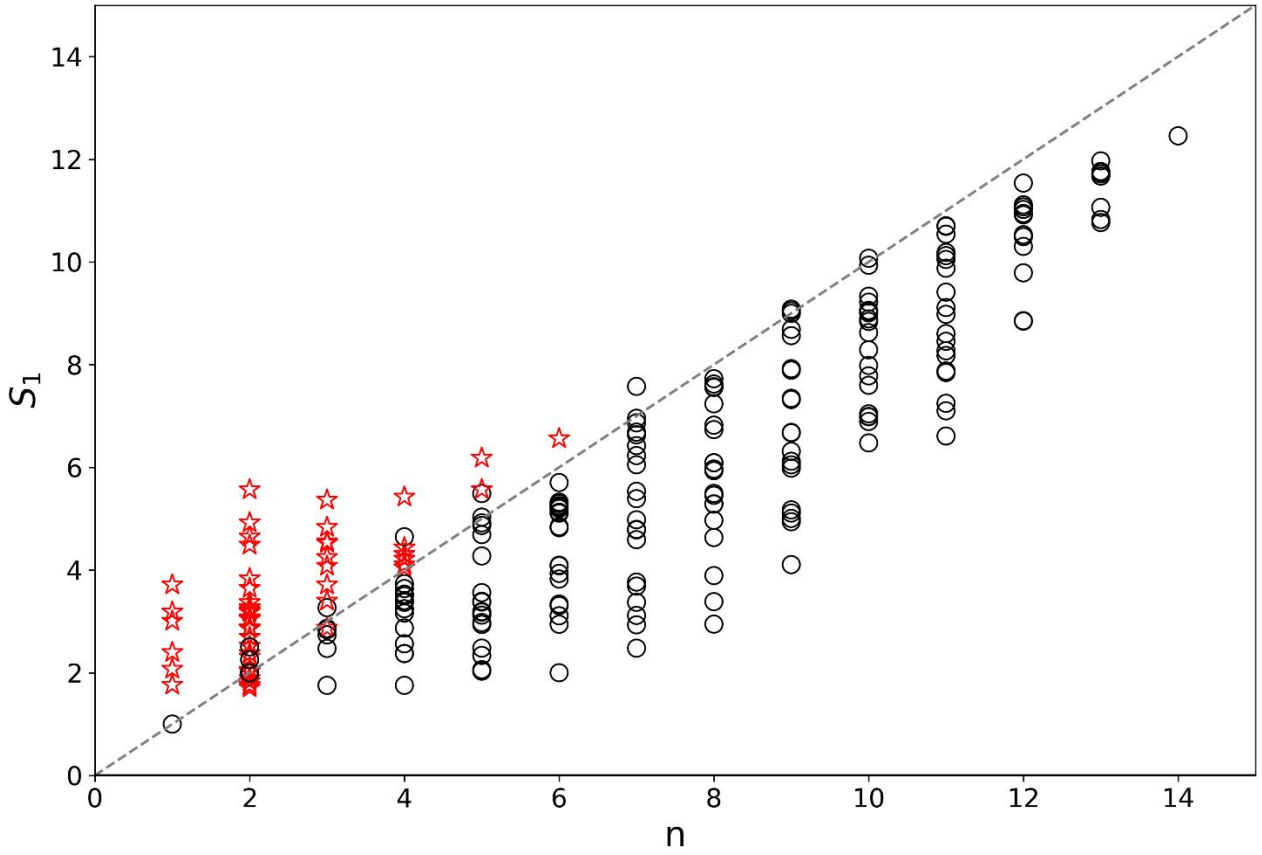

Figure 4.8. A scatter plot of the diversity S_1 plotted against the number n of favoured local structures. Structures with an energy per particle E < -0.97 are plotted as black circles. The higher energy (frustrated) structures are plotted as red stars. Note that for 2< n < 13 we have included only a randomly selected sample of the systems. The dashed line represents that case where $S_1 = n$.

The second influence on the diversity of the ground states is the 'discarding' of FLS during the generation of the ground states. Over a broad range of n, the diversity of ground states is less than the number of favoured local structures. The elimination of some favoured structures arises because they cannot be accommodated in the ground state. This behaviour is well understood when the ground state is crystalline. In the study of the 2FLS crystal ground states it is found (as shown in Fig. 4.3) that roughly 54% of the systems have formed a ground state with only one FLS present. The elimination of some FLS can be obscured in the overall diversity by the addition of companion structures. The discarding of low energy structures during cooling represents clear evidence of a cooperative structural selection process. What is intriguing about the results in Fig. 4.8 is that we see

evidence of this cooperative structural selection persisting even when the ground states have a high diversity and exhibit no obvious crystal order (as discussed in the following Section).

The relative importance of these two competing effects, via elimination of FLS' and inclusion of companion structures, can be resolved by writing S_1 in the form $S_1 = S_1(\text{FLS}) \times S_1(\text{non-FLS})$ for:

$$S_1(\text{FLS}) = exp\left(-\sum_i^n p_i \, ln \, p_i\right) \tag{4.5}$$

where the summing term is only over the FLS states, and vice versa for S_1 (non-FLS). In Fig. 4.9, the two quantities are plotted for each system (the same systems as shown in Fig. 4.8) as a scatter plot for various choices of n. Looking along the x axis, the distance between the distribution of points and the same coloured vertical line shows an idea of the degree to which a structure 'discards' FLS'. The influence of non-FLS, including the companion structures, is measured by the position on the y axis. There are two features that may be noticed from Fig. 4.9.

The first is, the discarding of FLS' is significant across the intermediate diversities. Up to 5 FLS' have been discarded by systems for n = 7, 9 and 11, consistent with the results in Fig. 4.8. This observation means that there is a significant difference in the structure of the ground state and the low temperature liquid in these systems, even though both may be amorphous.

The second is that the contribution of non-FLS' to the diversity is only significant for small values of n, that is $n \leq 5$. For larger n, S_1 (non-FLS) converges towards one and so contributes little to the local diversity. Thus it is possible to say that once there is a sufficient choice of FLS to form geometrically compatible structures, frustration is no longer a significant role within the diversity. This result also means that the non-FLS' do not play a significant role in offsetting the decrease in diversity due to the loss of FLS'.

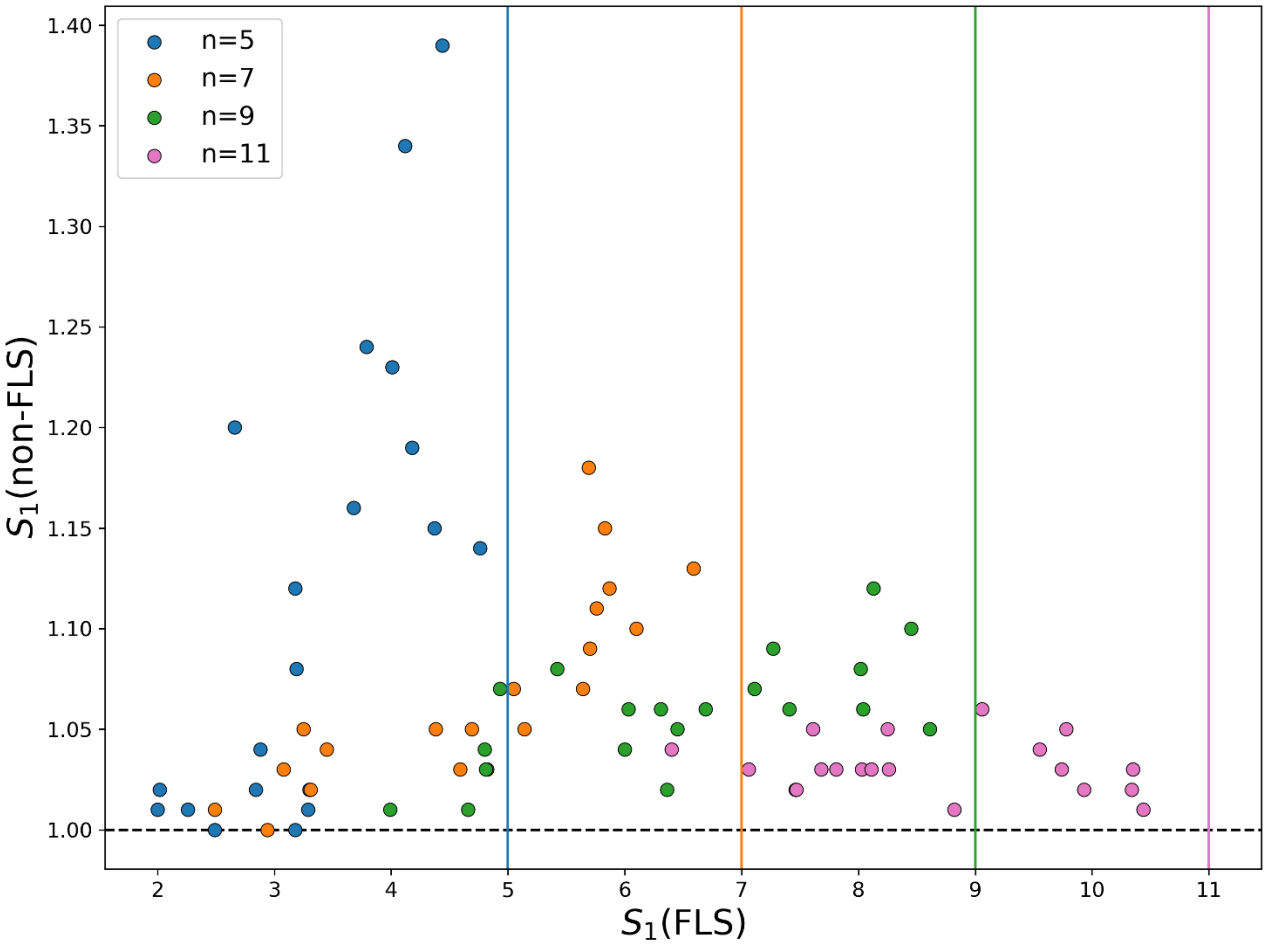

Figure 4.9. Scatter plot of S_1 (non-FLS) against S_1 (FLS) for structures with the number of FLS n = 5, 7, 9, and 11, as indicated by different colours, where the same coloured vertical line represents an estimate for the number of 'discarded' FLS. The dashed line represents S_1 (non-FLS) = 1 such that there are zero non-FLS' in the system. For local diversity $S_1 = S_1$ (FLS) × S_1 (non-FLS), the contribution from non-FLS structures diminishes as S_1 (non-FLS) approaches 1.

4.7 Diversity and Order

Here the core of the proposition such that diversity is a useful approach to characterizing complex structures shall be introduced. In the Introduction Section it was noted that crystals have a small number of local structures while glasses have a large number. So, can S_1 be interpreted as a measure of order or disorder in a material? To address this question, a second order parameter will be needed, one that can differentiate different degrees of ordering without the requirement to specify the details of this organization in advance. To this end, the spatial association of local structures over

intermediate length scales shall be looked at. The idea is that crystal, even if composed of multiple local structures, will be characterized by only a small number of groupings of these local structures. Consider a map of a state configuration in which each site is labelled by its local structure, from 1 to 14 in this case, which shall be named a *diversity map* (as previously shown in Fig. 4.4). The spatial distribution of the LS' in such a map can be quantified in a manner similar to the analysis of the structure itself, that is by calculating the effective number of local arrangements in the diversity map. The effective number of these structures that extend out to second neighbours will be referred to as the *association number.* Instead of the 14 distinct local arrangements in the structure map, the diversity map has millions of possibilities. Each site is classified in terms of the topological arrangement of local structures, which is its 6 neighbouring sites. The result is a distribution of the frequencies f_a of these distinct non-local structural states. The extended diversity Σ_a can be defined with an expression similar to local diversity,

$$\Sigma_a = \left(\sum_{j=1}^{\Sigma_0} f_j^a \right)^{1/(1-a)} \tag{4.6}$$

and the following measure will be used,

$$\Sigma_1 = exp\left(-\sum_j f_j \, ln \, f_j \right) \tag{4.7}$$

Does Σ_1 differentiate structures with different degrees of order? Faced with the wide variety of types of order in the FLS model, a qualitative answer based on visual inspection to classify structures will be relied on. It is found that ground states characterized by values of $\Sigma_1 \leq 10$ can be reasonably identified as 'simple crystals' – some examples are shown in Fig. 4.10a). Those configurations for which $\Sigma_1 \geq 200$ correspond to structures with little in the way of discernible structure that shall be characterised as 'amorphous'. That leaves the space in between, via configurations for which $10 < \Sigma_1 < 200$, examples of which have been plotted in Fig. 4.11. These structures exhibit a wide variety of complex structures – some resembling crystals with large unit cells and complex defects and others, best characterised as random networks of repeated modular units. This collection of configurations, each characterised by evidence of structural selection at a local level and disorder over longer length scales, shall be classified as *complex order*. This classification is fuzzy. It is introduced here, not as the last word in structural classification, but as a first suggestion as to how the structures of disordered materials may be differentiated. The proposed threshold values of Σ_1 does provide a simple explicit classification that is capable of capturing the *general* trends in the relationship

between order and diversity, even if the classification of borderline structures will vary with different choices of threshold. A more objective differentiation might be possible using an extension of patch repetition analysis [84,85] where one can quantify both the maximum size of repeating patterns along with the diversity of these patterns. Complex order might correspond to structures with finite sized patch that, individually, exhibit lower diversity than the system as a whole. These ideas are left for future work.

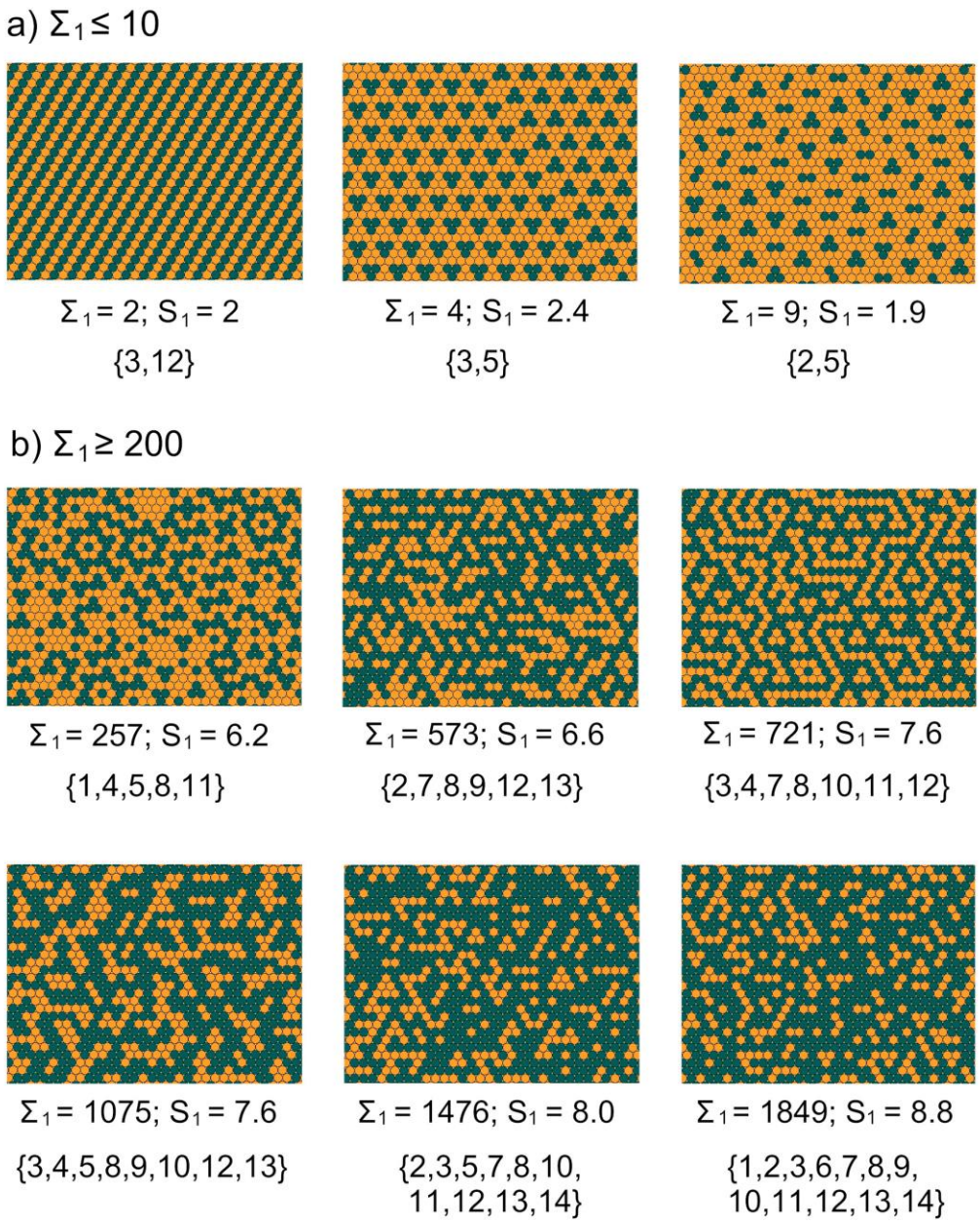

Figure 4.10. Classifying structures using the association number Σ_1. a) Examples of configuration for which $\Sigma_1 \leq 10$, classified as 'simple crystals'. b) Examples of configuration for which $\Sigma_1 \geq 200$, classified as 'amorphous'. For each configuration Σ_1, S_1 and the specific choice of FLS' are provided.

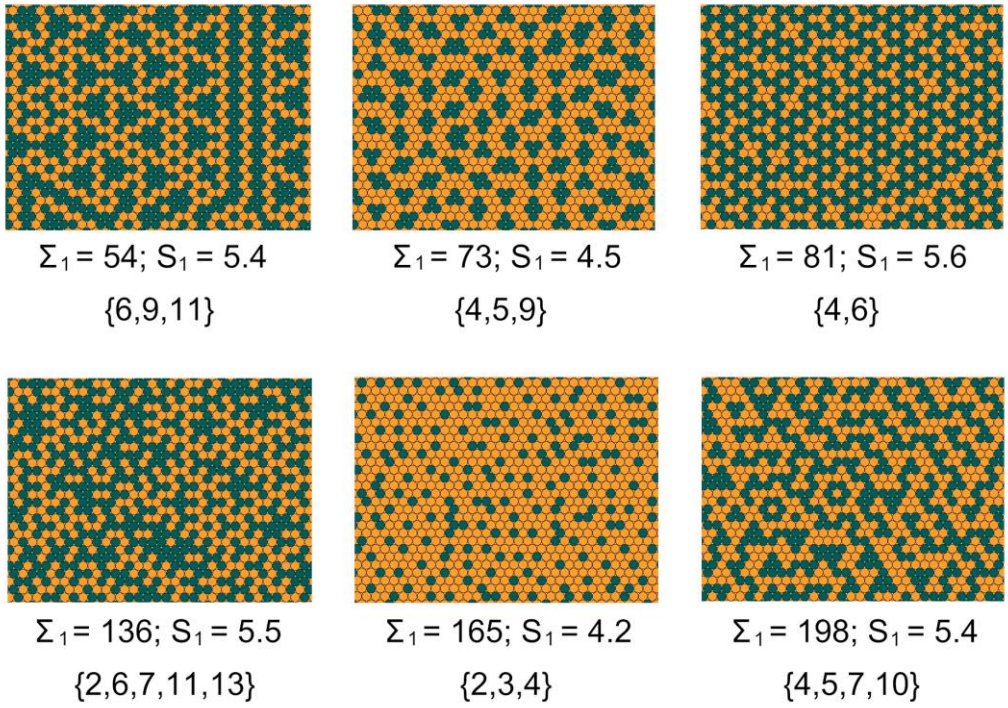

Figure 4.11. Examples of structures for which $10 < \Sigma_1 < 200$. These structures have been classified as 'complex order'. For each configurationΣ_1, S_1 and the specific choice of FLS' are provided.

The question of the relationship between diversity and order can now be addressed. Figure 4.12 presents a scatter plot of the association number, plotted as $\log_{10}(\Sigma_1)$, against S_1 for systems generated using a variety of choices of n as indicated. Three structural domains have been marked out whose boundaries are given by $\Sigma_1 = 10$ and 200, respectively. The following observations based on this data is made.

1) For $S_1 > 6$, only amorphous ground states are found. Unlike amorphous states generated by kinetic arrest during fast quenches, these amorphous ground states have energies roughly equal to that of the most stable crystal E/N = -1. Their dominance in $S_1 > 6$ materials reflects the existence of multiple options for maximally stable local arrangements directly associated with the high diversity.

2) For $S_1 > 2$, the occurrence of ground states exhibiting complex order is found. Just increasing the diversity to ~3 permits a variety of complex structures as shown in Fig. 4.11.

3) Simple crystal ground states are no longer observed for $S_1 > \sim 5$. This observation compliments the results, cited in the Introduction Section, regarding the apparent upper bound of local diversity in crystal structures. In the limited set of data analysed, the record for the maximum diversity exhibited by a simple crystal is held by a 4FLS structure with $S_1 \sim 4.5$ whose configuration is presented in Fig. 4.13a).

4) The space of structures intermediate between simple crystals and glasses - the class named as 'complex order' - lies in the diversity range of $2 < S_1 < 6$. Within this range, the diversity of a specific configuration is insufficient to identify the class of order that it belongs to. For example, for $4 < S_1 < 4.5$ examples of ground states from all three order types are observed.

5) It may be noted that within the amorphous category there is a wide range of diversity, from 4 to 13. The maximum diversity corresponds to the common representation of a glass as simply a trapped configuration of a high temperature liquid. However, the existence of *low diversity* amorphous states provides a very different material, one in which significant cooperative structural selection is involved in reaching the disordered ground state. The lowest diversity amorphous ground state found so far is shown in Fig. 4.13b) and resembles a crystal with a complex distribution of clustered point defects.

6) The dependence of $\log_{10}(\Sigma_1)$ on the diversity S_1 can be characterized by two bounding curves as shown in Fig. 4.14. The upper bound, in which $\Sigma_1 \sim S_1^{3.6}$, can be rationalized as the random filling of roughly half the nearest neighbour sites by local structures drawn from S_1 structures present. (The factor of ~ ½ accounts for the constraints associated with the overlap of neighbouring local structures.) This upper bound to other lattices can be generalized with,

$$\Sigma_1 \sim S_1^{z/2} \tag{4.8}$$

where z is the coordination number. The lower bound, in which $\Sigma_1 \sim 2.8^{S_1-1}$, shows an approach towards disorder via the stabilization of grain boundaries. At low values of Σ_1, the structures tend to form stabilized polycrystalline domains instead of point defects, due to the stabilization of grain boundaries. With increasing diversity, the selected structures appear to develop random networks. The lower bound can be generalized with the expression,

$$\Sigma_1 \sim Q^{S_1-1} \tag{4.9}$$

with Q being a fitted value.

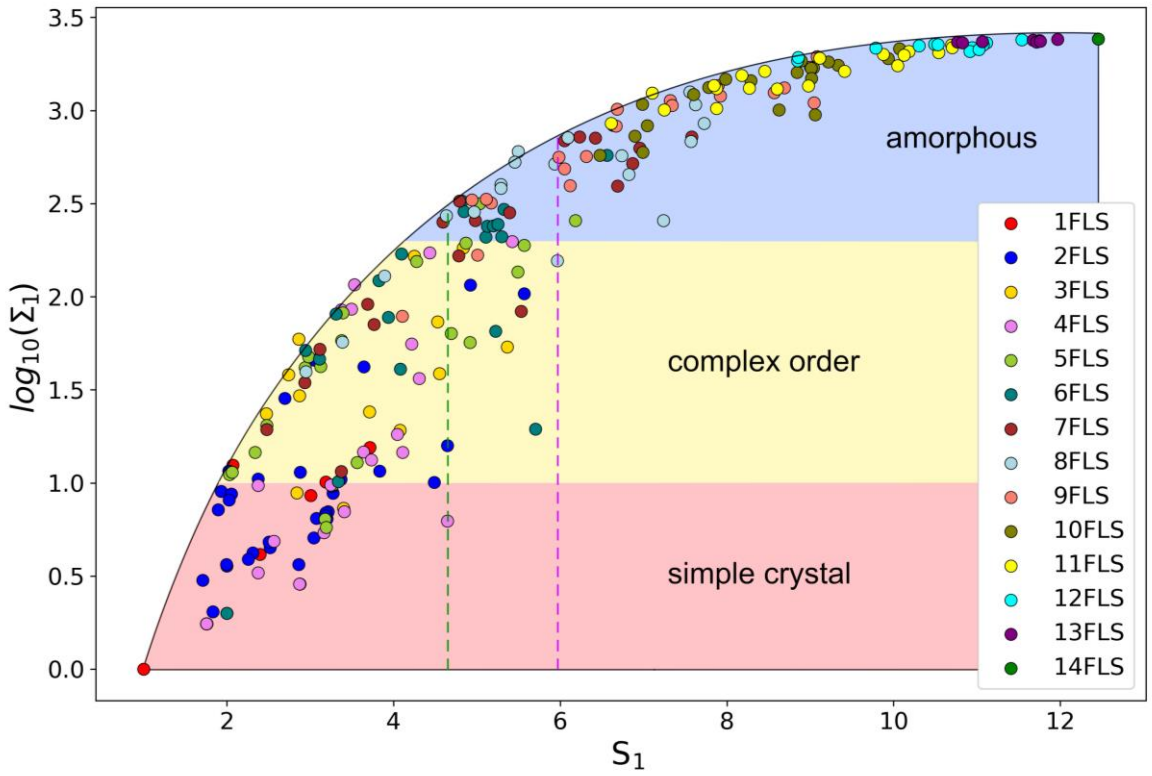

Figure 4.12. A scatter plot of $\log_{10}(\Sigma_1)$ against S_1. The three domains of order, as described in text, are indicated with colour boundaries at $\Sigma_1 = 10$ and 200. The vertical dashed green line corresponds the maximum diversity for which a simple crystal has been observed. The vertical purple dashed line corresponds the value of diversity above which all structures are amorphous. The horizontal divisions between 'simple crystal', 'complex order' and 'amorphous' and the vertical lines showing diversity bounds are fuzzy as discussed in the text.

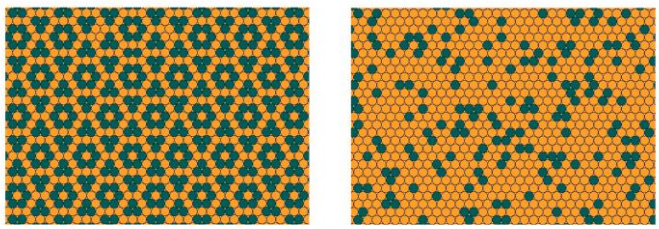

Figure 4.13. The configurations corresponding to a) the simple crystal with the maximum diversity and a unit cell size of 25 sites, and b) the amorphous state with the minimum diversity. Note that both configurations have the same value of S_1. The energy per site for structures a) and b) are E = -0.954 and -0.993, respectively. These diversity bounds depend on the fuzzy boundaries between structure types as discussed in the text.

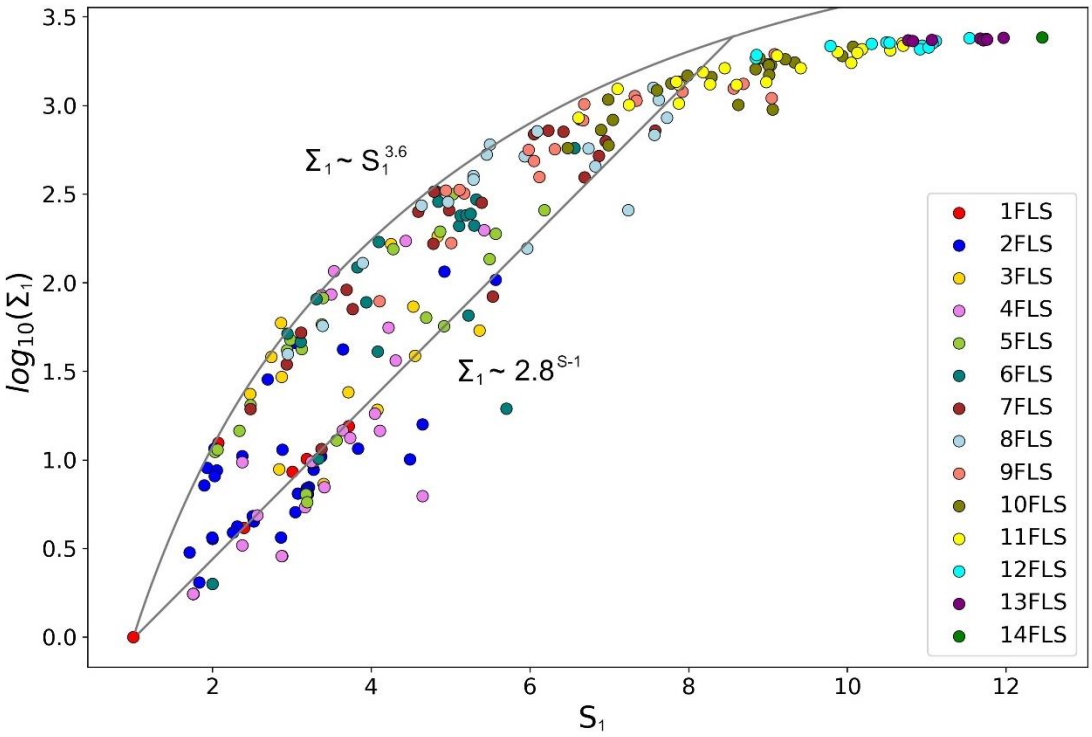

Figure 4.14. Scatter plot of $\log_{10}(\Sigma_1)$ against S_1. Data points from all values of n, the number of FLS, are depicted. Two solid lines represent empirical fits for the upper envelope (a power fit), and the lower envelope (an exponential fit).

4.8 How do Structures Incorporate Increasing Diversity: Paths from Crystal to Amorphous States

The large structural space provided by the various FLS models provide the opportunity to organize structures as progressions, that is a sequence ordered by increasing diversity, from simple crystal to amorphous states. These progressions are not intended to represent any actual physical process (e.g. transformations). Instead, they provide a means of understanding how structures can vary with diversity by taking a transect across the structural landscape. One option for this transect is the series of ground states for a sequence of models, starting with a 1FLS structure and then sequentially add FLS' until reaching the 14FLS model. There are 114673 such sequential progressions. The plot in Fig. 4.14 suggests that there are two natural choices for the progression from crystal to glass, one in which the increase in diversity follows a route of maximum Σ_1 (the 'high road') and one in which diversity increases via structures with the minimum Σ_1 (the 'low road').

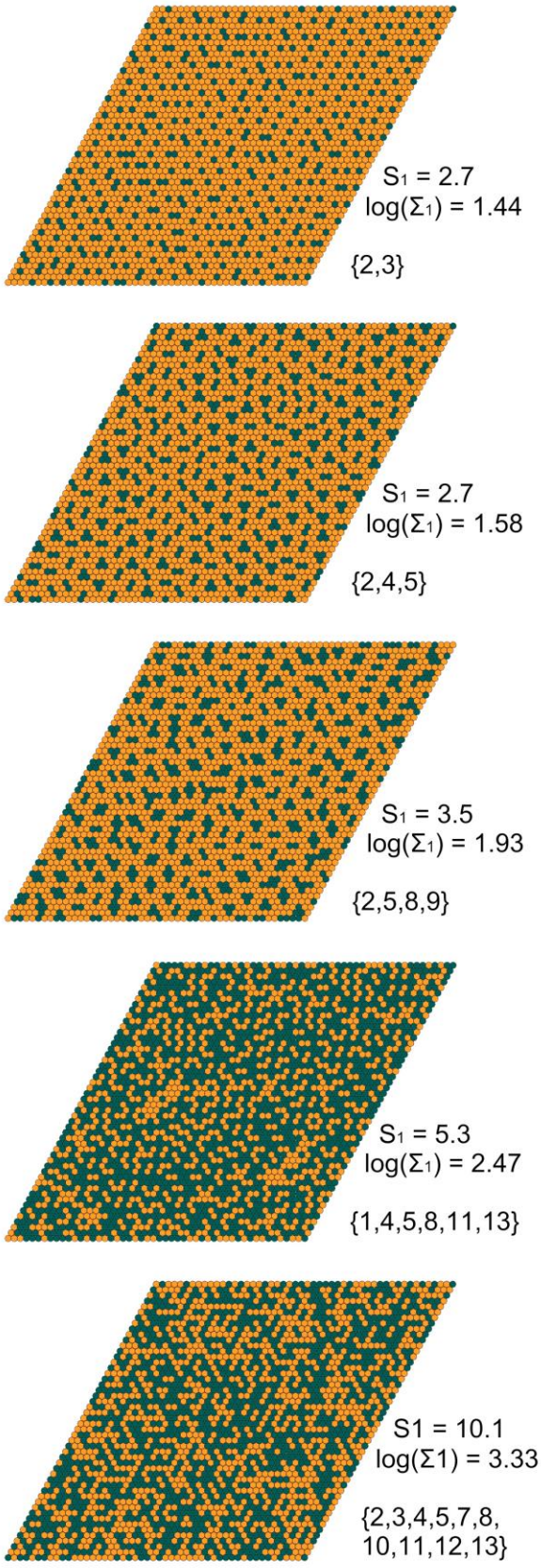

Figure 4.15. A progression of ground states of increasing diversity following a path of *maximum* Σ_1 (the 'high road'). The increase in diversity is accommodated by random inclusions. The values of $\log_{10}(\Sigma_1)$ and S_1 are shown along with the structures used to generate these images.

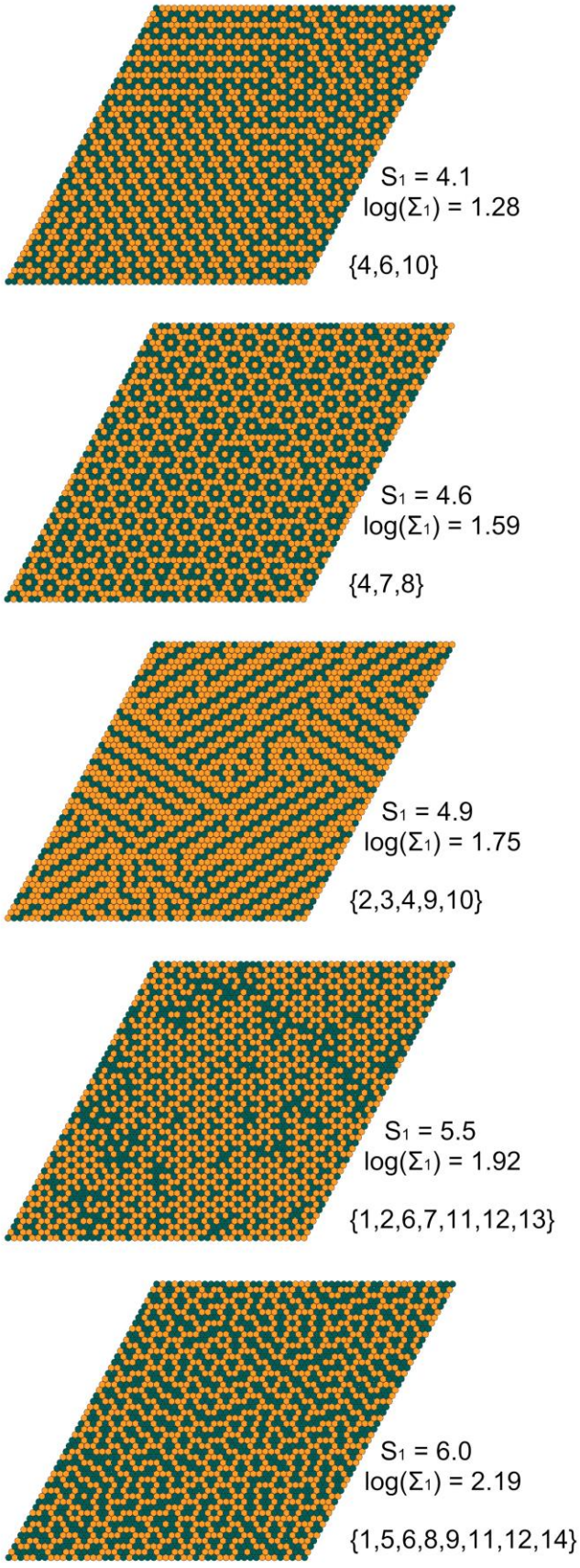

Figure 4.16. A progression of ground states of increasing diversity following a path of *minimum* Σ_1 (the 'low road'). The increasing diversity is, initially, incorporated via expanded unit cells which,

with increasing S_1, are supplemented by increasingly complex grain boundaries. The structures used to generate these images are shown.

The Figs. 4.15 and 4.16 show sequences of configurations associated with these two scenarios. It may be observed that the high road to disorder (see Fig. 4.15) proceeds by incorporating diversity in a crystal through the inclusion of defects. (Here reminding these are *low energy* 'defects' constructed from favoured local structures that disrupt the periodic order). The low diversity structures correspond to the random crystals discussed in Section 4.4. With increasing diversity, the disorder renders the idea of 'defect' meaningless. In contrast, on the 'low road' to disorder, depicted in Fig. 4.16, it is found that crystals incorporate diversity by initially increasing the size of the unit cell. There appears to be a threshold, around S_1 ~5- 6, at which the structures cross over from crystal-like to aperiodic networks consisting of modular units.

4.9 Discussion

The goal of this Chapter is to introduce the concept of structural diversity to provide a general characterization of the structure of materials, one detached from the specifics of unit cells and crystal periodicity. Some of the outcomes of this study shall be discussed as following.

The first is based on the existence of complex order. One interesting use of diversity is its capacity to characterize structures that lie between the extremes of simple crystals and the kinetically-arrested glasses. As pointed out in the Introduction Section, the list of *possible* examples of this intermediate 'complex' order includes oxide glasses [80], gels [81], disordered molecular framework materials [82] and the melts of chalcogenide phase change materials [83]. With regards the complex order exhibited by the FLS model, two qualifications are warranted. The first is to acknowledge that this group of structures will include ground states that, on slower cooling, are actually crystalline. In this case, the designation 'complex order' should, therefore, be regarded as tentative, an identification of a class of structures that do exist, at least as local minima. The second qualification concerns the role of dimensionality on the possible range of intermediate structures. As discussed in the previous Section, the upper bound of the association number Σ_1 is found to increase with S_1 as ~ $S_1^{z//2}$, where the coordination number z is the number of nearest neighbours. Using this formula, the amorphous threshold ($\Sigma_1 = 200$) at $S_1 = 5.8$ for the 2D lattice (larger than the observed value of 4.4) is reached. In the case of the 3D FCC lattice with z = 12, however, this amorphous threshold is achieved by $S_1 = 2.4$. This rapid rise in $\Sigma_1$with increasing S_1 suggests that the diversity range of possible complex

order will be significantly reduced (or even vanish) in 3D. Clearly, the limitations of the FLS model leave the question of the existence of complex order in more realistic models an interesting open question.

The second is discussion on the structural consequences of a continuous increase in diversity. In Figs. 4.15 and 4.16, two scenarios of how structure might change as the diversity increases are presented. The possibility of treating diversity as an order parameter, one capable of continuous variation, represents its particular usefulness. In considering this aspect of structural diversity, it is useful to compare this approach with defect-induced amorphization, a phenomenon that has received considerable attention and represents the simplest example of the important low temperature route to amorphous states by mechanical means. In 1992, Fecht [114] proposed a thermodynamic model for the disordering transition, analogous to thermal melting. A number of experimental studies involving either mechanical induced [115] or compositionally induced [116] defects have confirmed the first-order character of the defect induced amorphization. While the proposed diversity measure could be usefully applied to these problems, the specific results for the FLS model differs significantly from these earlier studies. The defects considered in refs. [114-116] are high energy defects that result in increasing the fictive temperature of the crystal to the point of melting. In contrast, the disorder considered in this study arises from low energy structures, resulting from changes in the Hamiltonian. Disordering arises not by destabilizing the crystal phase but, rather, by rendering it irrelevant amongst a growing population of disordered ground states with the same (or lower) energy.

4.10 Conclusions

A measure S_1 of the diversity of local structure has been introduced in this Chapter, with general applicability across all condensed states of matter: crystalline, polycrystalline, networks and glasses. It has been demonstrated that the measure, based on the Hill numbers $\{S_\alpha\}$, can be tuned to filter out (or specifically select for) structural noise. This capacity – to characterize and differentiate structures that range from ideal crystal to the 'idealized' glass (the latter being the arrested configuration of a high energy liquid) – represents a valuable tool for categorizing structures of arbitrary complexity and variety.

When applied to the ground states of the 2D FLS model, it was established that the structural diversity exhibits a continuous variation across the total accessible range. Between the low diversity crystals and the high diversity amorphous solids and the minimum diversity, an intermediate class of structures was identified, labelled complex order, that were characterised by a combination of strong

structural correlations and significant disorder. It is an interesting question as to whether these intermediate ground state structures have analogues for Hamiltonians based on realistic particle interactions. Finally, ground states were organized into sequences arranged in order of increasing diversity to explore scenarios by which crystallinity evolves into amorphous order as the number of local structures increased.

This is a preliminary study to establish of a useful measure of structural diversity. Having done so the following suggestions for new approaches to the treatment of disorder for future work may be concluded. The diversity and the relative abundances of the local structures distinguish a group of inherent structures. It would be useful to determine whether this distinguishing diversity persisted as the temperature is increased. If so, it would allow us to monitor the role of different groups of inherent structures in the structural fluctuations of supercooled liquids. There is a considerable literature in ecology in the relation between diversity and stability [117-119]. Whether analogous instabilities between diversity-defined groups of ground state structures are a feature of structural fluctuations in dense disordered phases is an intriguing possibility.

Chapter 5. Discussion and Conclusions

In Chapter 2, a simple model of a frictional sphere in collision with a single smooth wall was proposed, based on the kinematic equations of granular materials study [24]. The model aims to address the difficulties of particle anisotropy which arises from molecular scattering, by applying friction force to a spherical particle upon collision with a wall, resulting in a rotational motion of the particle due to a produced torque. The translational and rotational velocities are found to couple as vibrations with same frequency (with mean value of the rolling solution) during the collision, which refers to an exchange in energy. This characteristic of coupling may cause a dissipation in energy, but can be avoided by the adjustment of interaction parameters specific to this model. Restrictions to this current model is obvious in the fact that although meaningfully chosen, a single spherical particle is used to generally represent all anisotropies, where the actual shape of anisotropic particles is still an important aspect to consider. Another problem with single particle is that the study excludes situations where multiple anisotropies interact and collide with each other. Overall, the frictional sphere model provides details to the dynamics of particle scattering with the consideration of translational-rotational coupling, which may be regarded as a useful guide for similar studies.

In Chapter 3, the theoretical study incorporates the dynamics of ‘rough’ sphere, discussed as a result in Chapter 2. The simple model case applies a non-slip boundary condition at the microscopic level, leading to much more complex situations than that of the macroscopic case. In the stationary open channel case, the behaviour of trapping of the particle is proved possible as a result of the coupling of translational and rotational velocities in a single oscillatory mode. Due to a second coupling that arises between the rotations of the rough sphere and the shearing motion of walls, results show a sufficient increase in the average rotational velocity, and a change in the oscillatory component of energy. Similar to those restrictions noted for the previous model, this study lacks the consideration of surrounding particles, since the term ‘fluid’ in realistic fluid dynamics always refers to material with density. A linkage of this model case with realistic models would be an interesting topic for further study, since classic fluid dynamics tend to ignore microscopic dynamics and the internal molecular degrees of freedom [75].

In the previous Chapter, a simple computational code with the incorporation of the Monte Carlo method [106] and the Ising model [1] was applied to the study of structural diversity of crystals and glasses in a triangular lattice. The measure of diversity here introduced, connects with the study of biological communities in the field of ecology, and is proved to be generally applicable across all

condensed states of matter. The results established show the possibility of intermediate states between the range of ideal crystal and glass, and that these intermediate states tend to ‘discard’ certain choices of local structures in order to maintain stability. Two sequences of systems describing the progression from order to disorder were also observed throughout the analysis of a variety of ground states, suggesting that diversity may also be considered as a parameter with the capability of varying order continuously. The restrictions, again, on this simple model is the limitation of structure in two dimension, and the fixed system space on the triangular lattice. The nature of the Ising model [1] also gives rise to a restriction that only two species, either represented as +1 or –1, can be modelled within the lattice space. Although this model does not provide any details on the properties of material, neither considers the pairwise interaction between particles, it does show the capacity to explore the diversity of structure and disorder of complex materials and provide a picture of the progression within.

To conclude, this thesis has made use of simple models in the study of two very diverse topics in the field of computational studies. Despite the restrictions due to the simplicity of the models, results prove that generic questions can be answered, and they provide the possibility to guide for more complex problems.

References

1. E. Ising, Beitrag zur Theorie des Ferromagnetismus, *Z. Physik* **31**, 253–258 (1925).

2. W. Lenz, Beiträge zum Verständnis der magnetischen Eigenschaften in festen Körpern, *Z. Physik* **21**, 613-615 (1920).

3. S. G. Brush, History of the Lenz-Ising Model, *Rev. Mod. Phys.* **39**, 883 (1967).

4. R. Peierls, On Ising's model of ferromagnetism, *Proc. Cambridge Phil. Soc.* **32**, 477 (1936).

5. H. A. Kramers and G. H. Wannier, Statistics of the Two-Dimensional Ferromagnet. Part I, *Phys. Rev.* **60**, 252-263 (1941).

6. G. F. Newell and E. W. Montroll, On the theory of the Ising model of ferromagnetism, *Rev. Mod. Phys.* **25**, 353 (1953).

7. R. J. Glauber, Time-dependent statistics of the Ising model, *J. Math. Phys.* **4**, 294-307 (1963).

8. T. D. Schultz, D. C. Mattis and E. H. Lieb, Two-dimentional Ising model as a soluble problem of many fermions, *Rev. Mod. Phys.* **36**, 856 (1964).

9. A. W. Sandvik, Computational studies of quantum spin systems, In AIP Conference Proceedings, **1297**(1), 135-338 (2010).

10. A. Cervera-lierta, Exact Ising model simulation on a quantum computer, *Quantum* **2**, 114 (2018).

11. T. Preis, P. Virnau, W. Paul and J. J. Schneider, GPU accelerated Monte Carlo simulation of the 2D and 3D Ising model, *J. Comput. Phys.* **228**(12), 4468-4477 (2009).

12. N. Metropolis and S. Ulam, The Monte Carlo Method, *Am. Stat. Assoc.* **44**(247), 335-341 (1949).

13. D. H. Davis, Monte Carlo calculation of molecular flow rates through a cylindrical elbow and pipes of other shapes, *J. Appl. Phys.* **31**(7), 1169-1176 (1960).

14. G. W. King, Monte-Carlo Mrthod for Solving Diffusion Problems, *Ind. Eng. Chem. Res.* **43**(11), 2475-2478 (1951).

15. K. Binder, The Monte Carlo Method for the Study of Phase Transitions: A Review of Some Recent Progress, *J. Comput. Phys.* **59**, 1-55 (1985).

16. A. M. Ferrenberg and R. H. Swendsen, New Monte Carlo technique for studying phase transitions, *Phys. Rev. Lett.* **61**(23), 2635 (1988).

17. K. Kremer and K. Binder, Monte Carlo simulation of lattice models for macromolecules, Comput. *Phys. Rep.* **7**(6), 259-310 (1988).

18. B. J. Alder and T. E. Wainwright, Phase Transition for a Hard Sphere System, *J. Chem. Phys.* **27**, 1208-1209 (1957).

19. D. C. Rapaport, The event scheduling problem in molecular dynamic simulation, *J. Comput. Phys.* **34**, 184-201 (1980).

20. LAMMPS Molecular Dynamics Simulator, https://www.lammps.org/#gsc.tab=0, Sandia National Laboratories (accessed 28, Feb, 2024).

21. V. Salmaso and S. Moro, Bridging Molecular Cocking to Molecular Dynamics in Exploring Ligand-Protein Recognition Process: An Overview, *Front. Pharmacol.* **9**, 923 (2018).

22. R. C. Bernardi, M. C. R. Melo and K. Schulten, Enhanced sampling techniques in molecular dynamics simulations of biological systems, *Biochim. Biophys. Acta.* **1850**(5), 872-877 (2015).

23. Q. Ke, X. T. Gong, S. W. Liao, C. X. Duan and L. B. Li, Effects of thermostats/barostats in physical properties of liquids by molecular dynamics simulations, *J. Mol. Liq.* **365**, 120116 (2022).

24. P. A. Cundall and O. D. L. Strack, A discrete numerical model of granular assemblies. *Géotechnique* **29**, 47-65 (1979).

25. J. D. Doll, Simple classical model of the scattering of a diatomic molecules from a solid surface. *J. Chem.Phys.* **59**, 1038-1042 (1973).

26. I. T. Elsum and R. G. Gordon, A kinematic, classical mechanical theory of reactive collisions. *J. Chem. Phys*. **76**, 3009-3018 (1982).

27. R.B Gerber, Molecular scattering from surfaces: Theoretical methods and results. *Chem. Rev.* **87**, 29-79 (1987).

28. A. J. McCaffery, A new approach to molecular collision dynamics. *Phys. Chem. Chem. Phys.* **6**, 1637-1657 (2004).

29. M. Bonfanti and R. Martinazzo, Classical and quantum dynamics at surfaces: Basic concepts from simple models. *Int. J. Quant. Chem*. **116**, 1575-1602 (2016).

30. W. L. Nichols and J. H. Weare, Rotational energy distributions for homonuclear diatomic beams scattered from solid surfaces: A hard-cube model. *J. Chem. Phys.* **66**, 1075-1078 (1977).

31. R. Cross, The bounce of a ball. *Amer. J. Phys.* **67**, 222 (1999).

32. R. Cross, Tennis physics, anyone? *Phys. Today* **61**, 84 (2008).

33. G. Robinson and I. Robinson, The motion of an arbitrarily rotating spherical projectile and its application to ball games. *Physica Scripta* **88**, 018101 (2013).

34. N. Maw, J. R. Barber and J. N. Fawcett, The oblique impact of elastic spheres. *Wear* **38**, 101-114 (1976).

35. W. J. Stronge, Rigid body collisions with friction. *Proc. R. Soc. Lond. A* **431**, 169-181 (1990).

36. D. E. Stewart. Rigid-body dynamics with friction and impact. *SIAM Rev.* **42**, 3-39 (2000).

37. S. D. Lee and J. Song, Sensorless collision detection based on friction model for a robot manipulator. *Int. J. Precis. Eng. and Manuf.* **17**, 11-17 (2016).

38. I. Cook, Newton's 'experimental' law of impacts. *The Math.Gazette* **70**, 107-114 (1986).

39. W. J. Stronge, *Impact Mechanics* (Cambridge U.P. Cambridge 2004).

40. R. Zwanzig, Rotational friction coefficients of a bumpy cylinder with slipping and sticking boundary conditions. *J. Chem. Phys.* **68**, 4325-4326 (1978).

41. H. P. Zhu, Z. Y. Zhou, R. Y. Yang and A. B. Yu, Discrete particle simulation of particulate systems: A review of major applications and findings. *Chem. Eng. Sci.* **63**, 5728-5779 (2008).

42. L. E. Sibert, D. Ertas, G. S. Grest, T. C Halsey, D. Levine and S. J. Plimpton, Granular flow down an inclined plane: Bagnold scaling and rheology. *Phys. Rev. E* **64**, 051302 (2001).

43. Plimpton, S. J. Fast parallel algorithms for short-range molecular dynamics. *J. Comp. Phys.* **117**, 1–19 (1995).

44. F. S. Crawford, Dynamics impedance matching with a lever, *Amer. J. Phys.* **57**, 52-56 (1989).

45. R.L.Garwin, Kinematics of an ultraelastic rough ball. *Amer. J. Phys.* **37**, 88-92 (1969).

46. S. Chapman and T. G. Cowling, *The mathematical theory of non-uniform gases.* (Cambridge UP, London, 1953), Chp. 11.

47. J. Odell and B. J. Berne, Molecular-dynamics of rough sphere fluid 1. Rotational relaxation. *J. Chem. Phys.* **63**, 2376-2394 (1975).

48. B. J. Berne and J. A. Montgomery, Coupling between translational and rotational motions, *Mol. Phys.* **32**, 363-378 (1976).

49. J. A. Montgomery and B. J. Berne, Viscoelastic theory of angular velocity correlation function. *J. Chem. Phys.* **66**, 2161-2165 (1977).

50. https://www.youtube.com/watch?v=0Vk7Qm87hUw (accessed 20, Jan, 2024)

51. H. Brody, That's how the ball bounces, *Phys. Teach.* **22**, 494-497 (1984).

52. C. L. M. H. Navier, Mémoire sur les lois du mouvement des fluids. Mémoires del'Académie Royale des Sciences de l'Institut de France **6**, 389–440 (1823).

53. E. Ruckenstein and P. Rajora, On the no-slip boundary-condition of hydrodynamics. *J. Colloid Interface Sci.* **96**, 488 (1983).

54. P. A. Thompson and S. M. Troian, A general boundary condition for liquids flow at solid surfaces. *Nature* **389**, 360 (1997).

55. Y. Zhu and S. Granick, Limits of the hydrodynamic no-slip boundary conditions. *Phys. Rev. Lett.* **88**, 106102 (2002).

56. C. Neto, D. R. Evans, E. Bonaccuro, H.-J Butt and V. S. J. Craig, Boundary slip in Newtonian liquids: a review of experimental studies. *Rep. Prog. Phys.* **68**, 2859-2897 (2005).

57. G. H. Bryan, *Rep. Br. Advmt. Sci.* p.83 (1894).

58. F.B.Pidduck, The kinetic theory of a special type of rigid molecule. *Proc. R. Acad. Soc. A* **101**, 101(1922).

59. E. W. Condiff, Weu-Kao Lu, and J. S. Dahler, Transport properties of Polyatomic Fluids: A dilute gas of perfectly rough spheres. *J. Chem. Phys.* **42**, 3445 (1965).

60. B. J. McKoy, S. I. Sandler, and J. S. Dahler, Transport properties of polyatomic fluids: 4. Kinetic theory of a dense gas of perfectly rough spheres. *J. Chem. Phys* **45**, 3485 (1966).

61. S. Chapman and T. G. Cowling, *Mathematical theory of non-uniform gases* 3rd Ed. (Cambridge University Press, Cambridge, 1970).

62. L. Waldmann, Kinetische theorie des Lorentz-gases aus rotierenden molekülen. *Zeitschrift für Naturforschung A* **18**, 1033 (1963).

63. J. O'Dell and B. J. Berne, Molecular dynamics of the rough sphere fluid. I. Rotational relaxation. *J. Chem. Phys.* **63**, 2376 (1975).

64. O. Kravchenko and M. Thachuk, The effect of rotational and translational energy exchange on tracer diffusion in rough hard sphere fluid. *J. Chem. Phys.* **134**, 114310 (2011).

65. O. Kravchenko and M. Thachuk, Transport properties of the rough hard sphere fluid. *J. Chem. Phys.* **136**, 044520 (2012).

66. G. L. Strobel, Matrices and superballs. *Am. J. Phys.* **36**, 834-837 (1968).

67. R. L. Garwin, Kinematics of the ultraelastic rough ball. *Am. J. Phys.* **37**, 88-92 (1969).

68. 'Superball' is the brand name of a highly elastic synthetic rubber ball invented by N. H. Stingley in 1964 and first sold by Wham-O in the late 1960's.

69. B. T. Hefner, The kinematics of a superball bouncing between two vertical surfaces. *Am. J. Phys.* **72**, 875-883 (2004).

70. J. M. Travares, The elastic bounces of a sphere between two parallel walls. *Am. J. Phys.* **75**, 690-695 (2007).

71. R. Cross, Bounce of a spinning ball near normal incidence. *Am. J. Phys*. **73**, 914 (2005).

72. D. S. Broomhead and E. Gutkin, The dynamics of billiards with no-slip collisions. *Physica* D **67**, 188-197 (1993).

73. C. Cox, R. Feres and J. -K. Zhang, Stability of periodic orbits in no-slip billiards. *Nonlinearity* **31**, 4443 (2018).

74. M. M. Kratzer, S. K. Bhatia and A.Y. Klimenko, Knudsen layer behaviour and momentum accommodation from surface roughness modelling, *J. Stat. Phys*. **190**,63 (2023).

75. J. S. Hansen, B. D. Todd and P. J. Daivis, Dynamical properties of a confined diatomic fluid undergoing zero mean oscillatory flow: Effect of molecular rotation. *Phys. Rev. E* **77**, 066707 (2008).

76. G. N. Greaves, A. Fontaine, P. Lagarde, D. Raoux, & S. J. Gurman, Local Structures of silicate glasses, *Nature* **293**, 611-616 (1981).

77. D. Wei, J. Yang, M. Q. Jiang, L. H. Dai, Y. J. Wang, J. C. Dyre, I. Douglass and P. Harrowell, Assessing the utility of structure in amorphous materials, *J. Chem. Phys.* **150**, 114502 (2019).

78. J.L.C. Daams and P.Villars, Atomic environment classification of the tetragonal 'intermetallic' structure types, *J. Alloys Comp.* **252**, 110-14 (1997).

79. Z. F. Weng, W. D. S. Motherwell, F. H. Allen, J. M. Cole, Conformational variability of molecules in different crystal environments: a database study, *Acta. Cryst. B.* **64**, 348-362 (2008).

80. M. Baise et al, Negative hydration expansion in $ZrWO_8$: Microscopic mechanism, spaghetti dynamics, and negative thermal expansion. *Phys. Rev. Lett.* **120**, 265501 (2018).

81. C. P. Royall, M. A. Faers, S. L. Fussell and J. E. Hallett, Real space analysis of colloidal gels: triumphs, challenges and future directions. *J.Phys.: Cond. Matt.* **33**, 453002 (2021).

82. T. D. Bennett, et al, Structure and properties of an amorphous metal-organic framework. *Phys. Rev. Lett.* **104**, 115503 (2010).

83. M. Schumacher, et al, Structural, electronic and kinetic properties of the phase-change material $Ge_2Sb_2Te_5$ in the liquid state. *Sci. Rep.* **6**, 27434 (2016).

84. M. Tanemura, Y. Hiwatari, H. Matsuda, T. Ogawa, N. Ogta and A. Ueda, Geometrical analysis of crystallization of soft-core model. *Prog. Theor, Phys.* **58**, 1079-1095 (1977).

85. Y. Q. Cheng and E. Ma, Atomic-level structure and structure-property relationship in metallic glass. *Prog. Mater. Sci.* **56**, 379-473 (2011).

86. C. P. Royall and S. R. Williams, The role of local structure in dynamical arrest, *Phys. Rep.* **560**, 1-75 (2015).

87. J. Kurchan and D. Levine, Order in glassy systems. *J. Phys. A: Math. Theor.* **44**, 035001 (2011).

88. F. Sausset and D. Levine, Characterizing order in amorphous systems. *Phys. Rev. Lett.* **107**, 045501 (2011).

89. C. Cammarota and G. Biroli, Patch-repetition correlation length in glassy systems. *EPL* **98**, 36005 (2012).

90. J. Ziv and A.Lempel, A universal algorithm for sequential data compression. *IEEE Trans. Inf. Theory* **23**, 337 (1977).

91. S. Martiniani, P. M. Chajkin and D. Levine, Quantifying hidden order out of equilibrium. *Phys. Rev. X* **9**, 011031 (2019).

92. J. F. Sadoc and R. Mosseri, *Geometrical Frustration* (Cambridge UP, London, 2007).

93. L. Pi, F. Casanoves and J. Di Rienzo, *Quantifying functional biodiversity* (Springer, Amsterdam, 2012).

94. J. Maclaurin and K. Sterelny, *What is Biodiversity?* (U. Chicago Press, Chicago, 2008).

95. R. M. May, Patterns in species abundance and diversity, in *Ecology and Evolution of Communities* ed M. L. Cody and J. M. Diamond (Harvard UP, Cambridge 1975), p. 81-120.

96. L. Jost, Entropy and diversity, *Oikos* **113**, 363-375 (2006).

97. H. Tuomisto, A consistent terminology for quantifying species diversity? Yes, it does exist, *Oecologia* **164**, 853-860 (2010).

98. F. W. Preston, The commonness and rarity of species, *Ecology* **29**, 254-283 (1948).

99. R. H. MacArthur, On the relative abundance of bird species, *Proc. Nat. Acad. Sci. USA* **43**, 293-295 (1957).

100. F. He and D. Tang, Estimating the niche pre-emption parameter of the geometric series. *Acta Oecologica* **33**, 105-107 (2008).

101. P. Ronceray and P. Harrowell, The variety of ordering transitions in liquids characterized by a locally favoured structure. *EPL* **96**, 36005 (2011).

102. M. O. Hill, Diversity and evenness: A unifying notation and its consequences. *Ecology* **54**, 427-432 (1973).

103. A. Rényi, On measures of entropy and information. *4th Berkeley symposium on mathematical statistics and probability*. *Ed. J.Neyman,* p. 547-561 (1961).

104. C. E. Shannon and W. Weaver, *The mathematical theory of communication* (University of Illinois Press, 1998).

105. E. H. Simpson, Measurement of diversity, *Nature* **163**, 688 (1949).

106. Frenkel and B. Smit, *Understanding molecular simulation* (Academic Press, London, 2002).

107. A. B. Bortz, M. H. Kalos and J. L. Lebowitz, A new algorithm for the Monte Carlo simulation of Ising spin systems. *J. Comp. Phys.* **17**, 10-18 (1975).

108. F.C. Frank, Supercooling of liquids. *Proc. R. Soc. London Ser A* **215**, 43-46 (1952).

109. J. F. Sadoc and R. Mosseri, *Geometrical Frustration* (Cambridge UP, London, 2007).

110. A. Hirata, J.J. Kang, T. Fujita, B. Klumov, K. Matsue, M. Koyani, A. R. Yavari and M. W. Chen, Geometric frustration of icosahedorn in metallic glasses, *Science* **341**, 376-379 (2013).

111. P. Ronceray and P. Harrowell, Multiple ordering transitions in a liquid stabilized by low symmetry structures. *Phys. Rev. Lett.* **112**, 017801 (2014).

112. P. Ronceray and P. Harrowell, Suppression of crystalline fluctuations by competing structures in a supercooled liquid. *Phys. Rev. E* **96**, 04260 (2017).

113. S. J. Gould and R. Lewontin, The spandrels of San Marco and the Panglossian paradigm: A critique of the adaptionist programme. *Proc. Roy. Soc. B.* **205**, 581-598 (1979).

114. H. J. Fecht, Defect-induced melting and solid-state amorphization. *Nature* **356**, 133-135 (1992).

115. A. T. Motta, Amorphization of intermetallic compounds under irradiation- A review. *J. Nuc. Mater.* **244**, 227-250 (1997).

116. P. Yunker, Z. Zhang and A G. Yodh, Observation of the disorder-induced crystal-to-glass transition. *Phys. Rev. Lett.* **104**, 015701 (2010).

117. S. L. Pimm, The complexity and stability of ecosystems. *Nature* **307**, 321 (1984).

118. D. L. DeAngelis and J. C. Waterhouse, Equilibrium and nonequilibrium concepts in ecological models. *Ecol. Monographs* **57**, 1-21 (1987).

119. S. Allesina and S. Tang, Stability criteria for complex ecosystems. *Nature* **483**, 205-208 (2012).